A study on coherent magnetic properties in Ferrimagnetic Insulator

Doctoral Thesis

博士論文

A study on coherent magnetic properties in Ferrimagnetic Insulator

（強磁性絶縁体におけるコヒーレント磁性物性の研究）

埋田真樹

Department of Physics,
Graduate School of Science,
Tohoku University

東北大学大学院 理学研究科 物理学専攻

2020

令和２年

Dissertation Committee:

Prof. Dr. Gerrit E. W. Bauer, Committee Chair

Prof. Dr. Kozo Fujiwara

Prof. Dr. Yoshiro Hirayama

Assoc. Prof. Dr. Tsutomu Nojima

Prof. Dr. Eiji Saitoh (The University of Tokyo)

Contents

Chapter 1

Introduction

This chapter describes the magnetization dynamics in ferro(ferri) magnetic materials and basic concept of spin current and conventional superconductor. Here, the theoretical background is also provided for the coming discussion in the next chapters. A discussion is focused on the uniform magnetic excitation ($k = 0$), i.e. the ferromagnetic resonance (FMR) and on the non-uniform excitation ($k \neq 0$), i.e. the spin waves, which are of particular interest in this thesis.

1.1 Magnetic order and its interaction

Consider a ferromagnetic sample placed in an external magnetic field H_{ext}, the magnetic moment will experience an effective field H_{eff}, defined as:

$$H_{\text{eff}} = -\frac{1}{\mu_0}\frac{\delta E_{\text{total}}}{\delta M}, \tag{1.1}$$

where the total magnetic energy E_{total} is a function of $\boldsymbol{M}(\boldsymbol{r})$ defined as $\boldsymbol{M}(\boldsymbol{r}) = M_s\boldsymbol{m}(\boldsymbol{r})$ where M_s is the saturation magnetization and $\boldsymbol{m}(\boldsymbol{r})$ is the magnetic moment at the positon $\boldsymbol{r}$, respectively. A sum of the different energies acting in the ferromagnet is

$$E_{\text{total}} = E_{\text{Zeeman}} + E_{\text{demag}} + E_{\text{ani}} + E_{\text{exchange}}. \tag{1.2}$$

E_{zeeman} corresponds to the Zeeman interaction, E_{demag} is the demagnetizing energy, E_{ani} is the anisotropy energy and E_{exchange} is the exchange energy. The expression of the energy for each of these interactions is given below.

- Zeeman energy

  As a magnetic sample is placed in an external magnetic field H_{ext}, the magnetic moments favour a parallel alignment to H_{ext}. The Zeeman energy is expressed as:

  $$E_{\text{Zeeman}} = -\mu_0 \int \boldsymbol{H}_{\text{ext}} \cdot \boldsymbol{M} dV. \tag{1.3}$$

- Demagnetizing energy

  When a magnetic field is applied to the sample the aligned magnetic moments will interact with each other via the dipole-dipole interaction. Magnetic poles are generated on the boundaries of the sample, which creates a demagnetizing field H_d opposite to the direction of the external field. The demagnetizing

field depends on the distribution of the poles over the sample boundaries. It is expressed as

$$H_d = -\boldsymbol{N} \cdot \boldsymbol{M} \tag{1.4}$$

with $\boldsymbol{N}$ is a 3×3 dimensionless tensor, whose trace is equal to unity,

$$N_x + N_y + N_z = 1. \tag{1.5}$$

The energy associated with the demagnetizing field is called the demagnetizing energy, the magnetostatic energy, or the dipolar energy. It is written as:

$$E_{\text{demag}} = -\frac{\mu_0}{2} \int_{\text{sample}} \boldsymbol{M} \cdot \boldsymbol{H}_d dV. \tag{1.6}$$

Of particular importance throughout this thesis is the case of thin films with the z-axis oriented perpendicular to the film plane. The demagnetizing coefficients are $N_{xx} = 0, N_{yy} = 0, and N_{zz} = 1$. The associated demagnetizing energy in such films is written as:

$$E_{\text{demag}} = \frac{\mu_0 V}{2} (\boldsymbol{e}_z \cdot \boldsymbol{M})^2. \tag{1.7}$$

- Anisotropy energy

  The magnetocrystalline anisotropy describes the dependence of the magnetic energy on the relative orientation between the magnetization and the crystal lattice. This dependence arises from the spin-orbit interaction, where the spin moments are coupled to the lattice via the orbital motion of the electrons. In an anisotropic lattice, the lattice is easily magnetized along a preferable crystallographical direction. This is known as a uniaxial anisotropy. The associated volume energy density is:

$$e_K = K_u \sin^2 \theta, \tag{1.8}$$

  where K_u is the anissotropy constant in J/m^3 and θ is the angle between the magnetization vector and the preferred crystallographical direction. Depending on the sign of K_u, the uniaxial direction will be either an easy axis for $K_u > 0$, or a hard axis for $K_u < 0$. At the surface of the film, the reduced symmetry of the atomic orbital produces a surface anisotropy for the magnetization. The surface anisotropy energy density is defined as a function of the angle θ between the surface magnetization and the normal:

$$e_s = -K_s \cos^2 \theta, \tag{1.9}$$

  where K_s is in J/m^2. For $K_s > 0$ the normal of the surface is an easy axis.

- Exchange energy

  The exchange interaction acts on the electron spins in order to align the spins such that the Coulomb interaction energy is minimized. The exchange energy between two neighbouring magnetic moments $\boldsymbol{S}_i$ and $\boldsymbol{S}_j$ is usually described by:

$$e_{\text{exchange}} = -J\boldsymbol{S}_i \cdot \boldsymbol{S}_j. \tag{1.10}$$

J is the exchange integral which originates from the wave function overlap of two electrons. The exchange energy for a system of particles, under the assumption that the exchange energy is short-ranging and subsequently only acts on direct neighbours, is:

$$E_{\text{exchange}} = \frac{1}{2}\sum_{i,j} e_{\text{exchange}}. \tag{1.11}$$

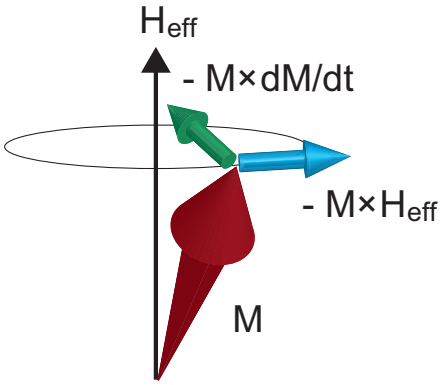

Figure 1.1 Gyromagnetic response of dc-biased ferrite to RF magnetic field with damping.

The magnetic moment equation of motion was first proposed by Landau and Lifshitz, based on a magnetic torque model. This torque equation was first applied to microwave magnetics by Kittel in his theory for ferromagnetic resonance. The equation of motion of a magnetization vector $\boldsymbol{M}$ can be written

$$\frac{d\boldsymbol{M}}{dt} = -|\gamma|\boldsymbol{M} \times \boldsymbol{H}_{\text{eff}}. \tag{1.12}$$

Upon displacing $\boldsymbol{M}$ from its equilibrium direction, it moves back to equilibrium in a spiralling trajectory due to the relaxation. This behaviour is given by Landau-Lifshitz-Gilbert equation (LLG);

$$\frac{d\boldsymbol{M}}{dt} = -|\gamma|\boldsymbol{M} \times \boldsymbol{H}_{\text{eff}} + \frac{\alpha}{|\boldsymbol{M}|}\left[\boldsymbol{M} \times \frac{d\boldsymbol{M}}{dt}\right]. \tag{1.13}$$

The last term in Eq. (1.13) phenomenologically describes this damping of the magnetization precession. α is a dimensionless constant called the damping factor. In detail, the relaxation rate κ_s and hence the resonance linewidth $\Delta\omega$ for a Gilbert-type damping term as in Eq. (1.13) depends on the precession frequency ω_{res} as follows:

$$\frac{1}{2\kappa_s} = \Delta\omega = 2\alpha\omega_{\text{res}} + \Delta\omega_0. \tag{1.14}$$

Here, the inhomogeneous broadening $\Delta\omega_0$ phenomenologically accounts for contributions to the relaxation that do not depend on the precession frequency such as relaxation via magnetic inhomogeneities or surface scattering.

The total effective field $\boldsymbol{H}_{\text{eff}}$ in the magnetic torque equation for an isotropic ferromagnetic medium consists of five fields: an applied static external field $\boldsymbol{H}_{\text{ext}}$, the

static demagnetization field $\boldsymbol{H}_{\rm dem}$, an applied microwave pump field $\boldsymbol{h}_p(t)$, the dipole field $\boldsymbol{h}_{\rm dip}(\boldsymbol{r},t)$, and the effective exchange field $\boldsymbol{h}_{\rm ex}(\boldsymbol{r},t)$.

$$\boldsymbol{H}_{\rm eff}(\boldsymbol{r},t) = \boldsymbol{H}_{\rm ext} + \boldsymbol{H}_{\rm dem} + \boldsymbol{h}_p(t) + \boldsymbol{h}_{\rm dip}(\boldsymbol{r},t) + \boldsymbol{h}_{\rm ex}(\boldsymbol{r},t). \tag{1.15}$$

For simplicity, the contribution of anisotropy is not included.

$\boldsymbol{H}_{\rm ext}$ is taken to be sufficient to magnetize the sample to saturation along the z-direction. The demagnetizing field is the static dipole field generated by the static magnetization $\boldsymbol{M}_s$ for a finite-size sample and generally related to the shape of the sample. For $\boldsymbol{M}_s$ along $\boldsymbol{e}_z$, this field is given by

$$\boldsymbol{H}_{\rm dem} = -M_s \boldsymbol{N} \cdot \boldsymbol{e}_z. \tag{1.16}$$

When the three principal axes of the ellipsoidal sample coincide with the x-, y-, and z-axes, only the diagonal elements on the tensor are nonzero and denoted as N_x, N_y, and N_z. For $\boldsymbol{H}_{\rm ext}$ and M_s in the z-direction, the demagnetizing is simply

$$\boldsymbol{H}_{\rm dem} = -M_s N_z \boldsymbol{e}_z. \tag{1.17}$$

We combine $H_{\rm ext}$ and $H_{\rm dem}$ to form the static internal field $H_{\rm int}$ as

$$\boldsymbol{H}_{\rm int} = (H_{\rm ext} - M_s N_z)\boldsymbol{e}_z. \tag{1.18}$$

Static equilibrium always requires that M_s be aligned along $\boldsymbol{H}_{\rm int}$.

The third field in $\boldsymbol{H}_{\rm eff}$ is the applied microwave pump field $\boldsymbol{h}_p(t)$. The microwave pump field is used as an excitation field for the spin system in the sample. In the case of applying it parallel to the static internal field or perpendicular to the static internal field, we can call it parallel pumping or perpendicular pumping, respectively.

The fourth field is the dipole field $\boldsymbol{h}_{\rm dip}(\boldsymbol{r},t)$. The dipole field is the dynamic magnetic field in the sample due to the dipole-dipole interaction of the precessing magnetic moments in the spin system. This includes the effects of both the uniform precession and the spin-wave components of the dynamic magnetization $\boldsymbol{m}(\boldsymbol{r},t)$. The dipole field is taken to satisfy Maxwell equations in the form

$$\nabla \times \boldsymbol{h}_{\rm dip}(\boldsymbol{r},t) = 0 \tag{1.19}$$

and

$$\nabla \cdot [\boldsymbol{h}_{\rm dip}(\boldsymbol{r},t) + \boldsymbol{m}(\boldsymbol{r},t)] = 0. \tag{1.20}$$

Equation (1.20) is obtained from Maxwell equations under the magnetic approxiamation described in Appendix A. Electromagnetic propagation effects are thus neglected by this approximation.

1.2 Uniform magnetization precession

Here, ferromagnets are only discussed. For static $\boldsymbol{M}_s$ along $\boldsymbol{e}_z$, $\boldsymbol{M}(\boldsymbol{r},t)$ is

$$\boldsymbol{M}(\boldsymbol{r},t) = M_s \boldsymbol{e}_z + \boldsymbol{m}(\boldsymbol{r},t) \tag{1.21}$$

and spatial Fourier expansion for $\boldsymbol{m}(\boldsymbol{r},t)$ can be written as

$$\boldsymbol{m}(\boldsymbol{r},t) = \boldsymbol{m}_0(t) + \sum_{k\neq 0} \boldsymbol{m}_k(t) e^{-i\boldsymbol{k}\cdot\boldsymbol{r}}, \tag{1.22}$$

$$\boldsymbol{m}_k^*(t) = \boldsymbol{m}_{-k}(t) \tag{1.23}$$

where $*$ is the complex conjugate of a complex component. Having written down the detailed expressions for the magnetization vector $\boldsymbol{M}(\boldsymbol{r},t)$ and total effective field $\boldsymbol{H}_{\text{eff}}(\boldsymbol{r},t)$ in (1.15), we now proceed to examine the equation of motion for the dynamic magnetization $\boldsymbol{m}(\boldsymbol{r},t)$. The total effective field $\boldsymbol{H}_{\text{eff}}(\boldsymbol{r},t)$ is given by

$$\begin{aligned}\boldsymbol{H}_{\text{eff}} &= H_{\text{int}}\boldsymbol{e}_z + \boldsymbol{h}_p(t) - \boldsymbol{N}\cdot\boldsymbol{m}_0(t) \\ &\quad - \sum_{k\neq 0} \boldsymbol{N}_k \cdot \boldsymbol{m}_k(t) e^{-i\boldsymbol{k}\cdot\boldsymbol{r}} - \frac{D}{M_s}\sum_{k\neq 0} k^2 \boldsymbol{m}_k(t) e^{-i\boldsymbol{k}\cdot\boldsymbol{r}}\end{aligned} \tag{1.24}$$

where D is the exchange stifness constant. Terms in this expression for the total effective field can be classified temporarily or spatially. From the time variation point of view, $\boldsymbol{H}_{\text{eff}}(\boldsymbol{r},t)$ contains static and dynamic terms; while from the spatial variation point of view, $\boldsymbol{H}_{\text{eff}}$ has uniform and nonuniform terms.

LL equation (1.12) yields

$$\begin{aligned}&\dot{\boldsymbol{m}}_0(t) + \sum_{\boldsymbol{k}\neq 0} \dot{\boldsymbol{m}}_k(t) e^{-i\boldsymbol{k}\cdot\boldsymbol{r}} \\ &= -|\gamma|[\boldsymbol{M}_s\boldsymbol{e}_z + \boldsymbol{m}_0(t) + \sum_{\boldsymbol{k}\neq 0} \boldsymbol{m}_k(t) e^{-i\boldsymbol{k}\cdot\boldsymbol{r}}] \times [\boldsymbol{H}_{\text{int}}\boldsymbol{e}_z + \boldsymbol{h}_p(t) - \boldsymbol{N}\cdot m_0(t) \\ &- i\sum_{\boldsymbol{k}'=0} N_{k'}\cdot\boldsymbol{m}_{k'}(t) e^{-i\boldsymbol{k}'\cdot\boldsymbol{r}} - \frac{D}{M_s}\sum_{k'\neq 0} k'^2 \boldsymbol{m}_{k'}(t) e^{-i\boldsymbol{k}'\cdot\boldsymbol{r}}].\end{aligned} \tag{1.25}$$

The dots above the $\boldsymbol{m}_0(t)$ and $\boldsymbol{m}_k(t)$ terms denote time derivatives. Equation (1.25) provides the foundation for investigating various linear and nonlinear spin-wave processes. In particular, the analysis yields the uniform mode FMR response, spin-wave dispersion, and spin-wave instability thresholds. We separate the general equation into two equations, one for $\boldsymbol{m}_0(t)$ and one for $\boldsymbol{m}_k(t)$. The equation of motion for the uniform mode $\boldsymbol{m}_0(t)$ is given by

$$\dot{\boldsymbol{m}}_0(t) = -|\gamma|[H_{\text{int}}\boldsymbol{m}_0(t) + M_s\boldsymbol{N}\cdot\boldsymbol{m}_0(t) - M_s\boldsymbol{h}_p(t)] \times \boldsymbol{e}_z. \tag{1.26}$$

The general equation of motion for spin waves ($k \neq 0$) to first order can be separated from Eq. (1.25) as

$$\begin{aligned}\dot{\boldsymbol{m}}_k(t) = &-|\gamma| \\ &[H_{\text{int}}\boldsymbol{m}_k(t) + M_s\boldsymbol{N}_k^L\cdot\boldsymbol{m}_k(t) + Dk^2\boldsymbol{m}_k(t)] \times \boldsymbol{e}_z \\ &+ M_s\boldsymbol{N}_k^N\cdot\boldsymbol{m}_k(t)\times\boldsymbol{e}_z + \boldsymbol{N}_k^L\cdot\boldsymbol{m}_k(t)\times\boldsymbol{m}_0(t) - \boldsymbol{h}_p(t)\times\boldsymbol{m}_k(t).\end{aligned} \tag{1.27}$$

This nonlinear equation yields the so-called first-order spin instability effect. We will not discuss other nonlinear effects (like the second-order spin instability) resulting from the inclusion of higher-order nonlinear coupling terms.

The linear response of the uniform mode can be examined by linearizing (1.26), as given by

$$\dot{\boldsymbol{m}}_0(t) = -|\gamma|\mu_0[H_{\text{int}}\boldsymbol{m}_0(t) + M_s\boldsymbol{N}\cdot\boldsymbol{m}_0(t) - M_s\boldsymbol{h}_p(t)]\times\boldsymbol{e}_z. \tag{1.28}$$

First, consider the pump-free response for $\boldsymbol{m}_0(t)$. It shows that the dynamic magnetization $\boldsymbol{m}_0(t)$ precesses elliptically around the direction of the static external field in the Larmor sense at the frequency ω_0 given by

$$\omega_0 = |\gamma|\mu_0\sqrt{[H_{\text{ext}} + M_s(N_x - N_z)][H_{\text{ext}} + M_s(N_y - N_z)]}. \tag{1.29}$$

This is the well known Kittel resonance frequency. The ratio of the amplitude components m_{0x} and m_{0y} is found to be

$$\frac{m_{0x}}{m_{0y}} = \sqrt{\frac{H_{\text{ext}} + M_z(N_y - N_z)}{H_{\text{ext}} + M_z(N_x - N_z)}}. \tag{1.30}$$

For the special case of a sphere with $N_x = N_y = N_z = 1/3$, the x- and y- components of the amplitude become equal,

$$m_{0x} = m_{0y}. \tag{1.31}$$

The precession is, therefore, circular and the frequency is simply

$$\omega_0 = |\gamma|\mu_0 H_{\text{ext}}. \tag{1.32}$$

Now consider the pumped response of $\boldsymbol{m}_0(t)$. We consider spherical samples only the assume that the uniform mode is driven by a microwave field $\boldsymbol{h}_p(t)$ at frequency ω_p.

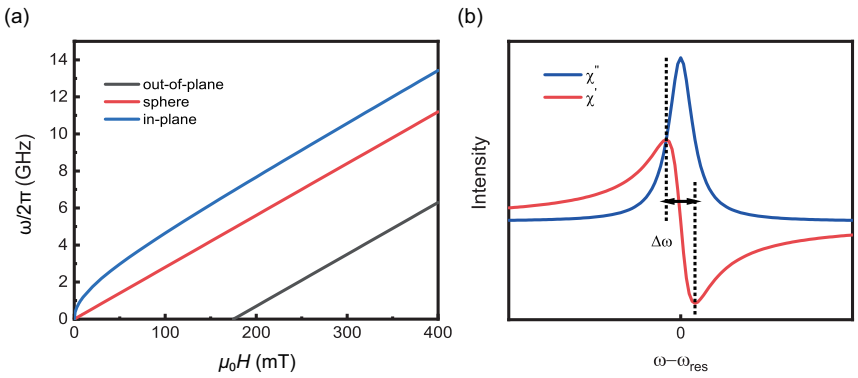

Figure 1.2 (a) ω_{res} as a function of $\mu_0 H$ taking into account the shape anisotropy for a sphere, an out-of-plane magnetized thin film and an in-plane magnetized thin film, respectively. (b) The Polder susceptibility χ at fixed external magnetic field strength $\mu_0 H$ as a function of w close to the ferromagnetic resonance frequency ω_{res}. Also indicated is the FWHM linewidth $\Delta\omega$.

To obtain dynamical solutions for Eq. (1.13) (Here we use LLG equation, which includes the damping term), we only consider an external static magnetic field $\boldsymbol{H}_{\text{ext}}$ applied parallel to the z-direction $\boldsymbol{H}_{\text{ext}} = (0, 0, H_{\text{ext}})$. The axis of precession and the equilibrium direction of $\boldsymbol{M}$ is therefore also aligned along z. We take a dynamic

externally applied magnetic field into account and separate the dynamic parts of $\boldsymbol{H}$ and $\boldsymbol{M}$ in a static and a dynamic part

$$\boldsymbol{H} = \boldsymbol{H}_{\text{ext}} + \boldsymbol{h}_p(t), \tag{1.33}$$
$$\boldsymbol{M} = \boldsymbol{M}_0 + \boldsymbol{m}(t), \tag{1.34}$$

where M_0 is the absolute value of the static magnetization and $\boldsymbol{m}$ is the vector of the dynamic transversal components of $\boldsymbol{M}$. Due to the precession frequencies of many ferrites in the microwave range, $\boldsymbol{h}_p$ is called the microwave magnetic field. For a small microwave magnetic field $\boldsymbol{h}_p = (h_x(t), h_y(t), 0)$ perpendicular to $\boldsymbol{H}_{\text{ext}}$, the precessing magnetization can be approximated as $\boldsymbol{M} = (m_x(t), m_y(t), M_0)$. The solution of the linearized LLG equation for a harmonic time dependence is then given by $\boldsymbol{m} = \tilde{\chi}\boldsymbol{h}_p$ and the high-frequency magnetic susceptibility tensor (Polder tensor)

$$\tilde{\chi} = \begin{pmatrix} \chi_{11} & i\chi_{12} \\ -i\chi_{12} & \chi_{22} \end{pmatrix}. \tag{1.35}$$

The diagonal elements ($\chi = \chi_{11} = \chi_{22}$ neglecting anisotropies) of the Polder tensor, typically called the Polder susceptibility, determine the response of the magnetic system to a linear excitation field $\boldsymbol{h}_p$ and are thus of particular interest. Neglecting terms $\mathcal{O}(\alpha^2)$, χ is given by

$$\chi_{\omega,H_0} = \frac{\omega_M(\gamma\mu_0 H_{\text{ext}} - i\Delta\omega)}{\omega_0^2(H_{\text{ext}}) - \omega^2 - i\omega\Delta\omega} \tag{1.36}$$
$$\equiv \tilde{\chi}'(\omega) - i\tilde{\chi}''(\omega) \tag{1.37}$$

with the resonance frequency ω_0 and $\omega_M = \gamma\mu_0 M_0$. In Fig. 1.2, χ is shown as a function of ω around ω_{res}.

Summarizing, the above derivation describes the linear response of a ferromagnet to an external static magnetic field H_{ext} in combination with a dynamic magnetic field $\boldsymbol{h}_p, \boldsymbol{H} = (h_x, h_y, H_{\text{ext}})$ in the absence of magnetic anisotropies.

1.3 Spin waves

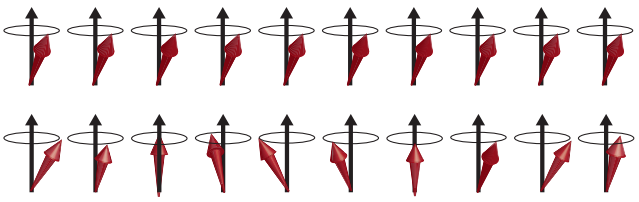

Figure 1.3 Schematic illustration of a ferromagnetic spin wave on a linear chain. (up) Kittel mode for $k = 0$ and (down) $k \neq 0$.

In the last section, the discussion is only about uniform precession mode where all the magnetic moments are collinear and precess in phase throughout the entire sample. However, the magnetic moments are coupled to each other through dipole-dipole and/or exchange interactions. The result of these interactions can be seen if

one excites some magnetic moments locally, the precession motion of those moments can propagate spatially in the magnetic material like a wave (Fig. 1.3). This wave is, therefore, a collective excitation of magnetic moments and is usually termed as a spin-wave.

1.3.1 Spin wave dispersion relation in an unbounded medium

We now turn to discuss the linear response of spin waves. We examine the equation of motion for the spin-wave amplitude $\boldsymbol{m}_k(t)$. The component form of the linearized equation of motion for $\boldsymbol{m}_k(t)$ can be obtained by taking the first right-hand-side term of (1.25) only,

$$\dot{\boldsymbol{m}}_k(t) = -|\gamma|[H_{\rm int}\boldsymbol{m}_k(t) + M_s N_k^L \cdot \boldsymbol{m}_k(t) + Dk^2\boldsymbol{m}_k(t)] \times \boldsymbol{e}_k \tag{1.38}$$

so

$$\begin{aligned}\dot{m}_{kx}(t) =& -\frac{1}{2}\omega_M \sin^2\theta_k \sin 2\phi_k m_{kx}(t) \\ & -(\omega_H + |\gamma|Dk^2 + \omega_M \sin^2\theta_k \sin^2\phi_k) m_{ky}(t), \qquad (1.39)\\ \dot{m}_{ky}(t) =& -\frac{1}{2}\omega_M \sin^2\theta_k \cos^2\phi_k m_{kx}(t) \\ & +\frac{1}{2}\omega_M \sin^2\theta_k \sin 2\phi_k) m_{ky}(t), \qquad (1.40)\end{aligned}$$

where θ_k and ϕ_k are the polar angles between static magnetization and the spinwave wavevector $\boldsymbol{k}$. Here, we have introduced two important frequency parameters, ω_H and ω_M.

$$\omega_H = |\gamma|\mu_0(H_{\rm ext} + H_{\rm dem}) = |\gamma|\mu_0 H_{\rm int}. \tag{1.41}$$

$$\omega_M = |\gamma|\mu_0 M_s. \tag{1.42}$$

These parameters express the internal field $H_{\rm int}$ and the saturation magnetization $4\pi M_s$ in frequency units.

As in the $\boldsymbol{m}_0(t)$ analysis, it is convenient to define two reduced complex amplitudes for spin waves.

$$\alpha_k(t) = \frac{1}{M_s}[m_{kx}(t) + i m_{ky}(t)]. \tag{1.43}$$

$$\alpha^*_{-k}(t) = \frac{1}{M_s}[m_{kx}(t) - i m_{ky}(t)]. \tag{1.44}$$

The spin-wave equation of motion for $m_{kx}(t)$ and $m_{ky}(t)$ given in Eq. (1.39),(1.40) can be transformed into a coupled matrix equation for $\alpha_k(t)$ and $\alpha^*_{-k}(t)$ as:

$$\frac{d}{dt}\begin{pmatrix} \alpha_k(t) \\ \alpha^*_{-k}(t) \end{pmatrix} = i\begin{pmatrix} A_k & B_k \\ -B_k^* & -A_k \end{pmatrix}\begin{pmatrix} \alpha_k(t) \\ \alpha^*_{-k}(t) \end{pmatrix}. \tag{1.45}$$

The coefficients A_k and B_k in the above equation are given by

$$A_k = \omega_H + |\gamma|Dk^2 + \frac{1}{2}\omega_M \sin^2\theta_k \tag{1.46}$$

and

$$B_k = \frac{1}{2}\omega_M \sin^2\theta_k e^{i2\phi_k}. \tag{1.47}$$

Note that A_k and B_k expressions are unchanged if the wavevector $\boldsymbol{k}$ is replaced by $-\boldsymbol{k}$. Hence, the relations $A_{-k} = A_k$ and $B_{-k} = B_k$ are satisfied.

Equation (1.40) shows that $\alpha_k(t)$ and $\alpha^*_{-k}(t)$ behave as a pair of coupled harmonic oscillators. The details of the specific transformation produce for spin-wave is given in Appendix B. The coupled spin-wave equation of motion for the $\alpha_k(t)$ and $\alpha^*_{-k}(t)$ of Eq. (1.45), decoupled under the Holstein-Primakoff transformation, yields

$$\begin{pmatrix} b_k(t) \\ b^*_{-k}(t) \end{pmatrix} = i \begin{pmatrix} \omega_k & 0 \\ 0 & -\omega_k \end{pmatrix} \begin{pmatrix} b_k(t) \\ b^*_{-k}(t) \end{pmatrix}. \tag{1.48}$$

The ω_k parameter in Eq. (1.48) is

$$\omega_k^2 = A_k^2 - |B_k^2|. \tag{1.49}$$

Equation (1.48) has simple uncoupled harmonic oscillator solutions of the form

$$b_k(t) = b_k e^{i\omega_k t}, \tag{1.50}$$

$$b^*_{-k}(t) = b^*_{-k} e^{-i\omega_k t}. \tag{1.51}$$

$$\tag{1.52}$$

These $b_k(t)$ and $b^*_{-k}(t)$ correspond to the spin-wave normal modes at frequency ω_k. The explicit expression of frequency ω_k for the spin-wave normal modes is given by

$$\omega_k = |\gamma| \sqrt{(H_{\text{int}} + Dk^2)(H_{\text{int}} + Dk^2 + 4\pi M_s \sin^2 \theta_k)}. \tag{1.53}$$

This is the well-known dispersion relation for spin waves.

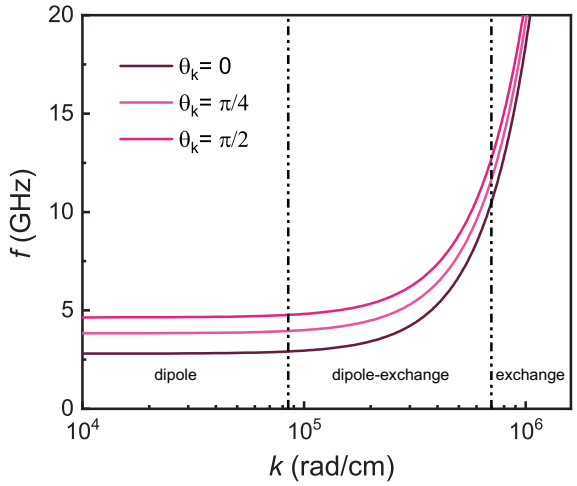

Figure 1.4 Dispersion relations for spin waves in an unbounded medium. The parameters $\mu_0 H_{\text{int}} = 100$ mT, $\mu_0 M_s = 175$ mT and $D = 3.2 \times 10^{-12}$ cm^{-12} for YIG are used.

The spin-wave frequency ω_k depends on the wavevector $\boldsymbol{k}$ in several ways. First, ω_k increases more-or-less quadratically with wavenumber k. This increase comes from exchange energy. Second, ω_k increases with θ_k. This is a result of the dipole fields and energy associated with the nonzero $\nabla \cdot \boldsymbol{m}$ for $\theta_k \neq 0$ spin waves. Figure 1.4 shows a schematic of the dispersion for three different θ_k values: $0, \pi/4$, and $\pi/2$.

Depending on the wavenumber value, the dispersion relation is separated into three different regions: (1) dipolar spin-wave region, (2) the dipole-exchange wave region, and (3) the exchange wave region. Dipolar spin-wave region roughly correspond to the region where the wavenumbers are below 10^5 rad/cm. In this region, the frequency has a weak dependence on the wavenumber.

1.3.2 Spin wave dispersion relation in a bounded medium

In this section, we present the dispersions of spin waves in thin ferromagnetic films. We consider only sample configurations for which the wave vector propagates in the plane of the film. Three types of magnetic field/film configurations are considered as follows.

Consider first the geometry where a magnetic field is applied out of the film plane. In this case, the boundary conditions require $\boldsymbol{h}_{x,y}$ to be continuous across the upper and lower film surfaces. Also, it is important to notice that the film thickness d is much smaller than the spin-wave decay length. Thus, spin waves will have reflections back and forth along the propagating axis and the component of the wave vector k will be quantized. A detailed derivation can be carried out with the above boundary conditions, Maxwell' s equations, and the magnetic torque equation. This derivation, however, will not be discussed herein details. For the lowest-order mode, a useful approximate dispersion relation has been derived by Kalinikos [1],

$$\omega(k) = \sqrt{\omega_H[\omega_H + \omega_M \left(1 - \frac{1 - e^{-kd}}{kd}\right)]} \tag{1.54}$$

where k is the spin-wave wavenumber in the film plane and d is the thickness of the film. Spin waves in the configuration is the so-called magneto-static forward volume waves. Several additional points should be made for forward volume waves. First of all, the notation forward comes from the fact that the group velocity is in the same direction as the phase velocity. This can be seen directly from the positive slope of the dispersion curve as seen in Fig. 1.5(a). Volume in the notation denotes that the spin-wave excitations are extended throughout the entire film thickness, as opposed to a surface mode. Second, the slope of dispersion curve or group velocity is decreasing with an increase in wavenumber. One can define the dispersion coefficient as follows,

$$D = \frac{\partial^2 \omega(k)}{\partial k^2}. \tag{1.55}$$

This dispersion coefficient has a negative value for forward volume spin waves. Forward volume waves have a rotation symmetry in the film plane since the magnetic field is applied out of the plane.

Two special field/wave vector configurations are as follows: (1) the wave vector is parallel to the magnetic field direction and (2) the wave vector direction is perpendicular to the field.

The first configuration supports the propagation of backward volume waves. The dispersion relation can be derived using a similar method described above for forward

volume waves. An approximate dispersion relation for the lowest-order mode has also been derived by Kalinikos [1],

$$\omega(k) = \sqrt{\omega_H \left[\omega_H + \omega_M \left(\frac{1 - e^{-kd}}{kd}\right)\right]}. \tag{1.56}$$

Fig. 1.5(b) shows an example of this dispersion curve. As opposed to forward volume waves, the phase velocity of the backward volume wave has an opposite sign for the group velocity, which explains the backward nature of such waves. Also, the dispersion coefficient of the backward volume wave is positive.

The second configuration supports the propagation of surface waves. This configuration is different from forward and backward volume waves because the wave amplitude exponentially decays in out-of-plane direction (in the thickness direction). In the case where k is larger than $1/d$, spin waves propagate on one of the surfaces of the film. The dispersion relation equation for surface waves has also been derived by Kalinikos [1],

$$\omega(k) = \sqrt{\omega_H(\omega_H + \omega_M) + \frac{\omega_M^2}{4}\left(1 - e^{-2kd}\right)}. \tag{1.57}$$

It is evident from Fig. 1.5(c) that for surface waves the group velocity and the phase velocity are in the same direction. The dispersion coefficient of surface waves is negative.

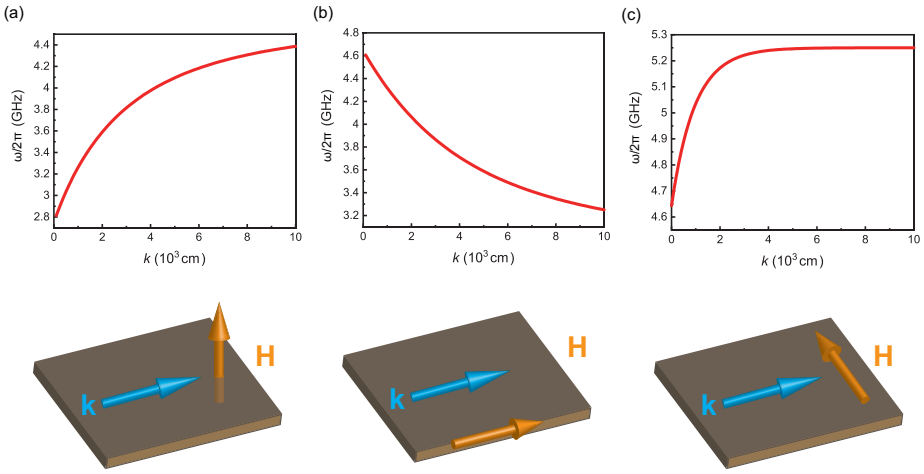

Figure 1.5 Examples of dispersion curves for (a) magneto-static forward volume waves, (b) magneto-static backward volume waves, and (c) magneto-static surface waves ($\mu_0 H = 100$ mT, $\mu_0 M_s = 175$ mT).

1.3.3 Exchange-dipole regime

In the previous section, the wavelength of the spin waves is considered to be larger than the exchange length, the length scale across which the exchange interaction is dominant over the demagnetizing energy, so that the spin waves are in the pure magnetostatic regime approximation. However, in the region where the wave propagates

with a wavelength comparable to the exchange length one should account for the exchange interaction. The exchange-dipole regime is briefly dicussed in this section based on the Kalinikos-Slavin theory [2].

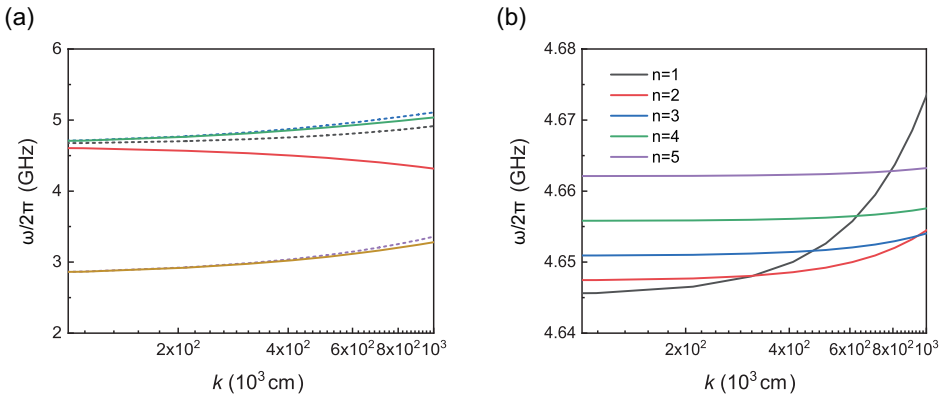

Figure 1.6 (a) Plot of the dispersion relation in the magnetostatic regime (solid lines) and the exchange-dipolar regime (dotted line) for the three configurations: MSFVW, MSBVW, and MSSW. The parameters are t =5 μm, $\mu_0 M_s$=175 mT, applied field $\mu_0 H_0$=100 mT, and $\gamma/2\pi$ =28 GHz/T, respectively. (b) Dispersion relation of PSSW from $n = 1$ to $n = 5$.

Due to the presence of the exchange operator in the effective field, the equation of motion will be an integral-differential equation of the second order. To solve this equation one needs supplymentary boundary conditions in addition to the electromagentic boundary conditions. Rado and Weertman [3] studied the modification in the ferromagnetic resonance under the influence of the exchange interaction as introduced surface spin pinning conditions. Their model assumes that spins at the surface experience a different local field than bulk spins, which is determined by the surface free energy. The supplymentary exchange boundary condition is written as [4]:

$$T_{\text{surf}} = -\frac{2A}{M_s^2} M \times \frac{\partial M}{\partial n} \tag{1.58}$$

where n is the normal of the surface, and T_{surf} is the total surface torque density which arises from forces other than the exchange interaction. Using these boundary conditions, Kalinikos and Slavin solved the integro-differential equation for the spin wave modes with as arbitrary angle between the propagation direction and the field. The dispersion relation of the spin-wave in the case of the exchange-dipolar regime reads [1] :

$$\omega_n^2 = (\omega_H + \alpha\omega_M k_n^2)(\omega_H + \alpha\omega_M k_n^2 + \omega_M F_{nn}) \tag{1.59}$$

with $k_n^2 = k_{||}^2 + q_n^2$, where q_n is the wavevector in the film, and $\alpha = \frac{2A}{\mu_0 M_0^2}$, with

$$F_{nn} = P_{nn} + \sin^2\theta(1 - P_{nn}(1 + \cos^2\phi) + \omega_M \frac{P_{nn}(1 - P_{nn}\sin^2\phi)}{\omega_H + \alpha k_n^2}), \tag{1.60}$$

where the θ is the angle between the magnetization and the normal of the film, and ϕ is the angle between $\boldsymbol{M}$ and $\boldsymbol{k}$. P_{nn} are the matrix elements relating the dynamical

magnetization and the dipolar field. In the case of unpinned surface spin ($q_n = \frac{n\pi}{d}$), the expression for P_{nn} has the form

$$P_{nn} = \frac{k^2}{k_n^2}\left(1 + \frac{k^2}{k_n^2}\frac{2}{1+\delta_{0n}}\frac{1-(-1)^n \mathrm{e}^{-\mathrm{kd}}}{kd}\right) \tag{1.61}$$

where δ_{0n} is the Kronecker delta.

In the longwave limit ($kd \ll 1$) a simple expression for P_{nn} may be found using these equations. In the case of unpinned surface, the expression for the P_{nn} has the form

$$P_{nn} = kL/2 \text{ when } n = 0 \tag{1.62}$$

$$P_{nn} = (kL)^2/n^2\pi^2 \text{ when } n \neq 0 \tag{1.63}$$

In particular, numerical calculations show that in the longwave part of the spectrum the equation (1.59) gives the results which coincide accurately with the results obtained from the non-exchange dispersion equations (1.54, 1.56, 1.57).

1.3.4 Quasiparticle description of spin waves: magnon

Consider a system of localized electrons, such as $3d$ electrons. Spin waves are the waves which are generated by parallelly aligned atomic spins in a ferromagnetic material. Spin waves of very long wavelengths (dipole interaction is dominant) can be excited by an oscillating magnetic field, but usually they are excited by thermal motion at various wavelengths. In the case of spin waves of short wave length, the exchange interaction between the spins become dominant and provide the restoring force if an external magnetic field is applied. Also, the magnetic anisotropic energy also adds to the restoring force.

The simplest case is the case where there is a uniform magnetic field $\boldsymbol{H}$ and all the spin moments at a rest point in the direction of the field. The anisotropic energy is assumed to be negligible. However, if the anisotropic energy can be introduced in the form of a uniform effective magnetic field, it is the same as in the case of an external magnetic field.

The equation of motion for the m-th spin $\boldsymbol{S}_m$ is Heisenberg's equation of motion is

$$-i\hbar\dot{\boldsymbol{S}}_m = [\mathcal{H}, \boldsymbol{S}_m] \tag{1.64}$$

and Hamiltonian $\mathcal{H}$ is

$$\mathcal{H} = -\sum_{\langle m,n\rangle} J_{mn}\boldsymbol{S}_m \cdot \boldsymbol{S}_n + g\mu_B \sum_m \boldsymbol{S}_m \cdot \boldsymbol{H}. \tag{1.65}$$

Using the commutation relation

$$[S_i, S_j] = i\epsilon_{ijk}S_k \tag{1.66}$$

where ϵ_{ijk} is the Levi-Civita symbol of variables i, j, and k, (1.65) is changed as

$$\hbar\dot{\boldsymbol{S}}_m = \boldsymbol{S}_m \times (2\sum_n J_{mn}\boldsymbol{S}_n - g\mu_B\boldsymbol{H}). \tag{1.67}$$

The left side represents the rate of change of the angular momentum $\hbar \boldsymbol{S}_m$ and the right side represents the moment of force acting on the magnetic moment $-g\mu_B \boldsymbol{S}_m$. Let spin components S_{mz} and S_{nz} in the $-\boldsymbol{H}$ direction be equal to S, assuming the amplitude of the wave is small. Also, if we leave the x and y components to the first-order terms (1.67),

$$\hbar \dot{S}_{mx} = (2S \sum_n J_{mn} + g\mu_B H) S_{my} - 2S \sum_n J_{mn} S_{ny}, \tag{1.68}$$

$$\hbar \dot{S}_{my} = (2S \sum_n J_{mn} + g\mu_B H) S_{mx} - 2S \sum_n J_{mn} S_{nx}, \tag{1.69}$$

$$\hbar \dot{S}_{mz} = 0. \tag{1.70}$$

To do a Fourier transform of the spin, multiply both sides of the above formula by $N^{-1}\exp(-i\boldsymbol{k} \cdot \boldsymbol{R}_m)$ and add about m. Writing $\boldsymbol{R}_m = (\boldsymbol{R}_m - \boldsymbol{R}_n) + \boldsymbol{R}_n = \boldsymbol{R}_{mn} + \boldsymbol{R}_n$ and $\sum_{mn} J_{mn} = J(\boldsymbol{k})$, we can get

$$\begin{aligned} \hbar \dot{S}_{kx} &= [2SJ(0) + g\mu_B H] S_{ky} \\ &\quad - 2SN^{-1} \sum_{mn} J_{mn} \exp(-i\boldsymbol{k} \cdot \boldsymbol{R}_{mn}) \exp(-i\boldsymbol{k} \cdot R_n) S_{ny}, \\ &= [2SJ(0) + g\mu_B H] S_{ky} - 2SJ(\boldsymbol{k}) S_{ky}. \end{aligned} \tag{1.71}$$

Similarly,

$$\hbar \dot{S}_{ky} = -[2SJ(0) + g\mu_B H] S_{kx} + 2SJ(\boldsymbol{k}) S_{kx}. \tag{1.72}$$

We assumed a Brave lattice in the above Fourier transform.

To solve for this, let S_{kx} and S_{ky} be proportional to $\exp(-i\omega_{\boldsymbol{k}} t)$, the equation is

$$-i\hbar\omega_{\boldsymbol{k}} S_{\boldsymbol{k}x} = \{2S[J(0) - J(\boldsymbol{k})] + g\mu_B H\} S_{\boldsymbol{k}y}, \tag{1.73}$$

$$-i\hbar\omega_{\boldsymbol{k}} S_{\boldsymbol{k}y} = -\{2S[J(0) - J(\boldsymbol{k})] + g\mu_B H\} S_{\boldsymbol{k}x}, \tag{1.74}$$

and

$$\hbar\omega_{\boldsymbol{k}} = 2S[J(0) - J(\boldsymbol{k})] + g\mu_B H, \tag{1.75}$$

$$S_{\boldsymbol{k}x} : S_{\boldsymbol{k}y} = 1 : -i. \tag{1.76}$$

From the above results, a spin wave with a wave number $\boldsymbol{k}$ has a frequency $\omega_{\boldsymbol{k}}$. S_{mx} and S_{my} are represented by the following for a single S_m,

$$S_{mx} = S_{\boldsymbol{k}x} \exp(i\boldsymbol{k} \cdot \boldsymbol{R}_m - i\omega_{\boldsymbol{k}} t), \tag{1.77}$$

$$S_{my} = -iS_{\boldsymbol{k}x} \exp(i\boldsymbol{k} \cdot \boldsymbol{R}_m - i\omega_{\boldsymbol{k}} t), \tag{1.78}$$

or real representation is

$$S_{mx} = A\cos(\boldsymbol{k} \cdot \boldsymbol{R}_m - \omega_{\boldsymbol{k}} t + \alpha), \tag{1.79}$$

$$S_{my} = A\sin(\boldsymbol{k} \cdot \boldsymbol{R}_m - \omega_{\boldsymbol{k}} t + \alpha). \tag{1.80}$$

Each moment the x, y components of the spin system show a helical arrangement with small amplitude. Since the z component is constant S, the whole is a cone array with a small tilt angle.

A slightly more quantum-mechanical-looking treatment begins by writing, for example, the spin vector $\boldsymbol{S}$ as follows,

$$S_x + iS_y = S^+ = (2S)^{1/2}(1 - \frac{b^\dagger b}{2S})^{1/2} b, \tag{1.81}$$

$$S_x - iS_y = S^- = (2S)^{1/2} b^\dagger (1 - \frac{b^\dagger b}{2S})^{1/2}, \tag{1.82}$$

$$S_z = S - b^\dagger b. \tag{1.83}$$

We take $b^\dagger$ is the creation operator of the Bose particle. The Holstein-Primakov formula, which satisfies the commutation relations for $b(b^\dagger)$ are

$$[b_{\boldsymbol{k}\sigma}, b^\dagger_{\boldsymbol{k}'\sigma'}] = \delta_{\boldsymbol{k}\boldsymbol{k}'}\delta_{\sigma\sigma'}, \tag{1.84}$$

$$[b_{\boldsymbol{k}\sigma}, b_{\boldsymbol{k}'\sigma'}] = 0, \tag{1.85}$$

$$[b^\dagger_{\boldsymbol{k}\sigma}, b^\dagger_{\boldsymbol{k}'\sigma'}] = 0. \tag{1.86}$$

We take b and $b^\dagger$ up to the second-order term of $b^\dagger$ and perform Fourier-transformation to obtain the eigenvalue of $n_{\boldsymbol{k}}\hbar\omega_{\boldsymbol{k}}(n_{\boldsymbol{k}} = 0, 1, 2, \cdots)$, where $n_{\boldsymbol{k}}$ is the value of n_b. We can see that the energy is quantized as magnon. However, assuming $b^\dagger b = n \ll 2S$, we can expand $(1 - b^\dagger b/2S)^{1/2}$, but if $S = 1/2$, this assumption will be no longer satisfied, so the value of S must be large.

1.4 Nonlinear effect: Spin wave instability process

1.4.1 Spin wave equation of motion

Following discussion is based on [5]. Spin-wave instability theory derives from the inclusion of additional terms which are still first order in the $\boldsymbol{m}_k(t)$ components but also contain $\boldsymbol{m}_0(t)$ components and/or a nonzero z-components of $\boldsymbol{h}_p(t), h_{pz}(t)$. A z-components microwave pump field $h_{pz}(t)$ leads to a special case of instability termed parallel pumping. The first order nonlinear $\boldsymbol{m}_k(t)$ equation for spin waves is already given. We now rewrite this equation in component form as

$$\begin{aligned}
\dot{m}_{kx}(t) =& -(\omega_H + |\gamma|Dk^2 + \omega_M \sin^2\theta_k \sin^2\phi_k) m_{ky}(t), \\
=& -\frac{1}{2}\omega_M \sin^2\theta_k \sin 2\phi_k m_{kx}(t) + \frac{1}{2}(\omega_M/M_s)\sin 2\theta_k \\
&\times [\sin\phi_k m_{0x}(t) m_{kx}(t) + \cos\phi_k m_{0y}(t) m_{kx}(t) \\
&+ 2\sin\phi_k m_{0y}(t) m_{ky}(t)] - |\gamma| h_{pz}(t) m_{ky}(t).
\end{aligned} \tag{1.87}$$

$$\begin{aligned}
\dot{m}_{ky}(t) =& -(\omega_H + |\gamma|Dk^2 + \omega_M \sin^2\theta_k \cos^2\phi_k) m_{kx}(t), \\
=& -\frac{1}{2}\omega_M \sin^2\theta_k \sin 2\phi_k m_{ky}(t) - \frac{1}{2}(\omega_M/M_s)\sin 2\theta_k \\
&\times [2\cos\phi_k m_{0x}(t) m_{kx}(t) + \sin\phi_k m_{0x}(t) m_{ky}(t) \\
&+ \cos\phi_k m_{0y}(t) m_{ky}(t)] + |\gamma| h_{pz}(t) m_{kx}(t).
\end{aligned} \tag{1.88}$$

These two equations are the basis for first-order spin wave instability theory. Equations constitute a coupling between the uniform mode $\boldsymbol{m}_0(t)$ or a parallel pump field $h_{pz}(t)$ and a spin wave mode $\boldsymbol{m}_k(t)$. The equations are first recognized by invoking the reduced complex spin-wave amplitude $\alpha_k(t)$ and $\alpha^*_{-k}(t)$ defined in Eq. (1.43,

1.44). The resulting spin wave equation of motion for the $\alpha_k(t)$ and α^*_{-k} is then obtained as

$$\frac{d}{dt}\begin{pmatrix} \alpha_k(t) \\ \alpha^*_{-k}(t) \end{pmatrix} = i\begin{pmatrix} A_k & B_k \\ -B^*_k & -A_k \end{pmatrix}\begin{pmatrix} \alpha_k(t) \\ \alpha^*_{-k}(t) \end{pmatrix} + i\begin{pmatrix} C_k & D_k \\ -D^*_k & -C^*_k \end{pmatrix}\begin{pmatrix} \alpha_k(t) \\ \alpha^*_k(t) \end{pmatrix}. \tag{1.89}$$

The A_k and B_k coefficients are the same as in the linear theory. The $C_k(t)$ and $D_k(t)$ coefficients are given by

$$C_k(t) = \frac{1}{2}\omega_M \sin\theta_k \cos\theta_k [e^{-i\phi_k}\alpha_0(t) + e^{i\phi_k}\alpha^*_0(t)] + |\gamma| h_{pz}(t) \tag{1.90}$$

$$D_k(t) = -\omega_M \sin\theta_k \cos\theta_k e^{i\phi_k}\alpha_0(t) \tag{1.91}$$

$C_k(t)$ and $D_k(t)$ terms involve the uniform mode amplitude $\alpha_0(t)$ and the z-component of the microwave pumping field $h_{pz}(t)$. Under low power conditions, the $\alpha_0(t)$ and $h_{pz}(t)$ terms are small. In this limit, these terms may be neglected and Eq. (1.89) reduces to the linear part which can be diagonalized by a Holstein-Primakoff transformation. To solve Eq. (1.89), we proceed by applying the same transformation to the nonlinear equation of with the $\alpha_0(t)$ and $h_{pz}(t)$ terms included.

$$\frac{d}{dt}\begin{pmatrix} b_k(t) \\ b^*_{-k}(t) \end{pmatrix} = i\begin{pmatrix} \omega_k + F_k(t) & G_k(t) \\ -G^*_k(t) & -[\omega_k + F_k(t)]^* \end{pmatrix}\begin{pmatrix} b_k(t) \\ b^*_{-k}(t) \end{pmatrix}. \tag{1.92}$$

the $F_k(t)$ and $G_k(t)$ coefficients are given by

$$F_k(t) = \lambda_k^2 C_k(t) + |\mu_k|^2 C^*_k(t) - \lambda_k \mu^*_k D_k(t) - \lambda_k \mu_k D^*_k(t) \tag{1.93}$$

and

$$G_k(t) = -\lambda_k \mu_k [C_k(t) + C^*_k(t)] + \lambda_k^2 D_k(t) + \mu_k^2 D^*_k(t) \tag{1.94}$$

here, the parameters λ_k and μ_k are the Holstein-Primakoff transformation parameters developed in Appendix B.

The $F_k(t)$ term leads to a change in the spin-wave frequency ω_k. This change is typically small compared with the value of ω_k when the microwave frequency ω_p is far away from the FMR frequency ω_0. Therefore, the $F_k(t)$ term may be ignored.

The $G_k(t)$ term in Eq. (1.92) has a more substantial effect. As we shall see, this term leads to the parametric coupling and unstable grown of the spin-wave amplitudes $b_k(t)$ and $b^*_{-k}(t)$ at high pumping power levels. As will be shown shortly, the $G_k(t)$ term turns out to be the coupling coefficient for the energy pumped into the spin-wave modes through the microwave field and the uniform mode.

1.4.2 First-order Suhl instability

To study first-order instability effects of the sort introduced above, it is necessary to introduce dissipation in the magnetic system. This is done phenomenologically by replacing the uniform mode frequency ω_0 and spin-wave frequency ω_k in Eqs. (1.89) and (1.92) with complex frequencies.

$$\omega_0 \rightarrow \Omega_0 = \omega_0 + i\eta_0 \tag{1.95}$$

$$\omega_k \rightarrow \Omega_k = \omega_k + i\eta_k \tag{1.96}$$

Here, η_0 denotes the uniform precession relaxation rate, and η_k denotes spin-wave relaxation rate for the particular spin-wave vector $\boldsymbol{k}$ under consideration. The uniform precession relaxation rate is conveniently expressed in terms of the corresponding FMR linewidth. For the uniform precession, the resonance absorption half-power full field-swept linewidth ΔH is expressed in terms of η_0

$$\Delta H = \frac{2\eta_0}{|\gamma|}. \tag{1.97}$$

For spin waves, we write a parallel expression,

$$\Delta H_k = \frac{2\eta_k}{|\gamma|}, \tag{1.98}$$

where ΔH_k is simply defined as the spin-wave full line width.

The spin wave equation of motion with the $F_k(t)$ term neglected and damping parameters included is given by

$$\frac{d}{dt}\begin{pmatrix} b_k(t) \\ b^*_{-k}(t) \end{pmatrix} = i\begin{pmatrix} \Omega_k & G_k(t) \\ -G^*_k(t) & -\Omega^*_k \end{pmatrix}\begin{pmatrix} b_k(t) \\ b^*_{-k}(t) \end{pmatrix}. \tag{1.99}$$

Our objective now is to solve this equation for $b_k(t)$ and $b^*_{-k}(t)$, and obtain corresponding threshold conditions for instability. The $G_k(t)$ term is first expanded into a series,

$$G_k = \sum_n G^{(n)}_k e^{in\omega_p t}. \tag{1.100}$$

First-order instability can be evaluated by considering only the $n = 1$ term of Eq. (1.100), that is, that part of $G_k(t)$ which varies as $\exp(\mathrm{i}\omega_\mathrm{p}\mathrm{t})$. The spin-wave equation of motion pertinent to first-order instability is given by

$$\frac{d}{dt}\begin{pmatrix} b_k(t) \\ b^*_{-k}(t) \end{pmatrix} = i\begin{pmatrix} \Omega_k & G^{(1)}_k e^{i\omega_p t} \\ -G^{(1)*}_k e^{-i\omega_p t} & -\Omega^*_k \end{pmatrix}\begin{pmatrix} b_k(t) \\ b^*_{-k}(t) \end{pmatrix}. \tag{1.101}$$

the $G^{(1)}_k$ expression for linearly polarized microwave field is given by

$$\begin{aligned} G^{(1)}_k = &-\frac{\omega_m}{4\omega_k}\sin^2\theta_k e^{i2\phi_k}|\gamma|h_{pz} - \frac{\omega_M}{2\omega_k}\sin\theta_k\cos\theta_k e^{i2\phi_k} \\ &\times[(\omega_H + |\gamma|Dk^2 + \omega_k)e^{-i\phi_k}\alpha^+_0 + (\omega_H + |\gamma|Dk^2 - \omega_k)e^{i\phi_k}\alpha^{-*}_0]. \end{aligned} \tag{1.102}$$

note that $G^{(1)}_k, h_{pz}, \alpha^+_0$ are time-independent. The parallel pumping field is given by $h_{pz} = h_{pz}\cos(\omega_p t)$. The α^+_0 and α^-_0 are the uniform mode Larmor and anti-Larmor responses. From Eq. (1.100), we obtain an ordinary differential equation for $b_k(t)$,

$$\left\{\frac{d^2}{dt^2} + (2\eta_k - i\omega_k)\frac{d}{dt} + [\omega^2_k + \eta^2_k - \omega_p(\omega_k + i\eta_k) - |G^{(1)}_k|^2]\right\} b_k(t) = 0. \tag{1.103}$$

The general solution to Eq. (1.100) is given by

$$b_k(t) = b_k e^{i\frac{1}{2}\omega_p t + \kappa t}. \tag{1.104}$$

The time exponential κ-parameter in this solution is obtained as

$$\kappa = -\eta_k \pm \sqrt{|G^{(1)}_k|^2 - (\omega_k - \omega_p/2)^2}. \tag{1.105}$$

Equation (1.105) reveals the basic nature of first-order instability process. One has, essentially, a competition between the coupling of microwave energy into the b_k mode via η_k. For a spin wave as low power levels, where $G_k^{(1)}$ is negligible, Eq. (1.105) reduces to the linear solution discussed above with an additional damping term

$$b_k(t) = b_k e^{i\omega_k t - \eta_k t}. \tag{1.106}$$

The spin wave amplitude remains at thermal levels due to the relaxation losses. At higher power levels where $|G_k^{(1)}| > |\omega_k - \omega_p/2|$ is satisfied, the spin wave amplitude increases exponentially with time as described by Eq. (1.105) and we have instability.

We see, therefore, that the κ-parameter determines the instability condition. When $\kappa < 0$ is satisfied, losses dominate and spin wave amplitude is stable and remains as thermal levels. This is a low power case. When the power is high enough so that $\kappa > 0$ is satisfied, the coupling dominates, the spin wave is unstable, and $b_k(t)$ tends to grow exponentially in time. The condition $\kappa = 0$ marks the onset of spin-wave instability. The instability threshold condition is obtained from the $\kappa = 0$ condition, which yields,

$$|G_k^{(1)}| = \sqrt{(\omega_k - \omega_p/2)^2 + \eta_k}. \tag{1.107}$$

We can now see the significance of $\omega_p/2$ and the specific nature of the threshold. The smallest value of the coupling term $|G_k^{(1)}|$ for Eq. (1.107) occurs at $\omega_k = \omega_p/2$. This frequency condition describes the coupling of the microwave pump field or the uniform precession mode at ω_p to spin waves at $\omega_k = \omega_p/2$ and $\pm\boldsymbol{k}$. The threshold condition now reduces to a very simple equation,

$$|G_k^{(1)}| = \eta_k. \tag{1.108}$$

Recall that $|G_k^{(1)}|$, given in eq. (1.105), contains field amplitude parameters of microwave pump in h_{pz} for parallel pumping and in h_p through $\alpha_0^{\pm}$ for perpendicular pumping. The main point for now is that $|G_k^{(1)}|$ increases linearly with the microwave pumping filed amplitude h_{pz} and h_p. At the critical point in h_{pz} or h_p is the microwave field threshold amplitude h_c for the instability. In the parallel pumping case, we have $h_p = 0$. In this limit, one may solve the Eq. (1.107) for h_{pz} and obtain a microwave field threshold amplitude h_c for the parallel pumping instability of specific waves. One may follow the same procedure for the perpendicular pumping case ($h_{pz} = 0$) and obtain the subsidiary absorption threshold h_c as follows.

Perpendicular Pumping

Nonlinear effects in magnetic materials were first observed in the conventional configuration of ferromagnetic resonance experiments with the RF magnetic field applied perpendicular to the dc bias field. For perpendicular excitation, the RF field primarily excites the uniform mode of the sample. The uniform mode, in turn, induces a time-varying coupling between spin waves propagating in opposite directions and hence gives rise to parametric excitation of these waves. These spin waves that resonate at ω_p are most susceptible to instability due to the first-order process.

The conditions for the appearance of spin wave instability are found to be expressed in equation (1.107). Now, considering the situation ($h_{pz} = 0, \alpha_0^+, \alpha_0^{-*} \neq 0$) where the RF magnetic field is applied perpendicular to the magnetization, $|G_k^{(1)}|$ in Eq. (1.102) can be expressed as,

$$G_k^{(1)} = -\frac{\omega_M}{2\omega_k} \sin\theta_k \cos\theta_k e^{i2\phi_k} \\ [(\omega_H + |\gamma|Dk^2 + \omega_k)e^{-i\phi_k}\alpha_0^+ + (\omega_H + |\gamma|Dk^2 - \omega_k)e^{i\phi_k}\alpha_0^-]. \tag{1.109}$$

Here, using the relation of $\alpha_0^{\pm}$ as

$$\alpha_0^+ = \frac{1}{2}\frac{\gamma h_p}{\omega_0 - \omega_p} \tag{1.110}$$

$$\alpha_0^- = \frac{1}{2}\frac{\gamma h_p}{\omega_0 + \omega_p}, \tag{1.111}$$

$|G_k^{(1)}|$ can be rewrite as

$$G_k^{(1)} = -\frac{1}{2}\gamma h_p \left(\frac{\omega_M}{2\omega_k}\right) e^{i2\phi_k} W(\omega_k, \theta_k, \phi_k) \tag{1.112}$$

$$W(\omega_k, \theta_k, \phi_k) = \omega_k \sin\theta_k \cos\theta_k \left[\frac{e_k(\theta_k)+1}{\omega_0 - \omega_p} e^{-i\phi_k} + \frac{e_k(\theta_k)-1}{\omega_0 + \omega_p} e^{i\phi_k}\right]. \tag{1.113}$$

Substituting Eq. (1.113) into Eq. (1.102), we obtain the threshold RF field strength at which the instability appears as

$$h_c = \frac{\omega_p}{\omega_M}\frac{\Delta H_k}{|W(\theta_k, \phi_k)|} \\ = \min_{\theta_k}\left\{\frac{\omega_p}{\omega_M}\frac{1-(\frac{\omega_0}{\omega_p})^2}{1+\frac{\omega_0}{\omega_p}e_k(\theta_k)}\frac{\Delta H_k}{\sin\theta_k\cos\theta_k}\right\}. \tag{1.114}$$

Here, $\min_{\mathrm{k},\theta_\mathrm{k}}\{\mathrm{g(k,\theta_k)}\}$ is the operator that produces the minimum value of the function $g(k, \theta_k)$ for k and θ_k.

For a given RF field strength the amplitude of the uniform mode is largest when the sample is biased to resonance. The lowest threshold for instability, therefore, occurs at resonance, provided that the first-order process is allowed under these conditions. The lowest spin-wave frequency, on the other hand, is given by ω_H. First-order instability can occur at resonance if

$$2\omega_H \leq \omega_0 \tag{1.115}$$

By eliminating ω_H this condition can alternatively be expressed as

$$\omega_0 \leq \omega_c \text{ and } \omega_\mathrm{c} \equiv 2\mathrm{N_z}\omega_\mathrm{M} \tag{1.116}$$

For spherical samples ($N_z = 1/3$) of YIG at room temperature, the first-order process is allowed at resonance immediately above the threshold can be analyzed when the pump frequency is below 3.3 GHz.

1.4.3 Multi-magnon scattering process

A single mode (for instance the uniform mode in FMR) or a small group of modes (for instance a group of spin waves in perpendicular pumping) are excited by an

Scattering process	Schematic illstration	Conserved quantities
2-magnon scattering	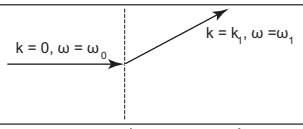	$k_0 \neq k_1, \omega_0 = \omega_1$
3-magnon scattering	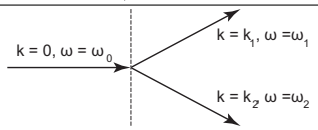	$k_0 = k_1 + k_2, \omega_0 = \omega_1 + \omega_2$
4-magnon scattering	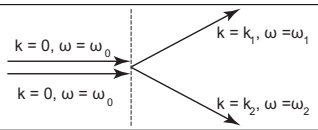	$2k_0 = k_1 + k_2, \omega_0 = \omega_1 + \omega_2$

electromagnetic signal. The excited modes can distribute their energy within the magnetic system or by interaction with other degrees of freedom (charge carriers, lattice vibrations, strongly relaxing ions, etc.). In low-loss microwave ferrites, the interactions within the magnetic system appear to be the most important. We will therefore focus attention on these relaxation processes.

The general procedure for calculating relaxation rates begins with the determination of the normal modes of the system. Next, the energy is expressed in terms of the normal mode amplitudes. The linear term of this Hamiltonian vanishes, because the normal amplitudes are defined as deviations from the energy minimum. In quantum mechanics, the normal mode amplitudes can be interpreted as creation and annihilation operators that obey the commutation relation. The Hamiltonian can be written as

$$\mathcal{H} = \mathcal{H}_0 + \mathcal{H}^{(2)} + \mathcal{H}_w, \tag{1.117}$$

$$\mathcal{H}_w = \mathcal{H}^{(3)} + \mathcal{H}^{(4)} \tag{1.118}$$

where $\mathcal{H}_0$ is the energy constant and $\mathcal{H}^{(2)}$ is the energy eigenvalue of the system. $\mathcal{H}_w$ is the addional component which induce the relaxation process.

In terms of these operators, the second-order Hamiltonian $\mathcal{H}^{(2)}$ becomes

$$\mathcal{H}^{(2)} = \hbar \sum_k \omega_k b_k^* b_k \tag{1.119}$$

where $b_k^* b_k = n_k$ is the occupation number of mode k. The eigenstates of the Hamiltonian $\mathcal{H}^{(2)}$ are characterized by a set of integer occupation numbers n_k. Because of dipolar and exchange interactions, $\mathcal{H}_w$ contains terms like

$$\mathcal{H}^{(3)} = \hbar \sum_{kk'k''k'''} P_{kk'k''} b_k b_{k'} b^*_{-k''} + c.c., \tag{1.120}$$

$$\mathcal{H}^{(4)} = \hbar \sum_{kk'k''k'''} P_{kk'k''k'''} b_k b_{k'} b^*_{-k''} b^*_{-k'''} + c.c., \tag{1.121}$$

which induce transitions P between these eigenstates. The third- and fourth-order terms of Hamiltonian induce relaxation processes, which are usually labelled as 3-magnon and 4-magnon processes. These processes occur in all ferro- and ferrimagnetic

materilas, in particular in perfect single crystals of ultrapure low-loss materals, such as YIG. The third-order Hamiltonian induces transitions, in which one magnon is

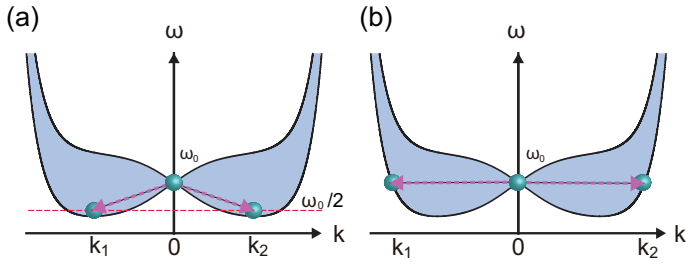

Figure 1.7 A schematic diagram of the (a) 3-magnon scattering process and (b) 4-magnon process in the dispersion relation.

absorbed and two are emitted (splitting process) or two magnons are absorbed and one is emitted (confluence process). In these transitions, Zeeman energy is converted into dipolar and exchange energy, and vice versa. In Fig. 1.7(a), the 3-magnon splitting and confluence processes are illustrated by simple diagrams. In the splitting process, the directly excited magnon (k) splits into two magnons k' and k'', under conservation of energy and momentum. The analysis shows that the conservation laws can be satisfied in two different ways, giving rise to two kinds of splitting processes: the low-k process (allowed only for frequencies less than $(2/3)\omega_M$, see the previous section), and the high-k splitting process (allowed only for sufficiently high k, not important in my experiment). Both of these processes give a contribution to the relaxation rate of spin waves that remains finite as the wave number approaches zero. The 3-magnon confluence process, on the other hand, gives a contribution to the relaxation rate that is proportional to k (for small k), at least for ferromagnetic materials. In the 4-magnon scattering process, illustrated in Fig. 1.7(b), a directly excited magnon k combines with a thermal magnon k' and forms magnons k'' and k''', under conservation of energy and momentum.

Additional, relaxation processes are significant in materials that contain imperfections, such as crystal defects, nonmagnetic inclusions (including pores), and grain boundaries. It can be described by an additional second-order term in the Hamiltonian, an interaction between spin waves of different wave number. The relaxation processes induced by this interaction are usually referred to as 2-magnon processes.

1.5 Spin current

The relation between charge density ρ and the conduction current $\boldsymbol{j}_c$ can be written as

$$\frac{d\rho}{dt} = -\nabla \cdot \boldsymbol{j}_c, \tag{1.122}$$

which represents the charge conservation law.

With this charge conservation law, we define spin current as a flow of spin angular momentum that satisfies the continuous equation for magnetization, as well as the

current. If we do not consider spin relaxation and magnetic fields, then the law of conservation of spin angular momentum allows us to determine the time variation of the magnetic moment $\int_\Omega \frac{d\boldsymbol{M}}{dt} = -\nabla \cdot \boldsymbol{j}_s d\Omega$ in a volume Ω from the S The flow is equal to the flow of the magnetic moment $-\int_S -\gamma \boldsymbol{j}_s \cdot d\boldsymbol{n}$. If we rewrite the inflowing spin current as a volume integral of divergence using Gaussian theorem, we obtain the spin current

$$\frac{d\boldsymbol{M}}{dt} = -\gamma \nabla \cdot \boldsymbol{j}_s \tag{1.123}$$

as a continuous equation of magnetization, which is a differential system of the spin angular momentum conservation law. Because the current is a vector quantity, whereas the spin current is a second-order tensor quantity, it is necessary to consider two directions of the spin current: the direction of the spin current flow (spatial component) and the spin-polarized component.

In the spin current, conduction electron and spin-wave (magnon) are the typical carriers of spin angular momentum. These two types of spin currents will be described in the following sections.

When an external field, such as an electric field, is applied to a metal or semiconductor, a non-equilibrium current is driven by conduction electrons on the Fermi surface. Similarly, in a conductor with conduction electrons, the conduction electrons driven by an external force also carries spin angular momentum. While the conduction current is the net charge flow carried by the conduction electron, the conduction spin current is the net spin angular momentum. Thus, the current $\boldsymbol{j}_c$ and the conduction spin current $\boldsymbol{j}_s$ are represented as

$$\boldsymbol{j}_c = \frac{1}{(2\pi)^3} e \sum_{\boldsymbol{k}\sigma\sigma'} v^i_{\boldsymbol{k}\sigma} c^\dagger_{\boldsymbol{k}\sigma} c_{\boldsymbol{k}\sigma}, \tag{1.124}$$

$$\boldsymbol{j}_s = \frac{1}{(2\pi)^3} \frac{\hbar}{2} \sum_{\boldsymbol{k}\sigma\sigma'} v^i_{\boldsymbol{k}\sigma} c^\dagger_{\boldsymbol{k}\sigma} \sigma^{\sigma\sigma'} c_{\boldsymbol{k}\sigma}, \tag{1.125}$$

where e is the charge, and σ is the Pauli matrix, and $c^\dagger_k(c_k)$ is the creation (annihilation) operator of electrons specified by the wavenumber $\boldsymbol{k}$ with spin σ. If we fix the spin quantization axis and choose a good quantum number, the spin current can be treated as a vector as well as a current. If $\boldsymbol{j}_\uparrow$ is the density of up-spin electrons, then ((1.124) and (1.124)、(1.125) can be represented as

$$\boldsymbol{j}_c = e(\boldsymbol{j}_\uparrow + \boldsymbol{j}_\downarrow), \tag{1.126}$$

$$\boldsymbol{j}_s = \frac{\hbar}{2}(\boldsymbol{j}_\uparrow - \boldsymbol{j}_\downarrow), \tag{1.127}$$

respectively.

1.5.1 Spin wave spin current

Consider the effective magnetic field in the presence of ferromagnetic exchange interactions. Substituting the energy from the Heisenberg exchange interaction $\mathcal{H} = -2J\sum_{\langle i,j\rangle} \boldsymbol{S}_i \cdot \boldsymbol{S}_j$ into the equation of motion to obtain the effective magnetic field

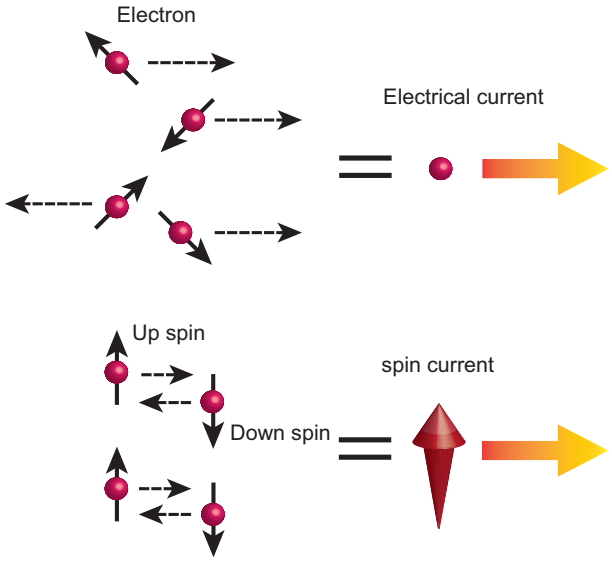

Figure 1.8 Electrical current and conduction-electron spin current

at the i site, the result is

$$\boldsymbol{H}_{\text{eff}}^{i} = -2\frac{J}{\gamma}\sum_{\langle i,j\rangle}\boldsymbol{S}_j \tag{1.128}$$

where J is called the exchange constant. We return this to the LL equation and add the relaxation term $\boldsymbol{T}'$ to obtain

$$\frac{d}{dt}\boldsymbol{m}_i = 2J\boldsymbol{m}_i \times \sum_{\langle i,j\rangle}\boldsymbol{S}_j + \boldsymbol{T}'. \tag{1.129}$$

To approximate from atomic position i to an a continuum atomic position $\boldsymbol{r}$, let $\boldsymbol{S}_i = \boldsymbol{S}(\boldsymbol{r})$ and let the distance between $\boldsymbol{S}_i$ and its nearest neighbour, $\boldsymbol{S}_j$ be given as $\boldsymbol{a}$. Let be denoted as $\boldsymbol{S}_j = \boldsymbol{S}(r+\boldsymbol{a})$. Taylor expansion of $\boldsymbol{S}(r+\boldsymbol{a})$ is as

$$\boldsymbol{S}(\boldsymbol{r}+\boldsymbol{a}) = \boldsymbol{S}(\boldsymbol{r}) + \frac{\partial \boldsymbol{S}(\boldsymbol{r})}{\partial \boldsymbol{r}}\cdot\boldsymbol{a} + \frac{1}{2}\frac{\partial^2 \boldsymbol{S}(\boldsymbol{r})}{\partial^2 \boldsymbol{r}}\cdot\boldsymbol{a}^2 + \cdots \tag{1.130}$$

with $\boldsymbol{S}(\boldsymbol{r}+\boldsymbol{a})$ and substitute it into (1.129). Considering that if there is an atom at the position of $\boldsymbol{r}$, there will always be an atom in $-\boldsymbol{r}$, the lowest order of the Taylor expansion is a term with second derivatives for a position. Therefore, the equation of motion is

$$\frac{d}{dt}\boldsymbol{m}(\boldsymbol{r}) = \frac{2Ja^2}{\gamma}\boldsymbol{m}(\boldsymbol{r}) \times \nabla^2\boldsymbol{m}(\boldsymbol{r}) + \boldsymbol{T}'. \tag{1.131}$$

Using the following relation as

$$\boldsymbol{m} \times \nabla^2\boldsymbol{m} = \nabla\cdot(\boldsymbol{m}\times\nabla\cdot\boldsymbol{m}) \tag{1.132}$$

and the formula (1.131), we get

$$\frac{d}{dt}\boldsymbol{m}(\boldsymbol{r}) = -A\gamma\nabla\cdot(\boldsymbol{m}\times\nabla\cdot\boldsymbol{m}), \tag{1.133}$$

which is the same form as the continuous equation. The new spin current $\boldsymbol{j}_s$, defined by

$$\boldsymbol{j}_s = \boldsymbol{m}\times\nabla\cdot\boldsymbol{m}, \tag{1.134}$$

is a continuous equation representing the flow of spin angular momentum. The spin current is called the exchange spin current, which is a representation of the exchange interaction using the spin current. Add the relaxation term and we get

$$\frac{d}{dt}\boldsymbol{m} = -\gamma\nabla\cdot\boldsymbol{j}_s + \frac{\alpha}{m}\boldsymbol{m}\times\frac{d}{dt}\boldsymbol{m}. \tag{1.135}$$

The exchange current is proportional to $\nabla\boldsymbol{m}$. If, when the magnetic moment is not aligned, the exchange current flows under $\nabla\cdot\boldsymbol{m}\neq 0$ and tries to change (rotate) the magnetic moment according to (1.133). This action and relaxation work together to set the magnetization in motion, and this motion continues until the magnetization is aligned ($\nabla\cdot\boldsymbol{m}=0$, zero exchange spin current). This exchange spin current is a spin current that flows in equilibrium, sometimes called equilibrium spin current or superspin current.

Consider the spin currents carried by spin waves, which are dynamic magnetization modulation structures. Exciting the dynamics of magnetization allows us to excite exchange spin currents in a steady state. Low energy magnetization dynamics in a magnetic material can be described by elementary excitations called spin waves, which are wave motions of magnetization, as already mentioned. Spin waves are states in which the microprecession of magnetization around the equilibrium magnetization propagates as waves, and their quantization is called a magnon. There are two types of spin waves: exchange spin waves and magnetstatic spin waves, and here we formulate the spin current carried by spin waves, considering exchange interaction as the main magnetic interaction.

The low-energy part of the exchange spin-wave, which is ferromagnetic, is described by the LLG equation as

$$\frac{\partial}{\partial t}\boldsymbol{M}(\boldsymbol{r},t) = -\gamma\boldsymbol{M}(\boldsymbol{r},t)\times\boldsymbol{H}_{\text{eff}} - \frac{D}{M_s}\boldsymbol{M}(\boldsymbol{r},t)\times\nabla^2\boldsymbol{M}(\boldsymbol{r},t) + \frac{\alpha}{M_s}\boldsymbol{M}(\boldsymbol{r},t)\times\frac{\partial}{\partial t}\boldsymbol{M}(\boldsymbol{r},t) \tag{1.136}$$

where $\boldsymbol{H}_{\text{eff}}$ is the effective magnetic field in z-direction and D is the exchange stiffness coefficient. This differential equation is solved by

$$M_+(\boldsymbol{r},t) = M_x(\boldsymbol{r},t) + iM_y(\boldsymbol{r},t) \propto \exp(i\boldsymbol{k}\cdot\boldsymbol{r} - \frac{i\omega_k t}{\hbar})\exp(-\alpha\omega_k) \tag{1.137}$$

and has a spin-wave dispersion relation of $\omega_k = \gamma H_{\text{eff}} + Dk^2$. We ignore the relaxation terms for simplicity. In this case (1.65) is rewritten as

$$\frac{\partial}{\partial t}\boldsymbol{M}(\boldsymbol{r},t) = -\gamma\boldsymbol{M}(\boldsymbol{r},t)\times\boldsymbol{H}_{\text{eff}} - \nabla\cdot\boldsymbol{J}^M(\boldsymbol{r},t). \tag{1.138}$$

In this equation, $\boldsymbol{J}^M(\boldsymbol{r},t)$ is an exchange spin current

$$\boldsymbol{J}_\beta^{M_\lambda}(\boldsymbol{r},t) = \frac{D}{M_s}[\boldsymbol{M}\times\nabla_\beta\boldsymbol{M}]_\lambda = \frac{D}{M_s}\epsilon_{\lambda\mu\nu}\boldsymbol{M}_\mu\nabla_\beta\boldsymbol{M}_\nu \tag{1.139}$$

where M_λ is the λth component of the magnetic vector M, and J_β is the βth component of the direction of the magnetic moment flow, and $\epsilon_{\lambda\mu\nu}$ is the Levi-Civita symbol.

If the relaxation can be neglected, i.e., when $\alpha = 0$ is negligible, the z component of (1.138) can be expressed as

$$\frac{\partial}{\partial t} M(z,t) + \nabla \cdot \boldsymbol{J}^{M_z}(z,t) = 0, \tag{1.140}$$

which has the same form as the continuous equation for spin currents. Using the new description as

$$\phi(\boldsymbol{r},t) = M_+(\boldsymbol{r},t) = M_x(\boldsymbol{r},t) + iM_y(\boldsymbol{r},t), \tag{1.141}$$
$$\phi^*(\boldsymbol{r},t) = M_-(\boldsymbol{r},t) = M_x(\boldsymbol{r},t) - iM_y(\boldsymbol{r},t), \tag{1.142}$$

the z component of the spin-wave spin current can be rewritten as follows.

$$\boldsymbol{J}^{M_z} = \frac{1}{2i}\frac{D}{M_s}[\phi^*(\boldsymbol{r},t)\nabla\phi(\boldsymbol{r},t) - \phi(\boldsymbol{r},t)\nabla\phi^*(\boldsymbol{r},t)] \tag{1.143}$$

1.6 Spin current generation and detection

1.6.1 Spin Hall and Inverse spin Hall effect

1.6.2 Spin Hall effect

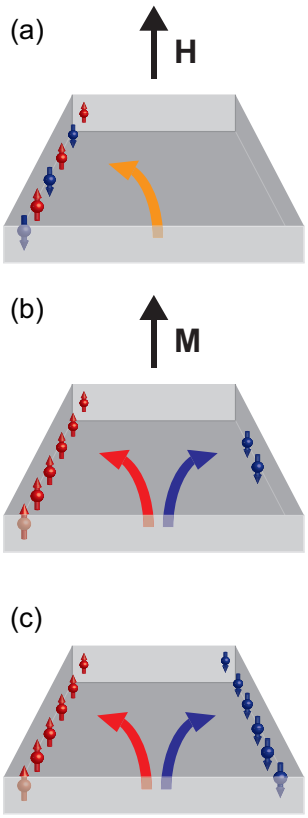

Figure 1.9 Schematic representation of the different Hall effects: (a) Ordinary Hall Effect, (b) Anomalous Hall Effect, and (c) Spin Hall Effect.

When an electric current is passed through a material placed in a magnetic field, a voltage proportional to the magnetic field strength is generated in the direction orthogonal to both the current direction and the magnetic field direction. This is called the normal Hall effect (Fig. 1.9(a)). This phenomenon is caused by the Lorentz force. In contrast, in ferromagnetism, a new Hall voltage appears in the direction orthogonal to both its magnetization and current. This phenomenon, called the anomalous Hall effect, is due to spin-orbit interactions in the material (Fig. 1.9(b)). Spin-orbit interactions bend the electron orbits of spin-polarized up-spin and down-spin electrons flowing through the ferromagnetic metal in opposite directions. The result is a net charge accumulation, which appears as an anomalous Hall voltage.

On the other hand, a similar phenomenon occurs in a paramagnetic material with an electric current. By analogy with the Hall effect or anomalous Hall effect, the electrons are not spin-polarized and therefore do not experience charge accumulation (Hall voltage), but spin-orbit interactions cause up-spin and down-spin electrons to be bent in opposite directions. This means that a net spin current is

$$j_j^i = \theta_{\mathrm{SH}} \epsilon^{ijk} j_k \tag{1.144}$$

where i is the direction of spin polarization, and j is the direction of the spin current, and k is the direction of the current j_k. It is induced in a direction orthogonal to both the direction of electron spin polarization and the current. This phenomenon is called the spin Hall effect, and the efficiency of the conversion from the current to the spin current is expressed by the spin Hall angle θ_{SH} (Fig. 1.9(c)). Using the electrical conductivity in the current direction and the Hall conductivity σ_{xx}, we obtain $\theta_{\mathrm{SH}} = \sigma_{xy}/\sigma_{xx}$, where $j = y$ and $k = x$. The excitation of the quasi-spin current by the spin Hall effect causes an inverse spin accumulation at each end of the sample, which is balanced with spin diffusion and spin relaxation to reach a steady state. This spin accumulation was measured by the optical method (Kerr effect) [66, 67]. Since the spin current has a time-reversal symmetry, the spin Hall effect occurs without breaking the time-reversal symmetry by applying a magnetic field to the sample. The spin Hall effect has played an important role in spintronics because the spin current can be generated without the use of ferromagnetic materials.

The notion of the spin Hall effect has been discussed since electron scattering via spin-orbit interactions with impurities was proposed by Dyakonov *et al.* The concept of the spin Hall effect has been discussed [48, 49, 50]. The microscopic mechanism of the spin Hall effect can be divided into two main categories: an intrinsic mechanism that originates from the spin-orbit interaction from the solid's band structure (Fig. 1.11(a)), and an extrinsic mechanism that originates from the spin-orbit interaction around impurities. There are two further interpretations of the exogenous mechanism, called the side-jumping mechanism (Fig. 1.11(b)) and the skew scattering mechanism (Fig. 1.11(c)). One can determine which of the side-jumping or skew scattering mechanism is more dominant by examining the relationship between the diagonal term of the resistivity tensor ρ_{xx} and the non-diagonal term (Hall resistivity) ρ_{xy}

If the $\rho_{xx} \propto \rho_{xy}^2$, it is a side jump and If the $\rho_{xx} \propto \rho_{xy}$, it is a skew scattering mechanism.

The side-jump mechanism is caused by the electric field generated by the impurity potential $V_{\rm imp}(\boldsymbol{r})$ in which the electrons in motion in $V_{\rm imp}(\boldsymbol{r})$ feel the spin-orbit interaction

$$\mathcal{H}_{\rm SO} = \eta_{\rm SO}(\boldsymbol{\sigma} \times \nabla V_{\rm imp}(\boldsymbol{r})) \cdot \boldsymbol{p} \tag{1.145}$$

where $\eta_{\rm SO}$ is the spin-orbit coupling constant, and $\boldsymbol{\sigma}$ is the Pauli matrix, and $\boldsymbol{p}$ is the momentum operator. The velocity of the electrons is found to be

$$\boldsymbol{v} = \frac{\partial \mathcal{H}}{\partial \boldsymbol{p}} = \frac{\boldsymbol{p}}{m} + \eta_{\rm SO}(\boldsymbol{\sigma} \times \nabla V_{\rm imp}(\boldsymbol{r})). \tag{1.146}$$

The second term on the right side is called the anomalous velocity, which causes the electron to add a shift in the velocity vector depending on the spin direction. On the other hand, the skew scattering mechanism is that when the impurity contains spin-orbit interactions, the non-diagonal σ_{xy} term arises from the first term, which generally gives the conductivity tensor's diagonal term σ_{xx}. In this case, the effect of the spin-orbit interaction is reflected through the nonequilibrium of the Fermi distribution function that appears in taking the expected value of the first term. This non-equilibrium corresponds to the scattering term in the Boltzmann equation.

Inverse spin Hall effect

The inverse spin Hall effect is the inverse process of the spin Hall effect described in the previous section, i.e., the conversion of spin current in a material into conduction current. The inverse spin Hall effect was first observed experimentally by several groups at the same time in 2006 using the non-local method and spin pumping method [51, 52, 53]. It has already been confirmed experimentally that the conversion efficiency from the spin current to the conduction current is expressed in terms of the spin Hall angle $\theta_{\rm SHE}$. The inverse spin Hall effect in the materials which have large $\theta_{\rm SH}$ ($\theta_{\rm SH} = 0.08$ in Pt and $\theta_{\rm SH} = 0.113$ in Au) allows us to detect the spin current and spin accumulation as an electrical signal with high sensitivity. However, since the spin current injected into these materials disappears within a distance of the spin diffusion length, it is necessary to fabricate thin-film samples to detect the spin current and spin accumulation. In my study, we use the inverse spin Hall effect in NbN thin films containing Nb which has a large spin Hall effect [89], to detect spin currents and spin accumulation.

1.6.3 Spin pumping and spin Seebeck effects

First, the concept of spin pumping as a method of spin injection in a paramagnetic/ferromagnetic junction will be explained. Next, we will show that a spin current flows at the interface of the junction when a temperature gradient is applied (spin Seebeck effects). At the interface, spin-flip scattering of conduction electrons through $s-d$ exchange interactions excites the magnon in the ferromagnet. Using linear response theory and the fluctuation-dissipation theorem, the spin flow across

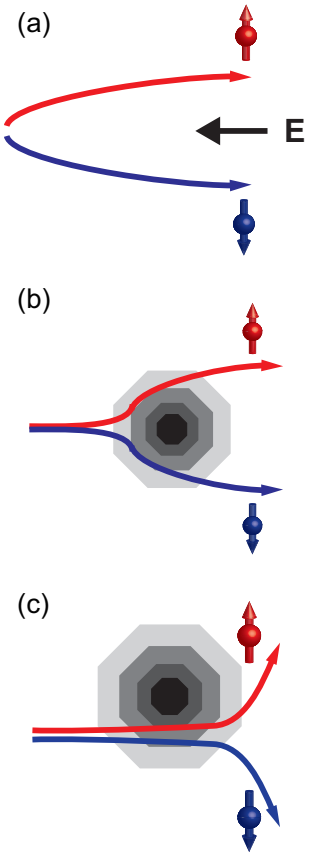

Figure 1.10 Schematic representation of the different spin hall effect mechanisms: (a) intrinsic Spin Hall Effect, (b) Side-jump scattering, and (c) Skew scattering.

the interface can be described theoretically by the thermal non-equilibrium of the combined layer.

Spin pumping

As for the interaction between magnetization and spin currents, (1.123) shows that spin current induces a temporal change of magnetization. This is especially for the perpendicular component of magnetization when the spin current flows through the magnetization. It tends to move in the opposite direction of the spin polization, receiving the change. This effect is called the spin transfer torque [39]. Utilizing this effect, it is analogous that spin angular momentum from the ferromagnet to the conduction electron via the spin transfer torque when the magnetization dynamics is spatially modulated.

The dimentionless damping parameter α in LLG equation is important to describe the effect of the torque. It is expressed as $\alpha = G/\gamma M_s$ using the saturation magnetization M_s and the Gilbert damping constant G. The magnitude of the Gilbert damping torque is proportional to G. The s-d model derived by Heinrich *et al.* [45]

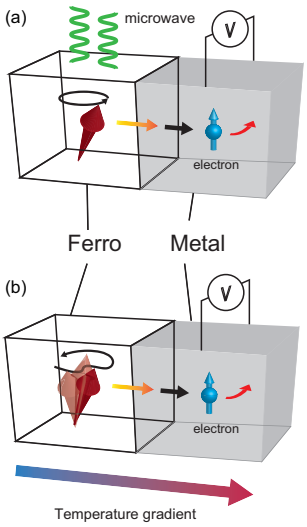

Figure 1.11 Schematic illustration of (a) spin pumping and (b) spin Seebeck effect. The conversion of a spin current into a charge current via the inverse spin Hall effect is also illustrated.

modelled α, while Kambersky *et al.* applied it to the itinerant d electron and led to

$$\alpha = \frac{1}{\gamma M_s} \cdot \frac{\mu_B^2 D(E_F)}{\tau_{sf}}, \tag{1.147}$$

where μ_B is the Bohr magneton, $D(E_F)$ is the total density of states on the Fermi surface, and τ_{sf} is the spin relaxation time of the d electron. At a certain temperature, the $\uparrow$ ($\downarrow$) electrons in the metal are hybridized with the $\downarrow$ ($\uparrow$) electrons due to the spin-orbit interaction. The rate of this hybridization is proportional to the magnitude of the spin-orbit interaction, ξ_{s0}, and inversely proportional to the energy difference between the bands on the order of ξ_{s0}/Δ. When electrons are scattered by phonons and various defects, they are inverted with a probability of $(\xi_{s0}/\Delta)^2$ and it can be expressed as

$$\frac{1}{\tau_{sf}} \approx \frac{(\xi_{s0}/\Delta)^2}{\tau} \approx \frac{(g-2)^2}{\tau} \tag{1.148}$$

where g is the g factor of the electron spin, and τ is the relaxation time of the electron. Here, we assume $\xi_{s0} \approx (g-2)$. Finally, the Gilbert-dumping constant G is derived from the equations (1.147)、(1.148) by

$$G = \alpha \gamma M_s = \frac{\mu_B^2 D(E_F)(g-2)^2}{\tau}. \tag{1.149}$$

Spin pumping was first reported by Silsbee *et al.* in 1979 [54] in experiments with conduction electron spin resonance and simultaneously proposed the phenomenological *s*-*d* model. It is reported that the G of a magnetic film is greatly increased when a non-magnetic film is combined to a magnetic film. The magnetic relaxation as a probe of spin current is reaffirmed in [43, 44]. This increase in G due to spin pumping is strongly dependent on the spin relaxation in the N layer. We discuss the spin pumping phenomenon more quantitatively, following the model calculations of Tserkovnyak *et*

al.[55, 56, 57]. The spin flow from the ferromagnet into the metal layer (N layer) is denoted as $\boldsymbol{J}_s^{\rm pump}$. The spin accumulated in the N layer due to the flow of spin into the N layer decreases as it leaves the interface, but a part of it is called the backflow to the F/N interface as the opposite spin current $\boldsymbol{J}_s^{\rm back}$. This difference $\boldsymbol{J}_s$ can be approximately represented as

$$\boldsymbol{J}_s = \boldsymbol{J}_s^{\rm pump} - \boldsymbol{J}_s^{\rm back} = \frac{\hbar}{4\pi} g^{\uparrow\downarrow} \left\{ 1 + \frac{g^{\uparrow\downarrow}}{g_N \tanh(L/\lambda_{sd})} \right\}^{-1} \boldsymbol{m} \times \frac{d\boldsymbol{m}}{dt}, \tag{1.150}$$

where $g^{\uparrow\downarrow}$ corresponds to the real part of the quantity called the mixing conductance, and g_N is the conductance of the N layer, and L is the thickness of the N layer, and λ_{sd} is the diffusion length of the spin current. In the LLG equation, the additional damping constant α' due to spin current is then written as

$$\alpha' = \frac{G'}{\gamma M_s} = \frac{g_L \mu_B}{4\pi M_s V} g^{\uparrow\downarrow} \left\{ 1 + \frac{g^{\uparrow\downarrow}}{g_N \tanh(L/\lambda_{sd})} \right\}^{-1}. \tag{1.151}$$

For example, if the N-layer is Cu with $\lambda_{\rm sd} = 350$nm, L is reduced to $\lambda_{\rm sd}$, which in turn yields a dumbing constant of $\alpha'(G') = 0$. On the other hand, if the N layer is Pt with $\lambda_{\rm sd} = 14 \pm 6$, and L is much larger than this, then the brace in the formula is $1 + g^{\uparrow\downarrow}/g_N$. Let's put the terms as

$$\frac{1}{g^{\uparrow\downarrow}} + \frac{1}{g_N} = \frac{1}{g_{\rm eff}^{\uparrow\downarrow}}, \tag{1.152}$$

and Eq. (1.151) is then

$$\alpha' = \frac{g_L \mu_B}{4\pi M_s S d} g_{\rm eff}^{\uparrow\downarrow}. \tag{1.153}$$

$g_{\rm eff}^{\uparrow\downarrow}$ is the value called the effective conductance, and the equation represents the sum of the resistance in the ferromagnetic layer ($1/g^{\uparrow\downarrow}$) and the resistance of the N layer ($1/g_N$). The Gilbert damping constant is not a material parameter, but strongly depends on the material in contact with the material; the spin relaxation in the N layer is thought to be due to spin-flip scattering due to spin-orbit coupling. Thus, the spin relaxation of heavy metals and transition metals with d electronic states in the Fermi level is expected to be intense.

A typical set-up of spin pumping is as follows. When a parallel magnetic field is applied to a nonmagnetic metal/ferromagnetic bilayer film, magnetic moments in the ferromagnetic layer precess according to (1.12). If an alternating magnetic field (e.g. microwave) of the same frequency of the precession is applied, the amplitude of the precession becomes resonantly large (ferromagnetic resonance, FMR) and a spin current is injected into the combined thin metal film. The injected spin current can be measured by converting it into a voltage by the inverse spin Hall effect.

Spin Seebeck effects (SSEs)

Spin Seebeck effects are phenomena in which a temperature gradient applied in ferromagnetic and paramagnetic junctions induces a spin current at the junction's interface, similar to conventional spin pumping. It is firstly reported in [58] as the

transvers spin Seebeck Effects. Subsequently, the longitudinal spin-Seebeck effects were discovered. Since they are relatively easy to apply a uniform temperature gradient and transvers spin Seebeck Effects are difficult to separate superimposed signals originated from conventional thermoelectric and thermomagnetic effects, measurements of longitudinal spin Seebeck effects are becoming the mainstream. This study also uses the longitudinal spin Seebeck arrangement (see below).

The theory of the spin Seebeck effect has made great progress since Xiao *et al.* [73] formulated the magnon drive mechanism in 2010, and various theoretical studies have been done since then. In our study, we formulate the spin Seebeck effect using linear response theory based on the theory of Adachi *et al.* [75] Spin current through the interface is represented by the dynamic susceptibility of the two combined layers.

We have also been considering only conduction spin current, but now we will consider spin pumping from spin-wave spin current by localized magnetization movements to conduction spin current. Consider the case where a paramagnetic material (N) is in contact with a ferromagnetic insulator (FI). Due to the huge bandgap at the Fermi energy in the ferromagnetic insulator, the electrons are reflected at the interface. In the scattering process, the electrons are spin-flipped from up to down and down to up due to the interaction of the interface, with the magnons being absorbed or emitted in the FI. Spin-flip scattering including magnon excitation produces a transport of spin angular momentum between the FI and N. At equilibrium, where the temperatures of the FI and N are equal, the scattering process is in equilibrium and the spin current does not flow at the interface; at non-equilibrium conditions where there is a temperature difference between the FI and N, one side of the spin-flip scattering becomes dominant. Spin currents are produced at the interface.

To formulate it, we consider the exchange interaction between electron spins and localized spins at the ferromagnetic/paramagnetic interface (e.g., the exchange interaction between a $3d$ electron, which is the carrier of the magnetic moment, and a conduction electron from a s electron). Suppose that the electron spins are spin-flip-scattered at the ferromagnetic/paramagnetic interface and the spins are excited in the ferromagnetic body (magnon creation or annihilation). Considering the situation, the Hamiltonian which indicates s-d exchange interaction at the interface, including the Fourier transformation, can be written as

$$\mathcal{H}_{sd} = \frac{J_{sd}}{N_a}\sum_{n=1}^{N_I}\int d^3r \boldsymbol{S}_n \cdot \phi^\dagger_{\sigma'}(\boldsymbol{r}_n)\boldsymbol{\sigma}_{\sigma\sigma'}\phi_\sigma(\boldsymbol{r}_n) \tag{1.154}$$

$$= J'_{sd}\sum_{\boldsymbol{k}\boldsymbol{k}'\boldsymbol{q}}[S^\dagger_{\boldsymbol{q}}c^+_{\boldsymbol{k}'\downarrow}c_{\boldsymbol{k}\uparrow} + S^-_{\boldsymbol{q}}c^\dagger_{\boldsymbol{k}'\uparrow}c_{\boldsymbol{k}\downarrow} + S^z_{\boldsymbol{q}}(c^\dagger_{\boldsymbol{k}'\uparrow}c_{\boldsymbol{k}\uparrow} - c^\dagger_{\boldsymbol{k}'\downarrow}c_{\boldsymbol{k}\downarrow})]\rho_{\boldsymbol{q}-\boldsymbol{k}'+\boldsymbol{k}}. \tag{1.155}$$

where the constants are determined as

$$J'_{sd} = \frac{J_{sd}}{N_e\sqrt{N_s}} \tag{1.156}$$

$$\rho_{\boldsymbol{q}-\boldsymbol{k}'+\boldsymbol{k}} = \sum_{n=1}^{N_I} e^{i(\boldsymbol{q}-\boldsymbol{k}'+\boldsymbol{k})\cdot\boldsymbol{r}_n}. \tag{1.157}$$

J_{sd} is the magnitude of the exchange interaction at the interface, N_I is the number of localized moments per unit area at the interface, and N_a is the number of lattices. A spin current operator $\hat{J}^s_{N/F}(t)$ is

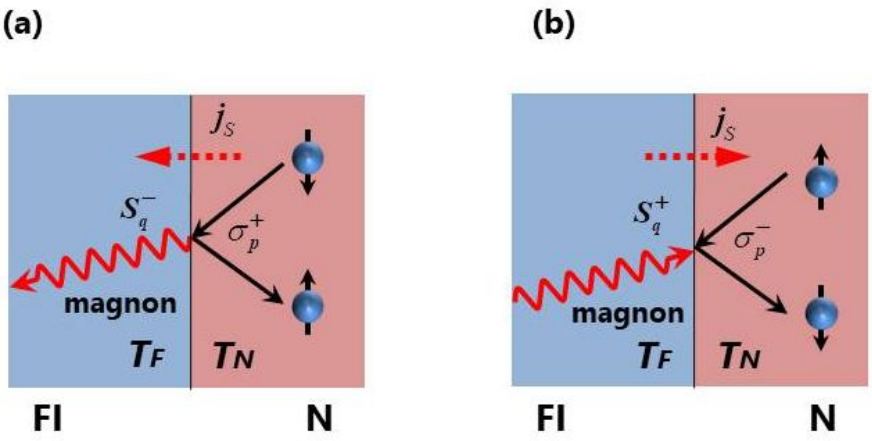

Figure 1.12 Schematic illustration of the angular momentum exchange in the presence of thermal spin pumping at the interface between a ferromagnetic and paramagnetic body. The case of (a) $T_N > T_F$ and (b) $T_F > T_N$.

$$\hat{J}^s_{N/F}(t) = \frac{d}{dt}(N_e^{\uparrow} - N_e^{\downarrow})$$
$$= \frac{2i}{\hbar} J'_{sd} \sum_{\boldsymbol{k}\boldsymbol{k}'\boldsymbol{q}} [e^{-i(\delta\mu/\hbar)t} c^{\dagger}_{\boldsymbol{k}\uparrow}(t) c_{\boldsymbol{k}'\downarrow}(t) \boldsymbol{S}^-_{-\boldsymbol{q}}(t) \rho^*_{\boldsymbol{q}-\boldsymbol{k}'+\boldsymbol{k}} - e^{i(\delta\mu/\hbar)t} c^{\dagger}_{\boldsymbol{k}'\downarrow}(t) c_{\boldsymbol{k}\uparrow}(t) \boldsymbol{S}^+_{\boldsymbol{q}}(t) \rho_{\boldsymbol{q}-\boldsymbol{k}'+\boldsymbol{k}}] \quad (1.158)$$
$$N_e^{\sigma} = \sum_{\boldsymbol{k}} c^{\dagger}_{\boldsymbol{k}\sigma} c_{\boldsymbol{k}\sigma}. \quad (1.159)$$

Here, the spin-flip scattering at the interface of electrons in a normal conductor produces a change of spin-polarized chemical potential as $\delta\mu = \mu_{\uparrow} - \mu_{\downarrow}$. Therefore, the spin current J^z_{sx} generated at the interface by the spin pumping is

$$J^s_{N/F} = -\frac{i}{\hbar} \int_{-\infty}^{t} dt' \, \langle [\hat{J}^z_{sx}(t), \mathcal{H}_{sd}(t')] \rangle \quad (1.160)$$
$$= \frac{2}{\hbar^2} N_I J'^2_{sd} \sum_{pq} \int_{-\infty}^{\infty} dt e^{i\delta\mu t} \langle S^-_{-q}(t) S^+_q(0) \rangle \langle \sigma^+_p(t) \sigma^-_{-p}(0) \rangle$$
$$- \frac{2e}{\hbar^2} N_I J'^2_{sd} \sum_{pq} \int_{-\infty}^{\infty} dt e^{-i\delta\mu t} \langle S^+_q(t) S^-_{-q}(0) \rangle \langle \sigma^-_{-p}(t) \sigma^+_p(0) \rangle \quad (1.161)$$

using linear response theory. Furthermore, from the fluctuation-dissipative theorem, the correlation function can be written in the imaginary part of the dynamical spin susceptibility, which yields

$$\int_{-\infty}^{\infty} e^{i\omega t/\hbar} \langle S^+_q(t) S^-_{-q}(0) \rangle = -2\hbar[n(\omega, T_\alpha) + 1] \mathrm{Im}\chi^{+-}_F(q, \omega), \quad (1.162)$$
$$\int_{-\infty}^{\infty} e^{i\omega t/\hbar} \langle S^-_{-q}(t) S^+_q(0) \rangle = -2\hbar n(\omega, T_\alpha) \mathrm{Im}\chi^{+-}_F(q, \omega), \quad (1.163)$$
$$\int_{-\infty}^{\infty} e^{-i\omega t/\hbar} \langle \sigma^+_p(t) \sigma^-_{-p}(0) \rangle = -2\hbar[n(\omega, T_\alpha) + 1] \mathrm{Im}\chi^{+-}_N(p, -\omega), \quad (1.164)$$
$$\int_{-\infty}^{\infty} e^{-i\omega t/\hbar} \langle \sigma^-_{-p}(t) \sigma^+_p(0) \rangle = -2\hbar n(\omega, T_\alpha) \mathrm{Im}\chi^{+-}_N(p, -\omega). \quad (1.165)$$

Since $n(\omega, T_\alpha) = 1/[\exp(\hbar\omega/k_B T_\alpha) - 1]$ is the Bose distribution function and $\chi^{+-}_{F,N}$ is the dynamic spin susceptibility, we can rewrite J^z_{sx} as

$$J^z_{sx} = \frac{4e}{\pi} N_I J'^2_{sd} \sum_{pq} \int_{-\infty}^{\infty} d\omega [n(\omega, T_F) - n(\omega + \delta\mu/\hbar, T_N)] \times \mathrm{Im}\chi^{+-}_F(q, \omega)\mathrm{Im}\chi^{+-}_N(q, \delta\mu + \omega). \quad (1.166)$$

Thus, spin currents generated by spin-pumping, such as those induced by microwave ferromagnetic resonance or thermal excitation (the distribution function changes between ferromagnetic and paramagnetic materials depending on the temperature difference), can be expressed as the imaginary component of the dynamical spin susceptibility, as represented by Eq. (1.166). It is found that the current depends on the $\mathrm{Im}\chi(\boldsymbol{q}, \omega)$. In equilibrium ($\delta\mu = 0, T_F = T_N$), the spin current does not flow in the state.

1.6.4 Spin transport and spin-to-charge conversion in conventional superconductor

The most characteristic feature of spin transport in superconductors is that in the conventional s-wave superconductors, the spin transport is carried by quasiparticles whose single-particle excitations are represented by the Bogolubov transformation. The spin transport is carried by quasiparticles rather than electrons, except in the spin-triplet state. As seen in the Bogolubov transformation, the Bogolubov quasiparticle is represented as a superposition of electronic and hole excitations, and the charge of the Bogolubov quasiparticle is in the intermediate state between $-e$ and e. In equilibrium, there is an equal number of electron and hole quasiparticles. However, spins or electrons are injected into the superconductor from the other system, the system goes into a non-equilibrium state and the number of quasiparticles for each branch changes. This non-equilibrium state causes spin-induced or charge-induced imbalance

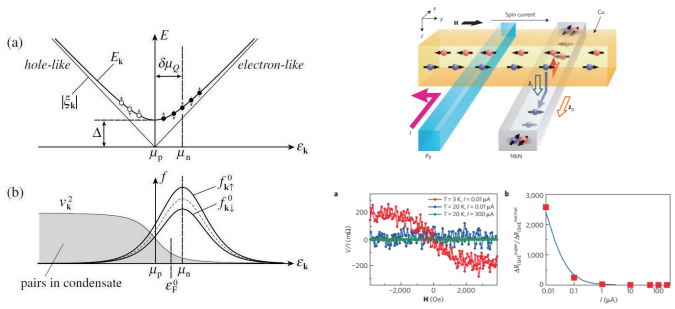

Figure 1.13 (Left) Distribution functions of quasiparticles in a superconductor with (a) non-equilibrium excitation spectra and (b) up-spin and down-spin quasiparticles, respectively. A spin-derived chemical potential shift, $\delta\mu_Q$, exists in the non-equilibrium state where up-spin excitations are abundant and (Right) Experimantal observation of qusiparticle inverses spin Hall effect in non-local setup [Reprinted from S. Takahashi and S. Maekawa, Phys. Rev. Lett. **88**, 116601 (2002) and T. Wakamura et al., Nature material 14 (2015)].

effect, which relaxes on a certain time scale (τ_Q) or spatial scale (λ_Q).

In addition to characteristic phenomena such as the imbalance effect in Bogolubov quasiparticles, the superconducting gap is also involved in spin transport in superconductors. Based on the discussion in semiconductors, the resistance of quasiparticles is proportional to $(f_0(\Delta))^{-1}$, where $f_0(E) = ((\Delta))^{-1}$. where $f_0(E) = (\exp(E/k_BT) + 1)^{-1}$ is the Fermi distribution function. Due to the energy gap, the number of quasi-particles decreases with decreasing temperature. This effect affects not only the charge transport properties, but also the spin transport properties, as recently shown by the non-local spin injection [72].

1.7 Purpose of this thesis

Recent advances in experimental techniques of thin film deposition and lithography have led to various experiments for coherent spin transport phenomena, such as at the superconductor interface or spin waves in the planar cavity. In this thesis, we further examine this coherent spin dynamics via YIG coupled systems (superconductor in *Chapter 3* and cavity's mode in *Chapter 4*) to realize the coherent state. Below, we elaborate on these purposes and show the outline of this thesis.

Chapter 2 describes the sample characteristics in terms of crystallographic structure and fabrication and simulation process, and measurement technique, including their physical backgrounds.

Chapter 3 denotes spin dynamics in superconductor/YIG systems.

Spin dynamics, referring to the dynamic spin susceptibility, in superconductors has been investigated mainly from the temperature dependence of the nuclear-spin relaxation rate via nuclear magnetic response or AC conductivity measurement in previous studies. Here, we perform temperature dependence of SSE measurement in NbN thin film/YIG bilayer system. Around the superconducting transition temperature, its signal shows the anomalous peak structure, which cannot be explained by the normal SSE in conventional paramagnetic metal/YIG systems. In the theoretical considerations based on the linear response theory, the numerical results were obtained to reproduce the experimental results.

Chapter 4 suggests the discovery of hybridization control between YIG and planar resonator photons.

Magnons in a magnetic material can be coupled with cavity's photons when their mode volumes are overlapping. In a strong coupling regime, it makes the level repulsion and creates coherent hybridized states called, the cavity-magnon-polaritons (CMPs). On the other hand, they also make the specific structure even in the weak coupling regime. In this study, we have investigated the control of the magnon-photon coupling strength between YIG film and omega-shaped resonator by changing magnetic field angles and strengths. We found that the effective coupling exhibits pronounced change around the critical angle where the nonlinear spin dynamics appeared. It enables us to control the interference in dynamical spins and the photon

mode.

Chapter 5 is devoted to summarize our results and comments on their importance.

Chapter 2

Experimentals

2.1 Sample material

2.1.1 Ferrimagnetic insulator $Y_3Fe_5O_{12}$

Here, we focus on the structure and properties of yttrium iron garnet ($Y_3Fe_5O_{12}$: YIG) as a ferrimagnet. YIG is one of the rare-earth iron garnets ($R_3Fe_5O_{12}$: RIG) and is a typical Garnett-type ferrite. The crystal structure of YIG is shown in Fig. 2.1. The lattice constant is $a = 12.376\mathring{A}$ and the crystal structure is cubic with a complex structure containing 160 atoms in a unit cell (with 8 compositional formulas). We find that magnetic Fe^{3+} ions are at the 16a and 24d sites, and Y^{3+} ions are at the 24c site. They are octahedral, tetrahedral, and dodecahedral 96h sites via O^{2-} ions, respectively. Fe^{3+} exhibits antiferromagnetically coupled ferrimagnetic properties. This is due to the superexchange interaction between Fe^{3+} and O^{2-}.

It is a Mott insulator with a large band gap to [81, 82] and an electrical resistivity on the order of $10^{13}\Omega$cm [83], so that the proximity effect can be almost negligible even when superconductors are combined as mentioned earlier. YIG behaves as a ferrimagnetic insulator with high curie temperature, 560 K [7]. A typical saturation magnetization is $M_s = 0.178$ T. Spin density is about $4.22 \times 10^{27}\mathrm{m}^{-3}$. An exchange constant α is 3×10^{-12} cm^2[6]. The half-width of the spectrum due to ferromagnetic resonance is very narrow (about 0.05 mT), resulting in very small magnetic relaxation and long magnon life times (small magnetic losses). The crystal magnetic anisotropy is very small and the spin-excitation gap energy is known to be in the range of a few tens of μeV.

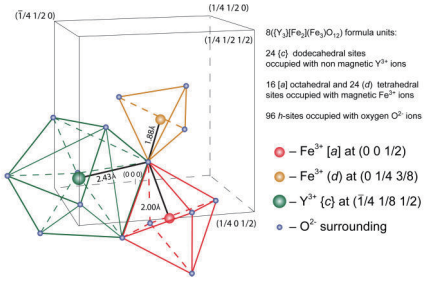

Figure 2.1 Crystal structure of YIG [6]

Liquid Phase Epitaxy (LPE)

Liquid Phase Epitaxy (LPE) is a technique for forming thin films on a substrate by immersing the substrate in molten lead flux and adjusting the temperature to take advantage of the supersaturated state. It is used to prepare the ferromagnetic insulator yttrium iron garnet, which is used in this study. A paramagnetic gadolinium gallium garnet (GGG) with the same garnet-type crystal structure was used to fabricate a thin film of YIG with a lattice constant of $12.329\mathring{A}$ and a lattice constant of GGG very close to $12.383\mathring{A}$, which is known to produce a good quality of crystalization. The investigated sample of cavity experiments is a $t = 1.4$ and 5 μm thick YIG film grown by liquid phase epitaxy on gadolinium gallium garnet (GGG). They are provided by Carsten Dubs from the INNOVENT e.V. Technologieentwicklung, Germany. The samples with lateral dimensions 5×5 mm were taken in the same crystal.

2.1.2 Type-II superconductor NbN

A thin film of niobium nitride (NbN) was used for spin injection into the superconductor, which is a conventional s-wave superconductor with a magnetic field penetration length λ of about 250 nm, and an electronic mean free path l of 1∼4Å in bulk NbN, and a coherence length of ξ_0 of about 4 nm. It is therefore known as an extremely dirty $(l \ll \xi_0)$ and type-II $(\xi_0 < \lambda)$ superconductor with an fcc crystal structure like NaCl. Although the superconducting transition temperature (T_c) is lower than that of high-temperature oxide superconductors, it has relatively high critical fields H_{c2} and are good for studying their transport properties with superconductivity because it also features the formation of magnetic field vortices with an applied external magnetic field. It is also a typical full-gap superconductor with a spin singlet so that BCS theory can be rigorously applied to its analysis.

Sample preparation, film fabrication, and evaluation

It is essential to control the film properties of NbN for the superconducting properties and chemical composition ratios, such as critical current, surface roughness, grain size, and film stress. It is known that NbN thin films epitaxially grown directly on dielectric films such as SiO and SiO_2 are polycrystalline films with poor lattice matching. Decrease of the superconducting transition temperature T_c and increase of the resistivity, which is thought to be due to the grain boundaries, occur in the polycrystaline structure. In the present experiment, however, T_c should be high enough not to destroy the superconducting state under the temperature gradient. This study aims to produce a NbN film on YIG with relatively high T_c compared to the bulk NbN. T_c of bulk NbN reported in the previous study is around 16 K.

NbN was epitaxially grown on the substrate under high vacuum ($< 2.0 \times 10^{-5}$Pa) and by reactive DC magnetron sputtering. The deposition was performed at room temperature and the pure Nb (5N) target was used. The deposition conditions were fixed at 100 W of power and 15 sccm of Ar flow rate folllowing the reference [86]. The

Figure 2.2 ULVAC, QAM4-STS used for the NbN deposition

nitrogen flow rate was controlled to provide the best film quality conditions. There is a difference in sputtering response between increasing and decreasing the N_2 flow rate. This is called the hysteresis effect, which results in abnormality of the voltage applied between sample and target with different N_2 flow rate. Other parameters have also been described in the literature as anomalies in the internal pressure or film deposition rate, and it is claimed that the N_2 flow conditions to produce high T_c NbN films are the values at which the voltage and sputtering pressure begin to increase rapidly.

The deposition was performed on a silicon substrate for dummies. First, by presputtering for 4 min, we removed contamination of the target's surface, and then increased the N_2 flow rate from 0 sccm to 8 sccm. The reverse bifurcation of the hysteresis curve was determined by decreasing the N_2 flow rate by the same increment.

With respect to the results, we could not confirm a clear hysteresis of the target voltage as claimed in the literature. However, when comparing voltage, total pressure, and deposition rate, a slight change was confirmed at a flow rate of around 2 sccm of N_2, so the condition of the sample with the highest T_c when varying the flow rate as 2 sccm was set as the optimal condition. The temperature dependence of the resistance of the each N_2 flow rates are shown in Fig. 2.5. Film thickness was set to 20 nm because of the spin-diffusion length l_{sf} of NbN is 7 nm, and the balance between the film thickness and T_c (of course the thinner the film, the lower the T_c). AFM image is also shown in Fig. 2.6. We can see that the surface roughness of the NbN film on YIG is less that 2 nm, which is enough small compared to the film thickness and l_{sf}.

2.1.3 Measurement set-up of the spin Seebeck effect (SSE)

In this section, we describe the experimental system for applying the temperature gradient to measure the spin Seebeck effect. A physical property measurement system (PPMS) was used for low-temperature measurements, which has a superconducting magnet applying magnetic field perpendicular to the floor. The magnetic field can be applied up to 9 T. The PPMS used in this study is shown in the figure 2.7.

The sample holder is made of aluminium nitride (AlN) and sapphire (Al_2O_3), which

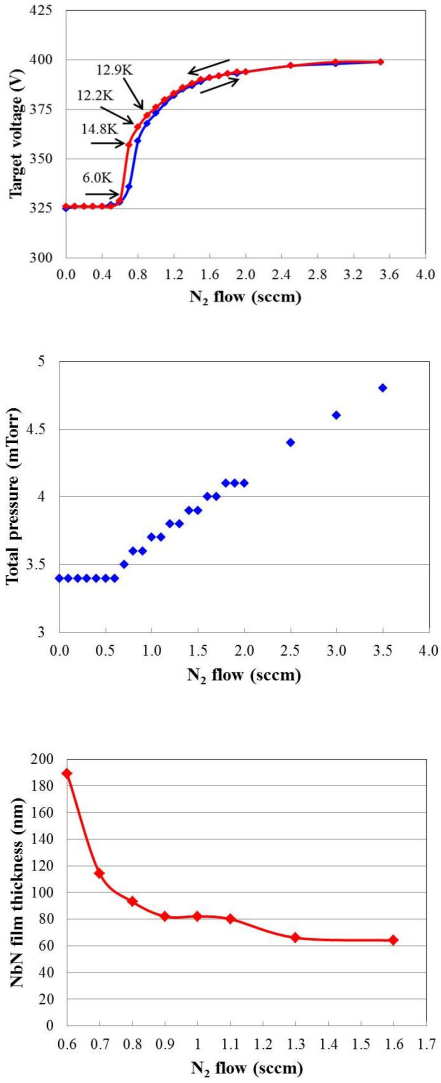

Figure 2.3 Nitrogen flow rate and literature values for each parameter[86].

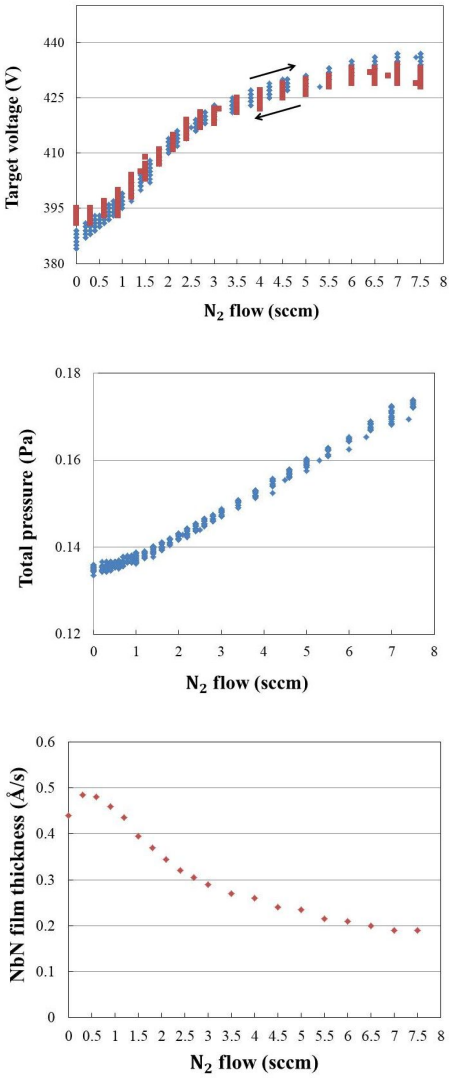

Figure 2.4 Experimental values for each parameter with the nitrogen flow rate.

has a very high thermal conductivity of about 150 W/mK, and works as a heat bath because it is much higher than the thermal conductivity of YIG (a few W/mK). The sample holder is made of two superconductor film/insulator composite structure samples sandwiched between two AlN sheets. Ceramic screws with low thermal conductivity are used to clamp the sample. The AlN and Al_2O_3 are in thermal contact with the PPMS pack, and the temperature can be controlled in the range of $5-300$ K with the PPMS temperature controller. On the other hand, a chip heater is attached to the AlN at the top. The chip heater has a very small magnetoresistance even in high magnetic fields and applies a constant current to the sample to apply a steady temperature gradient in the vertical direction. This temperature difference was read from the electromotive signals of two E-type (Chromel/Constantan) thermocouples connected to the differential, read by a nano voltmeter (KEITHLEY 2182A) and

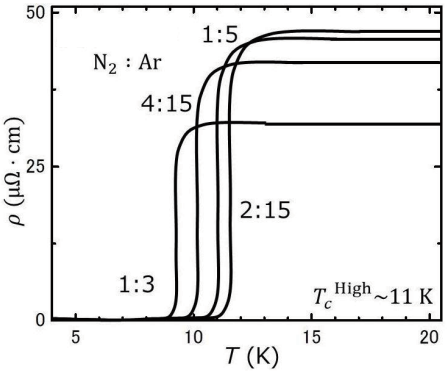

Figure 2.5 Temperature dependent electrical resistivity of NbN films of the different nitrogen and argon flow rate during NbN deposition.

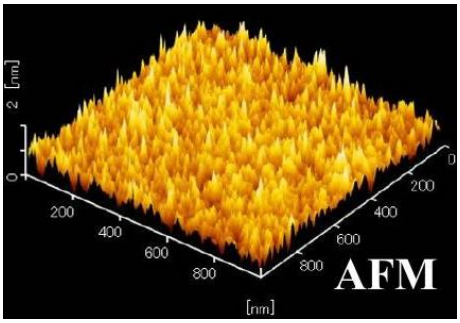

Figure 2.6 Surface roughness of the NbN film on YIG (film thickness: 20nm).

converted from the Seebeck coefficient (see Fig. 2.8)

4-wire resistance measurement

For the 4-wire resistance measurements, the current-applied electrodes were made of deposited Cu along the width of the sample to ensure that the applied current flows uniformly (constant current density on the thin film surface) and the electrodes

Figure 2.7 PPMS used in the experiment. A magnetic field H is applied perpendicular to the floor surface.

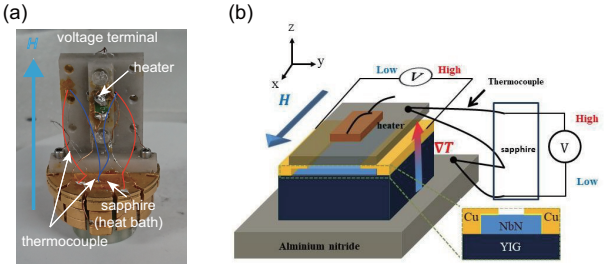

Figure 2.8 Longitudinal SSE measurement setup. (a) Photo of SSE device and (b) structure.

were made thick enough to have an equal potential on the electrodes. The terminals for voltage measurement should be designed to be as small as possible so as not to interfere with the uniform current distribution. In particular, when evaluating the superconducting transition temperature, note that the current distribution near the electrodes is non-uniform, and an increase in current density may cause a temperature increase due to Joule heating, which is estimated to be higher than the actual transition temperature.

2.2 Microwave spectroscopy; measurement technique and simulation in transmission lines

An important type of a transmission line resonator is the coplanar waveguide (CPW) resonator. It is based on CPW transmission lines which are presented as follws. A conventional coplanar waveguide consists of a centre strip conductor with semi-infinite ground planes on either side. Electromagnetic waves can be derived

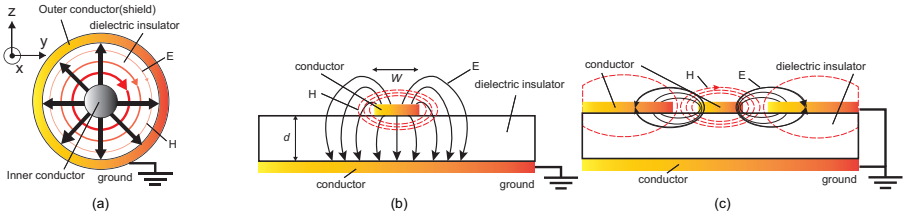

Figure 2.9 Schematic diagram of the distribution of electric (black) and magnetic (red) fields in the cross-sectional view of the transmission line. (a) Coaxial line, (b) microstrip line, and (c) coplanar waveguide.

from Maxwell's equations as the electric and magnetic fields are time-dependent by the angular frequency ω. Maxwell's equations can be written as follows:

$$\nabla \times \boldsymbol{E} = -\frac{\partial}{\partial t}\boldsymbol{B} \tag{2.1}$$

$$\nabla \times \boldsymbol{H} = \boldsymbol{j} + \frac{\partial}{\partial t}\boldsymbol{D}. \tag{2.2}$$

Now consider a coaxial line extending in the x-direction, shown in the figure 2.9(a). The mode of the electromagnetic wave is defined by the distribution of the electric field E and the magnetic field H. Consider the TEM mode of electromagnetic waves propagating along this coaxial line (x-axis). The most basic mode, TEM mode, can be found by solving Maxwell's equations under the condition $E_x = H_x = 0$. There are other modes, such as the TE and TM modes, which are only excited above a certain frequency due to a gap in frequency.

As shown in the figure, the potential difference V between the inner conductor of the coaxial line and the outer conductor at a distance r is found to be as follows with $\boldsymbol{E}_t$ as the internal electric field:

$$V = \int_0^r \boldsymbol{E}_t \cdot d\boldsymbol{r}. \tag{2.3}$$

Subsequent physical quantities with the subscript t mean that they have only y and z components perpendicular to the propagation, x-direction. Also, for the current J_x flowing through the central conductor, integrate the internal magnetic field $\boldsymbol{H}_t$ over the area s of the central conductor and apply Stokes' theorem to integrate it circumferentially over s as

$$J_x = \int_s (\nabla_t \times \boldsymbol{H}_t) \cdot \boldsymbol{e}_x ds = \oint_s \boldsymbol{H}_t \cdot d\boldsymbol{l}. \tag{2.4}$$

The relationship between V and J_x is obtained from the relationship between the electric field $\boldsymbol{E}_t$ and the magnetic field $\boldsymbol{H}_t$. Suppose $\boldsymbol{E}_t$ and $\boldsymbol{H}_t$ are oscillating for time t and position x and are proportional to exp[i(ωt − kx)] with k as the wave-number. So there's a relationship

$$k(\nabla_t \cdot \boldsymbol{E}_t)\boldsymbol{e}_x = \mu\omega(\nabla_t \times \boldsymbol{H}_t) \tag{2.5}$$

between $\boldsymbol{E}_t$ and $\boldsymbol{H}_t$. μ is the permeability in the dielectric material. From the condition of charge continuity in Maxwell's equations

$$\nabla_t \cdot \boldsymbol{E}_t = \frac{q}{c}, \tag{2.6}$$

$$\frac{\partial q}{\partial t} = -\frac{\partial}{\partial x} j_x, \tag{2.7}$$

where q is the charge density. Thus, the current J_x is generated by the flow of charge induced by the potential difference V, and in the transmission line of the TEM mode, its characteristics are determined by the structure in the yz plane. As shown in the cross-sectional view of the coaxial line in the figure, if the capacitance per unit length between the central conductor and the outer conductor is defined as C, the relationship between the charge induced in the conductor and the potential difference is expressed as follows by integrating the charge density over the area s of the central conductor:

$$V = \frac{1}{C} \int_s q ds. \tag{2.8}$$

and

$$V = \frac{\sqrt{\epsilon\mu}}{C} \int_s (\nabla_t \times \boldsymbol{H}_t) \cdot \boldsymbol{e}_x ds, \tag{2.9}$$

where ϵ is the permittivity in the dielectric material. Therefore, compared to (2.2.4), the ratio of potential difference to current is

$$\frac{V}{J_x} = \frac{\epsilon\mu}{C}. \tag{2.10}$$

Here, we define characteristic impedance as

$$Z_0 = \sqrt{\mu\epsilon} = \sqrt{L/C}. \tag{2.11}$$

Therefore

$$|V| = Z_0|J_x|, \ |E| = Z_0|H| \tag{2.12}$$

and wave vector k is described as

$$k = \omega\sqrt{\epsilon\mu}. \tag{2.13}$$

The power carried by the propagation of the electromagnetic field can be determined using the characteristic impedance as

$$P = \frac{1}{2}\frac{|V|^2}{Z_0} = \frac{1}{2}Z_0|J_x|^2. \tag{2.14}$$

The fundamental problem one faces when analyzing transmission lines is to measure voltages and currents directly because they vary significantly along the length of the transmission line (cf. Fig. 2.9). Therefore, the wave quantities are taken into consideration. Let us consider a 2-port network like the one presented in Fig. 2.10. We first apply the incident wave $V_{in,1}$ at the first port, while the second port is terminated with a matched impedance. In this way, no signal is reflected at the second port and we have $V_{in,2}$. The transmission parameter S_{21} is defined as the ratio of the voltage of the transmitted wave $V_{out,2}$ to the incident wave $V_{out,1}$. The reflection parameter S_{11} is the ratio of the reflected wave to the incident wave $V_{in,1}$. The scattering parameters S_{12} andS_{22} are determined by measuring in the opposite direction when the first port is terminated with a matched impedance. We summarize the scattering parameters in the scattering matrix $\boldsymbol{S}$ [8] as follows

$$\begin{pmatrix} V_{out,1} \\ V_{out,2} \end{pmatrix} = \begin{pmatrix} S_{11} & S_{12} \\ S_{21} & S_{22} \end{pmatrix} \begin{pmatrix} V_{in,1} \\ V_{in,2} \end{pmatrix} \tag{2.15}$$

or

$$\boldsymbol{V}_{in} = \boldsymbol{S}\boldsymbol{V}_{out}. \tag{2.16}$$

Define the voltage amplitude of electromagnetic waves propagating in the $x-$axis

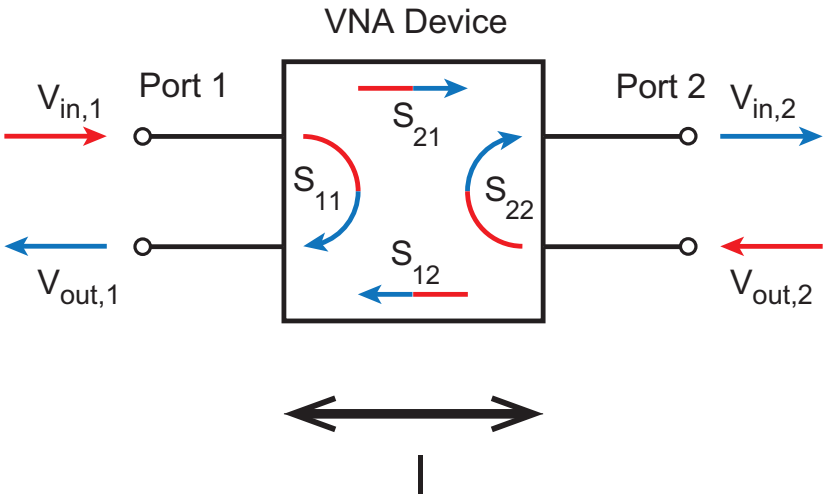

Figure 2.10 Relationship between voltage amplitude and S-parameter in a two-port transmission channel

direction through the transmission channel with wave number k as follows

$$V(x,t) = V_0 e^{i(\omega t - kx)}. \tag{2.17}$$

Within the two-port transmission channel, if the transmission channel is uniform in length l, S_{21} is obtained as

$$\begin{aligned} S_{21} &= V_{out,2}/V_{in,1} \\ &= e^{i(\omega t - k(x+l))}/e^{i(\omega t - kx)} \\ &= e^{i(-kl)}. \end{aligned} \tag{2.18}$$

Similarly, S_{12} is given as $e^{i(-kl)}$. From $S_{11} = S_{22} = 0$,

$$S = \begin{pmatrix} 0 & e^{i(-kl)} \\ e^{i(-kl)} & 0 \end{pmatrix}. \tag{2.19}$$

This is the S-parameter, which represents a uniform transmission path without reflection.

S-parameters expressed in terms of the power that is input and output

$$P_{out} = |S_{21}|^2 P_{in}. \tag{2.20}$$

The energy loss that occurs in ferromagnetic resonance manifests as microwave propagation loss through the transmission line's inductance.

During ferromagnetic resonance, the imaginary component of the sample's magnetic susceptibility affects the imaginary component k'' when the wavenumber k is set to $k = k' - ik''$. In a transmission line of length l, the S parameter is expressed as Eq. (2.18), so if we measure the absolute value of S_{21}

$$|S_{21}| = e^{-k''l} \tag{2.21}$$

From this value, absorption by magnetic materials should be observed. The magnetic susceptibility of the magnetic material is obtained from the equation $\chi = \mathrm{Re}[\chi] - \mathrm{iIm}[\chi]$, then the applied permeability μ_r of the transmission channel with the sample is expressed by using factor a, which depends on the structure of the transmission channel, as follows.

$$\mu_r = 1 + a \cdot \chi \tag{2.22}$$

Since $k = 0k_0\sqrt{\mu_r}$ and the magnetic material's contribution is less than 1, k is

$$k = k_0 \left(1 + \frac{a}{2}(\mathrm{Re}[\chi] - \mathrm{iIm}[\chi])\right). \tag{2.23}$$

Therefore, the imaginary part k'' of k is found to be $k'' = \frac{a}{2}k_0\mathrm{Im}[\chi]$, and by expanding equation (2.23) under the first-order approximation of $\mathrm{Im}[\chi]$, we have

$$|S_{21}|^2 = 1 - a \cdot k_0 l \mathrm{Im}[\chi]. \tag{2.24}$$

If the energy loss associated with the microwave propagation is ΔP, then ΔP can be expressed as $\Delta P = P_{out} - P^0_{out}$, where P^0_{out} is the output power in the absence of ferromagnetic resonance. Then

$$\Delta P = \left(|S_{21}|^2 - |S^0_{21}|^2\right) P_{in} \tag{2.25}$$

where $|S_{21}^0|$ is S_{21} in the absence of ferromagnetic resonance. With the above two equations, The microwave loss due to ferromagnetic resonance can be determined using the magnetic susceptibility as follows:

$$\Delta P = a \cdot k_0 l P_{in} \cdot \mathrm{Im}[\chi] \tag{2.26}$$

so ΔP is found to be proportional to $\mathrm{Im}[\chi]$. Measuring the change in the S parameter allows us to measure the loss of microwaves absorbed by the sample due to ferromagnetic resonance.

2.2.1 Microstrip transmission lines

Transmission lines are structures specialized on transmitting electromagnetic waves at radio frequencies i.e. between several GHz. In the present thesis, we use transmission lines of the microstrip type. Microstrips are planar transmission lines consisting of a conducting strip and a ground plane separated by a dielectric (cf. Fig. 2.9(b)).

As it is presented in Fig. 2.9(b) the electric field lines of the microstrip exist in the dielectric layer as well as in the surrounding medium (here the latter is assumed to be air). As a result, the effective permittivity ϵ_{eff} is between the dielectric constant of the surrounding medium ($\epsilon_{\mathrm{eff}} = 1$) and the dielectric constant of the substrate ϵ_r. For our microstrip ϵ_{eff} is given approximately by [8]

$$\epsilon_{\mathrm{eff}} \approx \frac{\epsilon_r + 1}{2} + \frac{\epsilon_r - 1}{2} + \frac{1}{\sqrt{1 + 12d/W}}, \tag{2.27}$$

where d is the thickness of the dielectric substrate and W is the width of the conducting strip (cf. Fig. 2.9(b)). The characteristic impedance Z_0 of a microstrip line is determined by its geometry and by the effective dielectric constant ϵ_{eff} [8]:

$$Z_0 \approx \begin{cases} \frac{60}{\sqrt{\epsilon_{\mathrm{eff}}}} \ln\left(\frac{8\mathrm{d}}{\mathrm{W}} + \frac{\mathrm{W}}{4\mathrm{d}}\right) & \text{for W/d} \leq 1 \\ \frac{120\pi}{\sqrt{\epsilon_{\mathrm{eff}}}[W/d + 1.393 + 0.667 \ln(\mathrm{W/d} + 1.444)]} & \text{for W/d} \geq 1. \end{cases} \tag{2.28}$$

2.2.2 Ferromagnetic resonance (FMR) condition

The power absorbed in the ferromagnetic material is described by χ'' and close to the FMR at a fixed frequency, it has a Lorentzian lineshape:

$$\chi'' = \frac{A_{\mathrm{sym}} \Delta H^2}{\Delta H^2 + (H_{\mathrm{eff}} - H_{\mathrm{res}})^2} \tag{2.29}$$

where ΔH is the half width at half maximum equal to $\mu_0 \Delta H = \frac{\alpha\omega}{\gamma}$. The absorbed power can then be written $P_{\mathrm{abs}} = \omega \chi'' h_{\mathrm{rf}}^2$. The amplitude of this Lorentzian is inversely proportional to the Gilbert damping α and proportional to the square of the rf magnetic field.

Here, we have to point out that in general a lineshape asymmetry can be observed. This asymmetry has been recently associated with eddy currents generated by the time-varying magnetic field.The phase shift between the rf magnetic field and the eddy

current-induced field will thus distort the resonance shape. The measured lineshape is therefore not perfectly symmetric and has an anti-Lorentzian (dispersive) contribution as

$$\chi'' = A_{\mathrm{sym}} \frac{\Delta H^2}{\Delta H^2 + (H_{\mathrm{eff}} - H_{\mathrm{res}})^2} - B_{\mathrm{asym}} \frac{\Delta H (H_{\mathrm{eff}} - H_{\mathrm{res}})}{\Delta H^2 + (H_{\mathrm{eff}} - H_{\mathrm{res}})^2}. \tag{2.30}$$

Note that the asymmetric part can be large when measuring FMR using stripelines with a strong out of plane component of the RF field on large samples with a thick conductive layer in contact with the ferromagnet. Nonetheless it is negligible when using small samples, especially in the cavity with a homogeneous radiofrequency field in the plane of the sample.

We now describe how to estimate the microwave absorption intensity ΔP by the S parameter. The measurement is performed using S_{21}, which gives the voltage ratio of transmitted microwaves, and the transmission loss between port and CPW is assumed to be equal at port 1 and port 2. Since the S parameter is the ratio of the microwave voltage amplitude, if the input power is defined as P_{in}, then the output The power P_{out} can be determined by

$$P_{out} = |S_{21}|^2 P_{in}. \tag{2.31}$$

Therefore, if there is an absorption of microwaves by the sample, a change

$$\Delta P_{out} = \left(\Delta |S_{21}|^2\right) P_{in} \tag{2.32}$$

in the output power P_{out} is made where $\Delta|S_{21}|^2$ is the change in the $|S_{21}|^2$ spectrum. When there is a loss due to ferromagnetic resonance, $|S_{21}|^2$ can be fitted using

$$|S_{21}|^2(H) = |S_{21}^0|^2 + a(H - H_r) - (\Delta|S_{21}|^2) \frac{(\Delta H/2)^2}{(H - H_r)^2 + (\Delta H/2)^2}. \tag{2.33}$$

The first and second terms are the background that shows the characteristics of the transmission line independent of the sample, and $|S_{21}^0|^2$ is a constant that represents only the background of the ferromagnetic resonance. The second term is a linear approximation of the magnetic field-dependent transmission line characteristics using the constant a. The third term is expressed in terms of a Lorentz-type function, which reflects the change in the magnetic susceptibility P_{abs} at ferromagnetic resonance since the relationship between the magnetic susceptibility P_{abs} and the imaginary part of magnetic susceptibility χ'' is $P_{\mathrm{abs}} = \omega \chi'' h_{rf}^2$ in the case of ferromagnetic resonance. To obtain the microwave absorption ΔP_{abs}, we need to consider the transmission loss from the sample to port 2. This loss is equal to half of $|S_{21}^0|^2$. Therefore, the microwave power ΔP absorbed by the sample is

$$\Delta P = \frac{P_{in}}{|S_{21}^0|} (\Delta |S_{21}|^2). \tag{2.34}$$

In this calculation, we assume that no reflections occur in all transmission lines, but this process is valid because S_{11}, which represents reflections, is about 0.1 in the experiment.

2.2.3 Frequency-sweeping FMR

The resonant frequency depends on both frequency and magnetic field, so both parameters must be swept in FMR. In typical field-sweeping FMR, the frequency is held constant and the magnetic field is swept. The measurement is then repeated for a range of frequencies to obtain f_{res} as a function of both f and $\boldsymbol{B}$. However, in this thesis, a frequency-sweeping FMR technique was used, in which the frequency was swept with a vector network analyzer at a constant magnetic field, with the measurement then repeated for a range of magnetic fields. This technique has the advantage of allowing rapid, broadband FMR measurements by using the VNA rather than field modulation, but it requires a different analysis of the resonant signal, which is produced in the frequency domain rather than the field domain.

The typical Gilbert damping model relates the damping constant α to the FWHM of the resonance peak, swept in the field domain, as [9]

$$\Delta H = \Delta H_0 + \frac{4\pi\alpha f}{|\gamma|} \tag{2.35}$$

Here ΔH_0 describes the inhomogeneous broadening that is a result of sample imperfections. It is ideally zero for a perfect sample, and since it is intrinsic to the sample being measured it is independent of frequency.

To extract α from the frequency linewidth Δf, as found in frequency-swept VNA-FMR, the field line width must be converted into a frequency linewidth by differentiating the Kittel equation (Eq. (1.29)) [10, 11]:

$$\Delta f = \Delta H \frac{\partial f_{\text{Kittel}}(H_{\text{eff}})}{\partial H_{\text{eff}}}\bigg|_{H_{\text{eff=H}_{\text{Kittel(f)}}}} \tag{2.36}$$

Based on the Kittel equation, the frequency linewidth for an out-of-plane magnetized film is a function of f_{res}:

$$\Delta f = 2\alpha f_{\text{res}} + \gamma\mu_0\Delta H_0 \tag{2.37}$$

The square-root dependence of the resonant frequency on the magnetic field for in-plane magnetization produces an inverse square-root shape for the frequency linewidth [12]:

$$\Delta f = (2\alpha f_{\text{res}} + \gamma\mu_0\Delta H_0)\sqrt{1 + \left(\frac{\gamma\mu_0 M_s}{2f_{\text{res}}}\right)^2} \tag{2.38}$$

The in-plane frequency linewidth is very large at low resonant frequencies, and then decreases until hitting a minimum but does not imply enhanced damping[19] [20].

Using frequency swept FMR method, $\Delta H, H_{\text{eff}}, H_{\text{res}}$ in fitting function for χ'' are replaced as $\Delta f, f, f_{\text{res}}$ and χ'' becomes

$$\chi'' = A_{\text{sym}}\frac{\Delta f^2}{\Delta f^2 + (f - f_{\text{res}})^2} - B_{\text{asym}}\frac{\Delta f(f - f_{\text{res}})}{\Delta f^2 + (f - f_{\text{res}})^2}. \tag{2.39}$$

The fit follows the FMR line as seen in fig, from these fittings we could extract the resonance field H_{res} or f_{res}, the half-width at half maximum ΔH or Δf and the

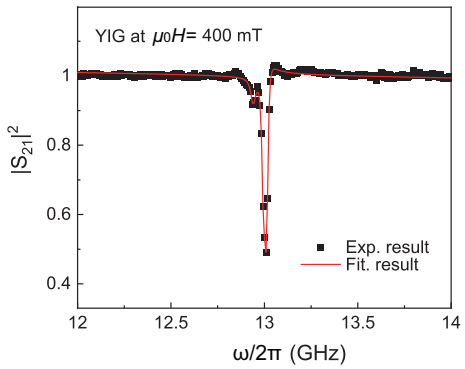

Figure 2.11 Derivative of the absorption at resonance in a YIG deposited on GGG and the integrated signal measured at a field of $\mu_0 H = 400$ mT. The fit was obtained using equation (2.39) the fitting parameters are $\Delta f = 0.032 \pm 0.002$ GHz and $f_{\text{res}} = 13 \pm 0.1$ GHz

amplitude of FMR induced absorption power. Note that in this analysis, we also consider other absorptions from spin waves (around 12.8 GHz) so that this data is fitted by two symmetric and asymmetric Lorentzian.

2.3 FDTD method

The CST Studio Suit is a commercially available software package, which makes use of finite integration techniques (FIT) to carry out electromagnetic simulations. Unlike most numerical methods, FIT discretises the integral form of Maxwell's equations rather than the differential ones. To solve these numerically one must define a finite calculation domain. To that end, a mesh system is implemented to divide the domain into many grid cells. The primary mesh can be visualised in CST using mesh view, however, internally a second or dual mesh is set up orthogonal to the first one. The spatial discretisation of Maxwell's equations is performed on these two orthogonal grid systems. Maxwell' s equations are formulated for each of the cell facets separately. To describe the FIT technique consider the following of Maxwell's equations.

$$\int \boldsymbol{E} \cdot d\boldsymbol{S} = -\frac{\partial}{\partial t} \int \int \boldsymbol{B} \cdot d\boldsymbol{A} \tag{2.40}$$

When considering a mesh cell Faraday' s law permits the closed integral $\int \boldsymbol{E} \cdot \boldsymbol{dS}$ to be rewritten as the sum of four grid voltages $(e_i + e_j - e_k - e_l)$. Also the magnetic flux on the enclosed cell facet (b_n) is equivalent to $\int \int \boldsymbol{B} \cdot d\boldsymbol{A}$. Thus resulting in Maxwell's equations

$$e_i + e_j - e_k - e_l = -\frac{\partial}{\partial t} b_n \tag{2.41}$$

Repeating this for all the cell facets results in the following matrix formulation, which can also be expressed using operator notation.

Applying a similar scheme to Ampere's law on the dual grid, which requires the definition of the dual discrete curl operator $\tilde{C}$, and discretising the remaining divergence equations results in the complete discretised set of Maxwell' s equations. The

material relations may then be approximated over the grid edges and cell areas, respectively. A noteworthy point of the FIT technique is that the properties of the continuous gradient, curl and divergence operators are maintained in grid space. In addition to orthogonal hexahedral grids, FIT can also be applied to more general mesh types such as topologically irregular and tetrahedral grids.

$$\begin{pmatrix} \cdot & \cdot & \cdot & \cdot & \cdot & \cdot & \cdot \\ 1 & \cdot & 1 & \cdot & -1 & \cdot & -1 \\ \cdot & \cdot & \cdot & \cdot & \cdot & \cdot & \cdot \end{pmatrix} \begin{pmatrix} e_i \\ \cdot \\ e_j \\ \cdot \\ e_k \\ \cdot \\ e_l \end{pmatrix} = -\frac{\partial}{\partial t} \begin{pmatrix} \cdot \\ b_n \\ \cdot \end{pmatrix} \tag{2.42}$$

$$\boldsymbol{C}_e = -\frac{\partial}{\partial t}\boldsymbol{b} \tag{2.43}$$

CST Microwave Studio has three basic solvers from which to choose; the Transient, Frequency Domain and Eigenmode solvers. The correct choice of solver appropriate to the problem type can be of critical importance inaccurate and efficient simulations, as such, a brief overview of the more relevant solvers is considered here. The work of this thesis made frequent use of the transient and frequency domain solvers. The transient solver allows for the simulation of a structure's behaviour over a wide frequency band in a single computation. It is available using only a hexagonal mesh type and is based on the discretised set of Maxwell's Grid equations where central differences are substituted for the time derivatives. The FDTD (Finite Difference Time Domain) method (FDTD) is one of the numerical electromagnetic field analysis methods. It is one of the most widely used analysis methods in the world today. The followings are the basic concepts described in the Yee algorithm [13]. Maxwell's equations using differential form are as follows

$$\nabla \times \boldsymbol{E}(\boldsymbol{r},t) = -\frac{\partial \boldsymbol{B}(\boldsymbol{r},t)}{\partial t} \tag{2.44}$$

$$\nabla \times \boldsymbol{H}(\boldsymbol{r},t) = -\frac{\partial \boldsymbol{D}(\boldsymbol{r},t)}{\partial t} + \boldsymbol{J}(\boldsymbol{r},t) \tag{2.45}$$

$$\nabla \cdot \boldsymbol{D}(\boldsymbol{r},t) = \rho(\boldsymbol{r},t) \tag{2.46}$$

$$\nabla \cdot \boldsymbol{B}(\boldsymbol{r},t) = 0 \tag{2.47}$$

where the electric field $\boldsymbol{E}$ [V/m], the magnetic field $\boldsymbol{H}$ [A/m], and the electric flux density $\boldsymbol{D}$ [C/m^2], the magnetic flux density $\boldsymbol{B}$ [T], ρ is the charge density, and $\boldsymbol{J}$ is the current density. Using the relationship $\boldsymbol{B} = \mu\boldsymbol{H}, \boldsymbol{D} = \epsilon\boldsymbol{E}, \boldsymbol{J} = \sigma\boldsymbol{E}$ (where σ is the electrical conductivity),

$$\frac{\partial \boldsymbol{E}}{\partial t} = -\frac{\sigma}{\epsilon}\boldsymbol{E} + \frac{1}{\epsilon}\nabla \times \boldsymbol{H}, \tag{2.48}$$

$$\frac{\partial \boldsymbol{H}}{\partial t} = -\frac{1}{\mu}\nabla \times \boldsymbol{E}. \tag{2.49}$$

In the FDTD method, the derivative of the function $F(x)$, using the central difference

$$\frac{\partial F}{\partial x} \simeq \frac{F(x+\frac{\Delta x}{2},y,z,t)-F(x-\frac{\Delta x}{2},y,z,t)}{\Delta x} \tag{2.50}$$

$$\frac{\partial F}{\partial t} \simeq \frac{F(x,y,z,t+\frac{\Delta t}{2})-F(x,y,z,t-\frac{\Delta x}{t})}{\Delta t}. \tag{2.51}$$

Also, the points (x,y,z,t) are

$$(x,y,z,t) = (i\Delta x, j\Delta y, k\Delta z, n\Delta t) \tag{2.52}$$

We define F

$$F(x,y,z,t) = F^n(i,j,k) \tag{2.53}$$

where n is simply a subscript.

To use the central difference, $\boldsymbol{E}$ and $\boldsymbol{H}$ are placed alternately on the time axis (Fig. 2.12(a)). $\boldsymbol{E}^n$ is calculated from $\boldsymbol{E}^{n-1}$ and $\boldsymbol{H}^{n-1/2}$, and $\boldsymbol{H}^{n+1/2}$ is calculated from $\boldsymbol{H}^{n-1/2}$ and $\boldsymbol{E}^n$, respectively. Specifically, we calculate

$$\boldsymbol{E}^n = \frac{1-\frac{\sigma\Delta t}{2\epsilon}}{1+\frac{\sigma\Delta t}{2\epsilon}}\boldsymbol{E}^{n-1} + \frac{\Delta t/\epsilon}{1+\frac{\sigma\Delta t}{2\epsilon}}\nabla\times\boldsymbol{H}^{n-1/2} \tag{2.54}$$

$$\simeq -\boldsymbol{E}^{n-1} + \frac{2}{\sigma}\nabla\times\boldsymbol{H}^{n-1/2} \tag{2.55}$$

$$\boldsymbol{H}^n = \boldsymbol{H}^{n-1/2} - \frac{\Delta t}{\mu}\nabla\times\boldsymbol{E}^n \tag{2.56}$$

The calculation is then conducted through consideration of electric voltages and magnetic fluxes. Both sets of unknowns are located alternately in time, and the approach is implemented as in the leap-frog scheme outlined in figure 2.12(a).

Fig. 2.12(b) shows a three-dimensional FDTD unit cell (Yee lattice). As shown here, each axis direction. In the FDTD method, the TE and TM modes are calculated discretely using the above equation. Defined as an electromagnetic wave with the following components

- TE : $E_x, E_y, H_z (E_z = 0)$
- TM : $E_z, H_x, H_y (H_z = 0)$
- TEM : $E_y, H_x (E_z = H_z = 0)$

2.4 Basic concepts of microwave resonators

Resonance means that the cavity stores the microwave energy; therefore, at the resonance frequency of the cavity, no microwaves will be reflected back, but will remain inside the cavity.

A cavity is characterized by their Q or quality factor, which indicates how efficiency the cavity stores microwave energy. it is defined as:

$$Q = \frac{\omega(\text{average energy stored in the resonator})}{\text{energy dissipated per second}} \tag{2.57}$$

where ω is the frequency. Therefore the quality factor is a measure of the circuit's losses. We can measure the Q factors easily because there is another way of expressing

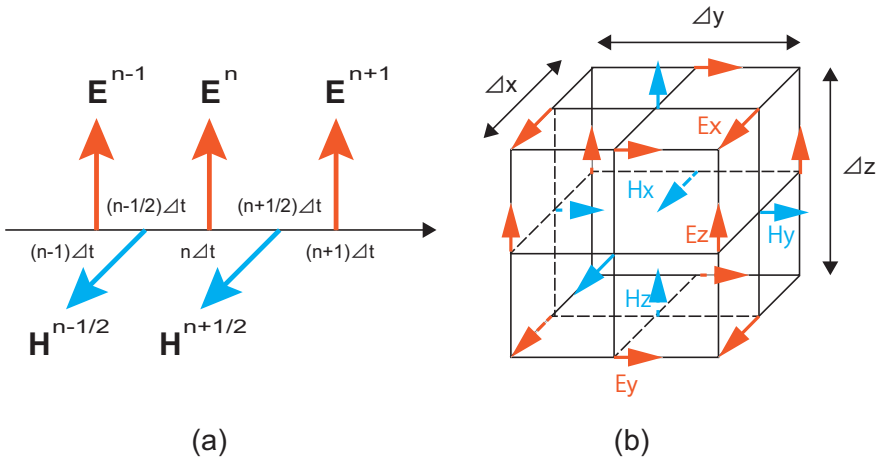

Figure 2.12 Yee's algorithm. (a) $\boldsymbol{E}$ and $\boldsymbol{H}$ are calculated one after the other every $\Delta t/2$. (b) : Yee latice.

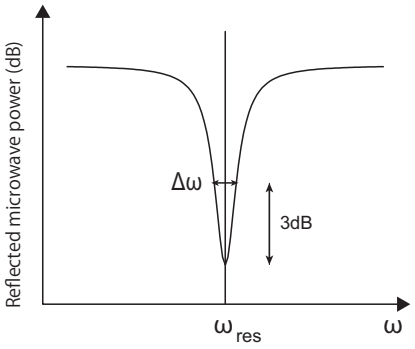

Figure 2.13 Reflected microwave power from a resonator

Q:

$$Q = \frac{\omega_c}{\Delta\omega_c} = \frac{\omega_c}{2\kappa_c} \tag{2.58}$$

with the cavity relaxation rate (HWHM: half width half maximum linewidth) $\kappa_c = 2\Delta\omega$.

Typically, for magnetic resonance spectroscopy, the resonator-feed line coupling is adjusted so that the characteristic impedance of the resonator equals the characteristic impedance of the feed line (50 Ω). This so-called critical coupling leads to optimal power transfer from and to the cavity and hence maximum sensitivity to the magnetic resonance signal. κ_c can be controlled by the external coupling between the resonator and feed-line. In this section, we take a different approach and keep the resonator critically coupled to the feed line but vary magnon-photon coupling rate by tuning the angle between the external static field and microwave, or the damping rate of the sample using nonlinear magnetic phenomena.

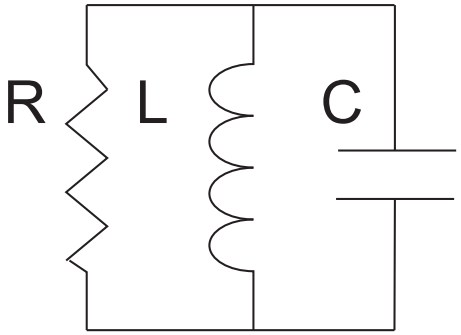

Figure 2.14 Lumped element model of a microstrip resonant circuit. In the vicinity of the resonant frequency, the resonator is modelled as a resistor R, an inductor L and a capacitor C.

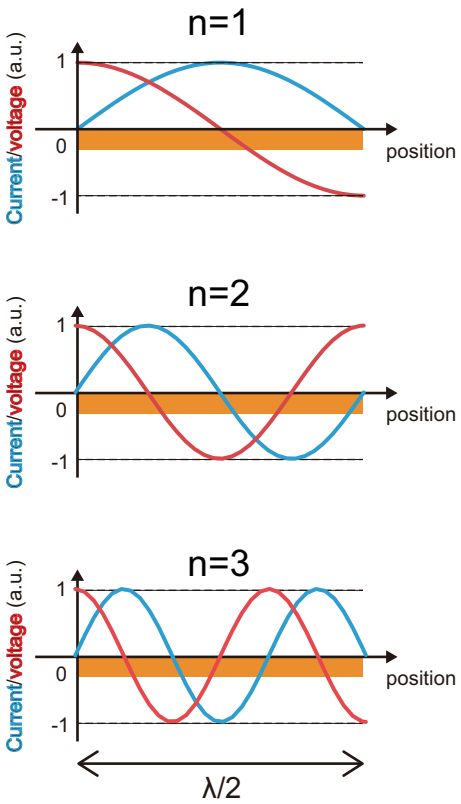

Figure 2.15 Current and voltage distribution in an open circuite transmission line for each mode ($n = 1 \sim 3$). Since the length of the resonator is equal to the half of the wavelength of its ground mode, it is called a $\lambda/2$-resonator.

2.4.1 Lumped element model

There are many methods to describe the behaviour of microstrip resonant circuits[14, 15, 16]. Here we apply the lumped element RLC model which describes the behaviour of a microwofave resonator at a resonant frequency. Transmission lines discussed in the previous chapter have the important property that voltage and

current vary in magnitude and phase over their length. Such a transmission line acts as a resonator whose length is equal to the half of the wavelength of its ground mode. Therefore it is called a $\lambda/2$ resonator.

It is a convenient to model a $\lambda/2$ resonator in the vicinity of the resonant frequency as a parallel connection of a resistor R, an inductor L and a capacitor C as presented in Fig. 2.14. The description of this so-called lumped element model of a transmission line resonant circuit. The input impedance Z_{in} of this circuit is given by

$$Z_{\text{in}} = \left(\frac{1}{R} + \frac{1}{i\omega L} + i\omega C \right)^{-1}, \tag{2.59}$$

where ω is the frequency and i is the imaginary unit. The complex input power P_{in} at the resonator's input is given by

$$P_{\text{in}} = \frac{1}{2}|V|^2 \left(\frac{1}{R} + \frac{1}{i\omega L} + i\omega C \right)^{-1}, \tag{2.60}$$

where V is voltage. The $1/R$-term in this equation represents the energy E_{loss} dissipated in the resistor. The complex terms represent the magnetic energy W_m stored in the inductor and the electric energy W_e stored in the capacitor, respectively. Resonance occurs when the resonator is able to convert the magnetic energy to the electric energy. To fulfill this condition $W_e = W_m$ must hold. Therefore the unloaded resonant frequency ω_0 is given by

$$\omega_0 = \frac{1}{\sqrt{LC}} \tag{2.61}$$

This is the frequency of the fundamental mode of the resonator. The resonant frequency of the n^{th} mode of the resonator is given by

$$\omega_n = n\omega_0 = \frac{1}{\sqrt{L_n C}} \tag{2.62}$$

where

$$L_n = Ln^2 \tag{2.63}$$

and $n \geq 1$ is an integer number. Then the internal quality factor of the resonant circuit is given according to Equation 2.4.16 by

$$Q_{\text{int}} = \omega_n \frac{2E_m}{E_{\text{loss}}} = \frac{R}{\omega_n L_n} = \omega_n RC \tag{2.64}$$

2.4.2 Capacitance and Induvtive coupled resonator

If we want to characterize a resonant circuit we have to couple it to external circuitry to feed the power. In my first experiment, this is done via gap coupling. The circuit consists of two building blocks, the $\lambda/2$ resonator and the feed lines. Both of them are transmission lines of the microstrip type. Feed lines serve solely to couple external circuits to the resonator. Important element of the circuit is the gap between the feed

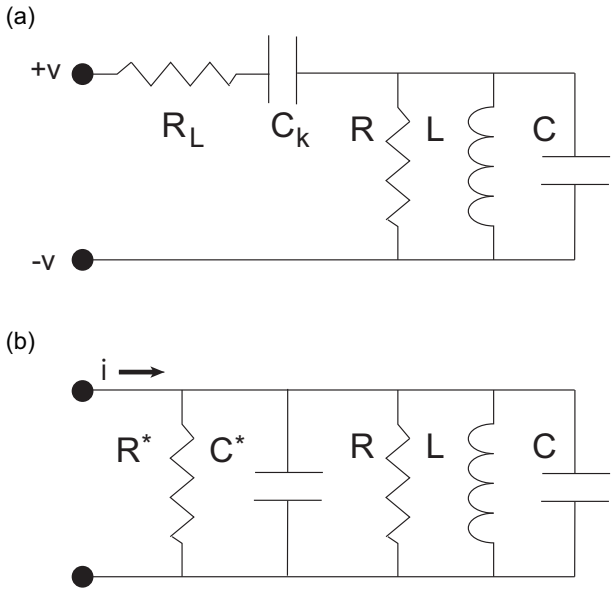

Figure 2.16 Lumped element model of a coupled resonant circuit. (a) The gap is modeled as a coupling capacitance C_k. The input and output circuitry are modeled by a load resistor R_L. (b) The elements R^* and C^* are Norton equivalents of C_k and R_L [17].

lines and the resonator. The effect of the gap is represented by a coupling capacitance C_k and a resistor R_L which is replaced as the feed line.

For further analysis the series connection of the coupling capacitance C_k and the resistor R_L is replaced by its Norton equivalent circuit. The Norton equivalent circuit [17] consists of a resistor R^* and a capacitor C^* with

$$R^* = \frac{1 + \omega_n^2 C_k^2 R_L^2}{\omega_n^2 C_k^2 R_L^2} \tag{2.65}$$

$$C^* = \frac{C_k}{1 + \omega_n^2 C_k^2 R_L^2}. \tag{2.66}$$

Then the loaded the quality factor Q_L for 1-port configuration is reduced due to the resistive loading, yielding

$$Q_L = \omega_n^* \frac{C + C^*}{1/R + 1/R^*} \tag{2.67}$$

with the loaded resonant frequency ω_n^*. The latter takes into account the effect of capacitive loading and is given by

$$\omega_n^* = \frac{1}{\sqrt{L_n(C + C^*)}} \tag{2.68}$$

The external quality factor Q_{ext} is given by

$$Q_{\text{ext}} = \frac{\omega_n R^* C}{2}. \tag{2.69}$$

In concusion, the internal quality factor Q_{int} represents the losses in the resonator and the external quality factor Q_{int} is influenced by the losses in the gap and in

the feedlines. The loaded quality factor Q_L is a parallel combination of the internal quality factor Q_{int} and the external quality factor Q_{ext},

$$\frac{1}{Q_L} = \frac{1}{Q_{\text{int}}} + \frac{1}{Q_{\text{ext}}}. \tag{2.70}$$

If two resonators are placed in proximity to one another such that there also be coupling between them via inductive coupling and it becomes possible for the resonators to exchange energy. The coupling coefficient is the ratio of the open-circuit actual voltage ratio to the ratio that would obtain if all the flux coupled from one circuit to the other. From the two simultaneous equations expressed in the two-port matrix the open-circuit voltage ratio is found to be:

$$\frac{V_2}{V_1}(\text{open circuit}) = \frac{\text{M}}{\text{L}_1} \tag{2.71}$$

while the ratio if all the flux is coupled is the ratio of the turns, hence the ratio of the square root of the inductances

$$\frac{V_2}{V_1}(\text{max coupled}) = \sqrt{\frac{\text{L}_2}{\text{L}_1}} \tag{2.72}$$

thus,

$$M = k\sqrt{L_1 L_2} \tag{2.73}$$

where $k(0 \leq k < 1)$ is the coupling coefficient, $L_n(n = 1, 2)$ is the inductance of each coil. he coupling coefficient is a convenient way to specify the relationship between a certain orientation of inductors with arbitrary inductance.

2.4.3 Losses in the microstrip resonator

Uncoupled resonator

There are three major loss mechanisms in the microstrip resonator. Their origins are the resistive, dielectric, and radiative loss. We first consider the resistive mechanism. We use alminum and copper for the conducting layer. The model postulates the existence of the type of charge carriers, the normal electrons. The normal electrons as charge carriers contribute to the current. Because the impedance $Z_n = i\omega L_n$ behaves like a normal circuit, the resistance of our circuit appeared as Joul heating. Also, if we apply an alternating current with frequency $\omega \neq 0$, AC current will flow through the normal channel and we have to take the resistance into consideration.

Next one is the dielectric losses. The dissipation due to the unsaturated two-level system at low temperature and low power is a relatively large magnitude and can dominate other effects [18]. All of my measurements is under the room tempearature so ralative effect can be ignored.

Finally, we consider the radiation losses. The size of our circuit is of the order of magnitude of the wavelength of the applied signals. Therefore the resonator will behave as an antenna radiating some of its energy into the environment [19].

To summarize the effect of the above described phenomena, we introduce attenuation constants α_c for the resistive losses in the conductor, α_d for the dielectric losses and α_r for the radiation losses. The total attenuation α of the microstrip line is given by

$$\alpha = \alpha_c + \alpha_d + \alpha_r \tag{2.74}$$

The internal quality factor of the resonator takes all the described loss mechanisms into consideration is given by [20]

$$Q_{\text{int}} = \frac{\pi}{2\alpha l} \tag{2.75}$$

where l is the length of the resonator.

Coupled resonator

Let us now consider a resonator that is gap-coupled to the feed lines. Due to this coupling to the environment energy is partially transmitted from the resonator into the feed lines [21]. These losses are represented by the external quality factor Q_{ext} which is determined by the coupling capacitance. Depending on the value of the coupling capacitance the resonators are divided into two classes [22]. If the coupling capacitance is small, then the resonator is called undercoupled. In the extreme case of an uncoupled resonator ($C = 0$) the loaded quality factor Q_L is governed by the intrinsic losses in the resonator. For the uncoupled resonator it is possible to investigate the internal quality factor Q_{int} [29]. If the coupling capacitance is large, then the resonator is called overcoupled.

Chapter 3

Spin current coherence peak in superconductor/magnet junctions

We injected and detected a spin current in the superconductor NbN/ferrimagnet $Y_3Fe_5O_{12}$(YIG) combined structure using the spin Seebeck effect (SSE). In the normal state, the SSE voltage was observed and the spin injection was successfully performed with high efficiency. In the superconducting state under zero resistivity, the signal disappeared. On the other hand, around the superconducting transition temperature (T_c), the SSE voltage showed the anormalous enhancement in the finite resistivity region. From control experiments, we confirmed that the enhancement is not due to the thermoelectric effect of the superconductor but to the spin current. The theoretical approach based on the linear response theory revealed that the enhancement is due to the coherence effect reflecting the density of states of the quasiparticles scattered at the NbN/YIG interface.

3.1 Coherence effect in superconductivity

The coherence effect, in which an external field as a perturbation is applied to a superconductor, shows a peculiar response reflecting the interference of quasi-particle amplitudes, and provides strong evidence for the validity of the BCS theory in that it is used to explain the experimental results. In the following, we provide a standard explanation of the coherence effect by using the Bogoliubov transformation introduced to explain BCS theory. In this section, we will also proceed with the discussion under the assumption of a superconductor with s wave symmetry.

We use the following Hamiltonian as an external field (electric, magnetic, elastic, etc.) that we apply to the superconductor:

$$\mathcal{H}_{\rm ext} = \sum_{\boldsymbol{k},\boldsymbol{k}',\sigma,\sigma'} A_{\boldsymbol{k}\sigma,\boldsymbol{k}'\sigma'} c^{\dagger}_{\boldsymbol{k}\sigma} c_{\boldsymbol{k}'\sigma'}, \tag{3.1}$$

where $A_{\boldsymbol{k}\sigma,\boldsymbol{k}'\sigma'}$ is the transition matrix element of the field and the electrons in the superconductor in state $(\boldsymbol{k}',\sigma')$ to the $(\boldsymbol{k},\sigma)$. The coefficients can be classified using the new coefficient $\theta_{\sigma\sigma'}$ by their behavior under the time-reversal, i.e., when $\boldsymbol{k}\to-\boldsymbol{k}, \sigma\to-\sigma$.

$$A_{\boldsymbol{k}\sigma,\boldsymbol{k}'\sigma'} = +\theta_{\sigma\sigma'} A_{-\boldsymbol{k}'-\sigma',-\boldsymbol{k}-\sigma} \text{ (I)} \tag{3.2}$$

$$A_{\boldsymbol{k}\sigma,\boldsymbol{k}'\sigma'} = -\theta_{\sigma\sigma'} A_{-\boldsymbol{k}'-\sigma',-\boldsymbol{k}-\sigma} \text{ (II)} \tag{3.3}$$

Case I corresponds to an electric or elastic field with even under time reversal, and case II corresponds to a magnetic field with odd under time reversal. In the following, we focus on ultrasonic absorption and nuclear magnetic relaxation, the former belonging to the $\sigma = \sigma'$ case I and the latter to the $\sigma = -\sigma'$ case II. In the previous section, we noted that electrons in a superconductor are characterized by quasi-particles, and we can understand the essence of the coherence effect by rewriting the external field (3.1). First, we deal with the spin-free version of (3.1) under the Bogoliubov transformation with the formula

$$c_{\boldsymbol{k}\uparrow} = u_{\boldsymbol{k}}\alpha_{\boldsymbol{k}0} + v_{\boldsymbol{k}}\alpha^{\dagger}_{-\boldsymbol{k}1}, \tag{3.4}$$

$$c^{\dagger}_{-\boldsymbol{k}\downarrow} = -v_{\boldsymbol{k}}\alpha_{\boldsymbol{k}0} + u_{\boldsymbol{k}}\alpha^{\dagger}_{-\boldsymbol{k}1}, \tag{3.5}$$

$$u^2_{\boldsymbol{k}} + v^2_{\boldsymbol{k}} = 1. \tag{3.6}$$

We can rewrite

$$\begin{aligned} c^{\dagger}_{\boldsymbol{k}\uparrow}c_{\boldsymbol{k}'\uparrow} &= u_{\boldsymbol{k}}u_{\boldsymbol{k}'}\alpha^{\dagger}_{\boldsymbol{k}0}\alpha_{\boldsymbol{k}'0} - v_{\boldsymbol{k}}v_{\boldsymbol{k}'}\alpha^{\dagger}_{-\boldsymbol{k}'1}\alpha_{-\boldsymbol{k}1} \\ &\quad + u_{\boldsymbol{k}}v_{\boldsymbol{k}'}\alpha^{\dagger}_{\boldsymbol{k}0}\alpha^{\dagger}_{-\boldsymbol{k}'1} + v_{\boldsymbol{k}}u_{\boldsymbol{k}'}\alpha_{-\boldsymbol{k}1}\alpha_{-\boldsymbol{k}'0} \end{aligned} \tag{3.7}$$

$$\begin{aligned} c^{\dagger}_{-\boldsymbol{k}'\downarrow}c_{-\boldsymbol{k}\downarrow} &= -v_{\boldsymbol{k}}v_{\boldsymbol{k}'}\alpha^{\dagger}_{\boldsymbol{k}0}\alpha_{\boldsymbol{k}'0} + u_{\boldsymbol{k}}u_{\boldsymbol{k}'}\alpha^{\dagger}_{-\boldsymbol{k}'1}\alpha_{-\boldsymbol{k}1} \\ &\quad + v_{\boldsymbol{k}}u_{\boldsymbol{k}'}\alpha^{\dagger}_{\boldsymbol{k}0}\alpha^{\dagger}_{-\boldsymbol{k}'1} + u_{\boldsymbol{k}}v_{\boldsymbol{k}'}\alpha_{-\boldsymbol{k}1}\alpha_{-\boldsymbol{k}'0} \end{aligned} \tag{3.8}$$

Time-reversal symmetry of $A_{\boldsymbol{k}\uparrow,\boldsymbol{k}'\uparrow}c^{\dagger}_{\boldsymbol{k}\uparrow}c_{\boldsymbol{k}'\uparrow}$ and $A_{-\boldsymbol{k}'\downarrow,-\boldsymbol{k}\downarrow}c^{\dagger}_{-\boldsymbol{k}'\downarrow}c_{-\boldsymbol{k}\downarrow}$ affects their interference. Therefore, when calculating the transition probability due to an external perturbation, we need to add the interfering amplitudes first. For $\sigma = \sigma'$ (3.1) reads

$$\mathcal{H}_{\rm ext} = \sum_{\boldsymbol{k},\boldsymbol{k}'} (A_{\boldsymbol{k}\uparrow,\boldsymbol{k}'\uparrow}c^{\dagger}_{\boldsymbol{k}\uparrow}c_{\boldsymbol{k}'\uparrow} + A_{-\boldsymbol{k}'\downarrow,-\boldsymbol{k}\downarrow}c^{\dagger}_{-\boldsymbol{k}'\downarrow}c_{-\boldsymbol{k}\downarrow}) \tag{3.9}$$

$$= \sum_{\boldsymbol{k},\boldsymbol{k}'} A_{\boldsymbol{k}\uparrow,\boldsymbol{k}'\uparrow}[(u_{\boldsymbol{k}}u_{\boldsymbol{k}'} \mp v_{\boldsymbol{k}}v_{\boldsymbol{k}'})(\alpha^{\dagger}_{\boldsymbol{k}0}\alpha_{\boldsymbol{k}'0} \pm \alpha^{\dagger}_{-\boldsymbol{k}'1}\alpha_{-\boldsymbol{k}1}) + (u_{\boldsymbol{k}}v_{\boldsymbol{k}'} \pm v_{\boldsymbol{k}}u_{\boldsymbol{k}'})(\alpha^{\dagger}_{\boldsymbol{k}0}\alpha^{\dagger}_{-\boldsymbol{k}'1} \pm \alpha_{-\boldsymbol{k}1}\alpha_{-\boldsymbol{k}'0})] \tag{3.10}$$

When $\sigma = -\sigma'$,

$$\mathcal{H}_{\rm ext} = \sum_{\boldsymbol{k},\boldsymbol{k}'} (A_{\boldsymbol{k}\uparrow,\boldsymbol{k}'\downarrow}c^{\dagger}_{\boldsymbol{k}\uparrow}c_{\boldsymbol{k}'\downarrow} + A_{-\boldsymbol{k}'\uparrow,-\boldsymbol{k}\downarrow}c^{\dagger}_{-\boldsymbol{k}'\uparrow}c_{-\boldsymbol{k}\downarrow}) \tag{3.11}$$

$$= \sum_{\boldsymbol{k},\boldsymbol{k}'} A_{\boldsymbol{k}\uparrow,\boldsymbol{k}'\downarrow}[(u_{\boldsymbol{k}}u_{\boldsymbol{k}'} \mp v_{\boldsymbol{k}}v_{\boldsymbol{k}'})(\alpha^{\dagger}_{\boldsymbol{k}0}\alpha_{\boldsymbol{k}'1} \pm \alpha^{\dagger}_{-\boldsymbol{k}'0}\alpha_{-\boldsymbol{k}1}) + (u_{\boldsymbol{k}}v_{\boldsymbol{k}'} \pm v_{\boldsymbol{k}}u_{\boldsymbol{k}'})(\alpha^{\dagger}_{\boldsymbol{k}0}\alpha^{\dagger}_{-\boldsymbol{k}'0} \mp \alpha_{-\boldsymbol{k}1}\alpha_{-\boldsymbol{k}'1})] \tag{3.12}$$

Comparing Eqs. (3.10) and (3.12) contain two contributions: the first items, which includes the $\alpha^{\dagger}\alpha$, and the second items, which includes $\alpha^{\dagger}\alpha^{\dagger}(\alpha\alpha)$. The former corresponds to the excitation process by which quasiparticles are scattered, while the latter does not conserve the quasi-particle number. The latter process implies on one hand the destruction of the Cooper pairs and a creation of two that requires more than $2|\Delta|$ of excitation energy. In the following we discuss the transition probabilities due to these external fields in which the square of the coefficients before $\alpha^{\dagger}\alpha$ and $\alpha^{\dagger}\alpha^{\dagger}(\alpha\alpha)$ is important.

For the quasi-particle excitation process, the following factors make a particularly important contribution to the transition probability:

$$(u_{\boldsymbol{k}}u_{\boldsymbol{k}'} \mp v_{\boldsymbol{k}}v_{\boldsymbol{k}'})^2 = \frac{1}{2}(1 + \frac{\xi_{\boldsymbol{k}}\xi_{\boldsymbol{k}'}}{E_{\boldsymbol{k}}E_{\boldsymbol{k}'}} \mp \frac{\Delta^2}{E_{\boldsymbol{k}}E_{\boldsymbol{k}'}}) \tag{3.13}$$

The upper sign corresponds to Case I and the lower sign to Case II. (3.13) is called coherence factors and affect the transition probability (as a function of temperature).

In this section, both the case without spin flipping (3.10) and with spin flipping (3.12) are calculated. In order to see the influence of the coherence factor on the transition probability, we calculate the ultrasonic absorption and nuclear magnetic relaxation rates below. Both the frequencies of ultrasonic absorption and relaxation rates are sufficiently small compared to the absolute value of the superconducting gap $|\Delta|$, and no quasi-particle pairing or annihilation process can occur. Therefore, we only need to consider (3.13) as a coherence factor. The only difference between ultrasonic absorption and nuclear magnetic relaxation is the sign within the coherence factor. Therefore, if we write the coherence factor as $C_{\boldsymbol{k},\boldsymbol{k}'}$ in general, the transition probability W_s for both phenomena can be written by Fermi's golden rule as follows.

$$W_s \propto |A|^2 \sum_{\boldsymbol{k},\boldsymbol{k}'} C_{\boldsymbol{k},\boldsymbol{k}'}[f(E_{\boldsymbol{k}'}) - f(E_{\boldsymbol{k}})]\delta(E_{\boldsymbol{k}'} + \omega - E_{\boldsymbol{k}}) \tag{3.14}$$

Here the wavenumber and spin dependence of the external field coefficient is neglected and A is set to A, and the energy of the outer field multiplied is set to ω. Substituting the specific form of the coherence factor (3.13) into the equation (3.14) and organizing the equation after the variable transformation, we get the following.

$$\begin{aligned}
W_s \propto & |A|^2 N(0)^2 \int d\xi_{\boldsymbol{k}} d\xi_{\boldsymbol{k}'} (1 \mp \frac{\Delta^2}{E_{\boldsymbol{k}} E_{\boldsymbol{k}'}})[f(E_{\boldsymbol{k}'} - E_{\boldsymbol{k}})]\delta(E_{\boldsymbol{k}'} + \omega - E_{\boldsymbol{k}}) \qquad (3.15)\\
= & |A|^2 N(0)^2 \int_\Delta^\infty dE \int_\Delta^\infty dE' \frac{E}{\sqrt{E^2 - \Delta^2}} \frac{E'}{\sqrt{E'^2 - \Delta^2}} \\
& \times (1 \mp \frac{\Delta^2}{EE'})[f(E') - f(E)]\delta(E' + \omega - E) \\
= & |A|^2 N(0)^2 \int_\Delta^\infty dE' \frac{E' + \omega}{\sqrt{(E' + \omega)^2 - \Delta^2}} \frac{E'}{\sqrt{E^2 - \Delta^2}} \\
& \times (1 \mp \frac{\Delta^2}{EE'})[f(E') - f(E' + \omega)] \\
= & |A|^2 N(0)^2 \int_\Delta^\infty dE' \frac{[E'(E' + \omega) \mp \Delta^2][f(E') - f(E' + \omega)]}{\sqrt{E'^2 - \Delta^2}\sqrt{(E' + \omega)^2 - \Delta^2}} \qquad (3.16)
\end{aligned}$$

Note that the term is excluded in the coherence factor in the Eq. (3.15), which is derived from the odd function of the $\xi_{\boldsymbol{k}}\xi_{\boldsymbol{k}'}/E_{\boldsymbol{k}}E_{\boldsymbol{k}'}$ term. This is due to the fact that this term is an odd function of $\xi_{\boldsymbol{k}}, \xi_{\boldsymbol{k}'}$. We also put $N(0)$ for the density of states in the normal-conducting state. Using the Eq. (3.16), we obtain the transition probabilities in the cases of ultrasonic absorption and nuclear magnetic relaxation, respectively. We will use the Eq. (3.16) to find the transition probability for each case of ultrasonic absorption and nuclear magnetic relaxation.

Ultrasound Absorption

Since ultrasonic absorption is a response to an external field (I) that perturbs the density of the system, we can take the sign on the equation (3.16). Then the transition probability is as follows.

$$\begin{aligned}
W_s &\approx -|A|^2 N(0)^2 \int_\Delta^\infty dE' \frac{\partial f(E)'}{\partial E'} \omega \qquad (3.17)\\
&= |A|^2 N(0)^2 f(\Delta)\omega \qquad (3.18)
\end{aligned}$$

Note that the fact that W_n is $\omega \ll |\Delta|$ is used in deriving the first formula. The normal-conductive state transition probability W_n can be given in the formula (3.18) as $W_n = (|A|^2 N(0)^2 \omega)/2$, where W_n is the value of the normal-conductive state. Therefore, the transition probability (ultrasonic absorption rate) can be calculated as follows as a ratio to the normal conducting state value.

$$\frac{W_s}{W_n} = \frac{2}{1 + e^{\beta\Delta}} \tag{3.19}$$

A comparison of the experimental and the BCS theory calculations of the temperature dependence of ultrasonic absorption is shown in Fig. 3.1. Here T_c is the superconducting transition temperature. As can be seen in the figure 3.1, the ultrasonic absorption decreases monotonically below the transition temperature. And this behavior can be understood from the equation (3.18) as follows. Equation (3.18) contains a factor of $E'/\sqrt{E'^2 - \Delta^2}$ which is derived from the density of states $1/\sqrt{E'^2 - \Delta^2}$ of the superconducting state. This factor diverges with $E' = \Delta$, but it is the factor $E'(E'+\omega) - \Delta^2$ derived from the coherence factor that suppresses its divergence. Now, the factor is effectively $E'^2 - \Delta^2$ and is zero at $E' = 0$ because the ω is sufficiently small compared to $|\Delta|$. Thus, at $E' = \Delta$ this factor cancels out the divergence of the denominator and obtains the monotonic decreasing behavior as shown in the figure.

Nuclear magnetic relaxation

Since nuclear magnetic relaxation in superconductor is the response of spin, the transition probability is as follows

$$W_s \approx -|A|^2 N(0)^2 \int_\Delta^\infty dE' \frac{E'(E'+\omega) + \Delta^2}{\sqrt{E'^2 - \Delta^2}\sqrt{(E'+\omega)^2 - \Delta^2}} \frac{\partial f(E')}{\partial E'} \omega \tag{3.20}$$

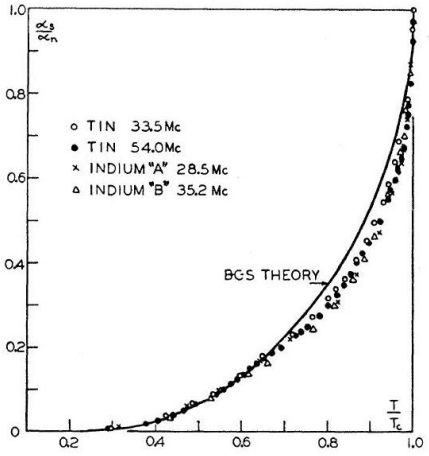

Figure 3.1 The temperature dependence of the ultrasonic absorption rate measured by Morse et al. A comparison of viability and calculations based on BCS theory [Reprinted from R.W. Morse and H.V. Bohm, Phys. Rev. **108**, 1094 (1957).]

Since the transition probability in the normal-conducting state is $W_n = (|A|^2 N(0)^2 \omega)/2$, the transition probability (i.e., nuclear magnetic relaxation rate) is calculated as follows compared to the value in the normal-conducting state.

$$\frac{W_s}{W_n} = 2\int_{\Delta}^{\infty} dE' \frac{E'(E'+\omega)+\Delta^2}{\sqrt{E'^2-\Delta^2}\sqrt{(E'+\omega)^2-\Delta^2}} \frac{\partial f(E')}{\partial E'} \tag{3.21}$$

Again, we use the fact of $\omega \ll \Delta$. The temperature dependence of the nuclear magnetic relaxation rate obtained in this way is shown in Fig. 3.2. It can be seen that the nuclear magnetic relaxation rate R_s has a peak just below the transition temperature. This peak is called the Hebel-Slichter peak after its discoverer. The temperature dependence can be easily understood from the equation (3.16) or the formula (3.21). The same formula(3.21) as before contains a factor $1/\sqrt{E'^2-\Delta^2}$ that originates from the density of states of superconductivity and diverges with $E' = \Delta$. But in this case, unlike the ultrasound case, the factor $(E'(E'+\omega)+\Delta^2)$ derived from the coherence factor is not zero and has a finite value at $E' = \Delta$ due to its internal positive sign. Therefore, the divergence of the density of states cannot be cancelled out and a peak appears as shown in the figure 3.2.

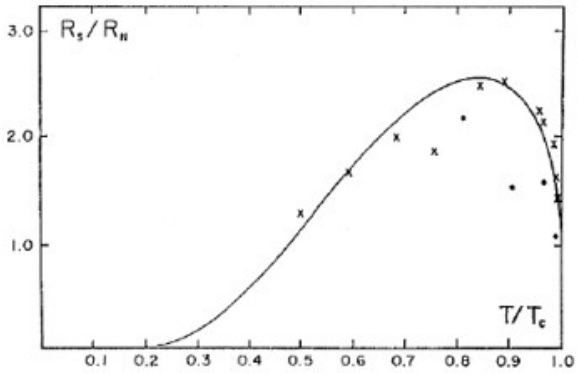

Figure 3.2 Comparison of the temperature dependence of the nuclear magnetic relaxation rate obtained by Hebel and Slichter with calculations based on BCS theory [Reprinted from L. C. Hebel and C. P. Slichter, Phys. Rev. **113**, 1504 (1959).]

The temperature dependence of the transition probability (response function) of a superconductor subjected to an external field of $\omega \ll |\Delta_{\boldsymbol{k}}|$ is determined by the following effective coherence factor.

$$\frac{1}{2}(1 \mp \frac{\Delta_{\boldsymbol{k}}\Delta_{\boldsymbol{k}'}}{E_{\boldsymbol{k}E_{\boldsymbol{k}'}}}) \tag{3.22}$$

In the case of an external field that perturbs the density of the system, such as ultrasonic absorption (I), the transition probability (density response function) does not have a peak and decreases monotonically with temperature because the coherence factor with the negative sign of Eq. (3.22). On the other hand, when an external field is applied to the system that perturbs the system's spin, such as nuclear magnetic

relaxation (II), the transition probability (spin response function) has a peak and then decreases with temperature because the coherence factor with the positive sign of equation (3.22) does not cancel out the divergence of the density of states.

The origin of the Hebel-Slichter peak is a scattering process that reverses the spin of the quasiparticle with respect to the external field. Considering the spin currents in the paramagnetic/ferromagnetic junction system discussed here, the s-d exchange interaction at the interface leads to spin reversal of electrons through the magnon, so we find that the situation is very similar to the nuclear relaxation process.

Therefore, we performed thermal spin injection and voltage measurement detected by the inverse spin Hall effect in superconductor.

3.2 Transport properties

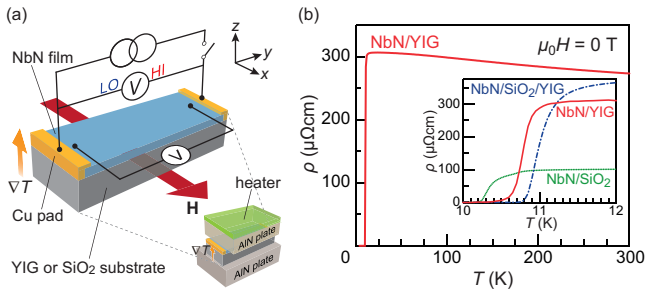

Figure 3.3 (a) A schematic illustration of the longitudinal SSE measurement. Ohmic contacts are made at the Cu pads. The temperature gradient ∇T and magnetic field H are applied in the $+z$ and $\pm x$ directions, respectively, and the thermoelectric voltage is measured in the $+y$ direction. Resistivity (ρ) measurement is done with a four-point probe. (b) Temperature (T) dependence of ρ for NbN/YIG (red color), NbN/SiO_2(100 nm)/YIG (blue color), and NbN/SiO_2 (green color) in zero magnetic field.

The measurement of the SSE was performed using the longitudinal setup with a superconducting magnet [88], where an external magnetic field (H) up to 9 T was applied along the x direction in the film plane [xy-plane in Fig. 3.3(a)]. The sample was sandwiched by two aluminum-nitride plates. The temperature difference ΔT along the z axis was applied using a chip resistance heater [Fig. 3.3(a)] and measured with a couple of type-E thermocouples. The ISHE voltage which arises in the y-direction due to $\nabla T(||z)$ was measured using a nanovoltmeter at each H value. As shown in Fig. 3.3(a), a 30-nm-thick Cu film was deposited at ends of the NbN film, and ohmic contacts were made on the Cu parts for the measurement of ISHE voltage. To compare the ISHE voltage and the transport properties of the NbN layer under a temperature gradient, 4-wire resistance was measured under the same ΔT values. The resistance of the NbN layer was used also as a thermometer to determine the average sample temperature of the NbN layer under ΔT.

Resistivity, ρ, for the NbN/YIG bilayer measured without applying H nor ΔT

is shown as a function of system temperature, T, in Fig. 3.3(b). The magnitude of ρ is about 270 $\mu\Omega$cm at 300 K. ρ increases slightly as T decreases from 300 K, and suddenly drops around 11 K. The occurrence of the zero resistivity state below 10.5 K clearly demonstrates that the NbN layer shows superconductivity below that temperature. The resistivity becomes zero below 10.5 K, signifying superconductivity of the NbN layer. T_c is determined as the temperature where ρ becomes 95 % of the normal state resistivity ρ_n. In the inset to Fig. 3.3(b), the T dependences of ρ for a NbN/SiO_2/YIG trilayer and a NbN/SiO_2 bilayer are also shown, where the thickness of the SiO_2 layer is 100 nm. The NbN films in NbN/SiO_2/YIG and NbN/SiO_2 show similar T_c: 11.7 K and 10.6 K, respectively.

3.3 SSE measurement in normal and superconducting states

In Fig. 3.4, we show the experimental results of the SSE measurements, by plotting $S \equiv V/\Delta T$. Figure 3.4(a) shows the H dependence of S measured at 300 K, which is much higher than $T_c = 11.1$ K. The observed H dependence of S is antisymmetric with respect to the magnetic field. By increasing H from zero, S gradually increases reflecting the magnetization in YIG [inset to Fig. 3.4(a)], but is clearly suppressed by further increasing H ($\mu_0 H > 0.1$ T). This suppression of S is consistent with the typical SSE feature [88]; magnon excitations responsible for SSE are suppressed by strong magnetic fields. The sign of S is consistent with the spin Hall angle of Nb [89]. As T decreases in the normal-state regime far above T_c, the magnitude of S at constant magnetic field ($\mu_0 H = 0.15$ T) shows a maximum around 60 K and then decreases with decreasing T, as shown in the inset of Fig. 3.4(b).

Figure 3.4(c) shows the H dependence of S for the NbN/YIG at 7 K, which is immediately below T_c. The magnitude of S is almost zero in the low H regime, but suddenly increases at around ± 6 T. The onset H corresponds to a superconducting critical field. A similar behavior is observed in the NbN/SiO_2 as shown in Fig. 3.4(c). In the normal state in the vicinity of the transition, large ΔT-induced voltage signals are observed [see Figure 3.4(c)], which are due to a superconducting vortex flow by thermal gradients. This effect is known as the vortex Nernst effect (VNE), where the vortex flow in the direction of decreasing temperature gives rise to a voltage along the Hall direction [91, 92, 93, 94, 95]. When the H direction is reversed, the direction of the magnetic flux of vortices is reversed, and the sign of the voltage due to the VNE is reversed, consistent with the experimental results in Fig. 3.4(c). Note that the sign of the VNE voltage is opposite to that of the spin Seebeck voltage, as shown in Figs. 3.4(a), (b), and (c). ; electric field induced by vortex Nernst effect is written as $\boldsymbol{E} = \mu_0 \boldsymbol{H} \times \boldsymbol{v}_\phi$ where $\boldsymbol{v}_\phi$ is vortex flow velocity which is along $-z$ direction [Fig. 3.3(a)]. With further increasing H in the normal state, the superconducting fluctuation becomes smaller, and the VNE is suppressed.

As T further decreases down to 4 K, which is much lower than T_c, no voltage signal is observed even up to 9 T. At very low temperatures below T_c, the zero-resistivity

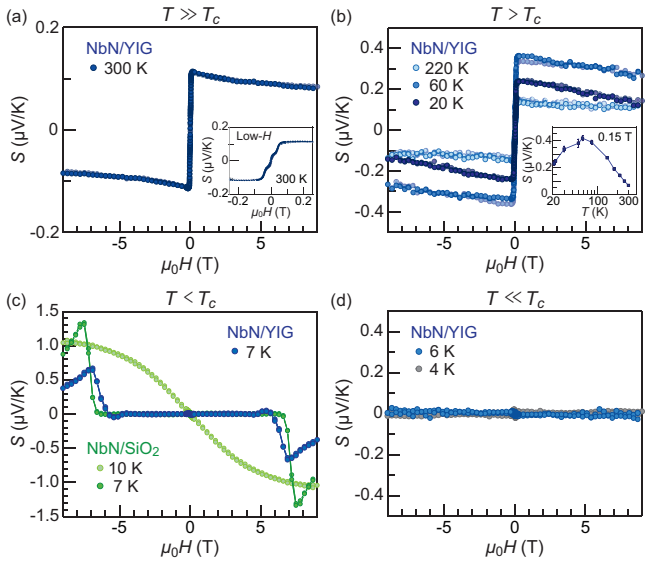

Figure 3.4 H dependence of S for NbN/YIG (a) at $T = 300$ K, (b) at selected temperatures above T_c, (c) at 7 K just below T_c (blue circles), and (d) in the zero-resistivity state below T_c. The H was swept between -9 T and 9 T. The inset to (a) shows a magnified view of $S(H)$ in the low-H range ($|\mu_0 H| \lesssim 0.25$ T) at 300 K. The inset to (b) presents the T dependence of the saturated value of S at $\mu_0 H = 0.15$ T. In (c), H dependence of S for NbN/SiO_2 at 7 K and 10 K is also shown (green and light green circles). All the measurements were done with $\Delta T = 2.0$ K

state persists up to 9 T, which means that vortices are strongly pinned in the NbN layer. Therefore, the voltage due to the VNE disappears in a mixed state at low temperatures [96]. The voltage due to SSE also disappears owing to the shunting effect due to the zero resistivity [97]. The disappearance of the ISHE voltage in the zero-resistivity state of the NbN is in stark contrast to a previous report on the giant ISHE induced by electrical spin injection into a NbN layer [72]. In our case, the voltage contact is ohmic, different from the non-ohmic contact in the previous report [72], and charge neutrality in the superconductor can be achieved by the cancellation of the QP charge currents and supercurrents [98].

3.4 Temperature dependence of SSE around T_c

We found that, surprisingly, in a narrow temperature region 9.3 K< T <10.0 K, the magnitude of S is strongly enhanced [Fig. 3.5(a)]. At the same time, the magnetization M of YIG is almost unchanged in the entire temperature range as shown in Fig. 3.5(c). The enhancement of S immediately below T_c cannot be explained by VNE, but is attributable to ISHE induced by SSE for the following reasons. First, the H dependence of S at 9.5 K almost traces the M curve of YIG, as shown in Figs. 3.5(c) and (d), indicating that the H dependence of S is relevant to the YIG magnetization. Second, the sign of the enhanced S signal is the same as that of the

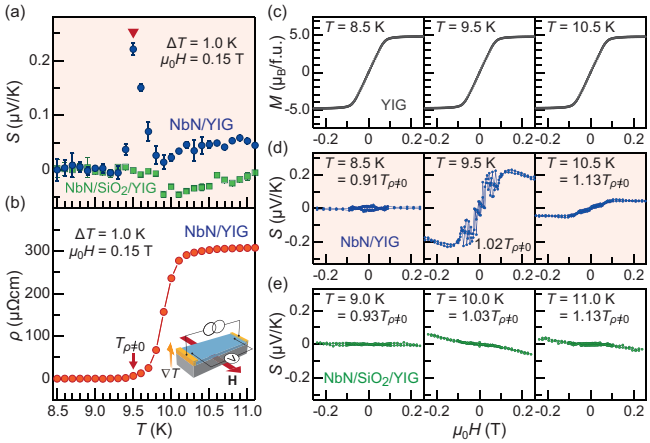

Figure 3.5 (a),(b) T dependence of (a) S and (b) ρ for NbN/YIG near T_c at $\mu_0 H = 0.15$ T with $\Delta T = 1$ K. In (a), T dependence of S for NbN/SiO_2/YIG is also plotted for comparison (green squares). (c) H dependence of magnetization M for the YIG substrate at low temperatures. (d),(e) H dependence of S for (d) NbN/YIG and (e) NbN/SiO_2/YIG in the low-H regime. Here, H was swept between -0.25 T and 0.25 T. For comparison of results between the two samples, the data taken at similar $T/T_{\rho\neq 0}$ values are shown where $T_{\rho\neq 0}$ is the temperature at which ρ begins to increase from the zero value

ISHE voltage induced by the SSE, but is opposite to that of the VNE voltage. Third, the enhancement of S is not observed in NbN/SiO_2/YIG trilayer samples, where the SiO_2 layer blocks the transmission of spin currents from YIG to NbN, but VNE is still expected to appear. For comparison of results between the two samples, the data taken at similar $T = T_{\rho\neq 0}$ values are shown where $T_{\rho\neq 0}$ is the temperature at which $\rho \neq 0$ begins to increase from the zero value. We don't use T_c for the parameter comparison because the temperature range of the resistance change is different for each sample. As shown in Fig. 3.5(e), on the other hand, negative voltage signals in positive magnetic fields are observed in NbN/SiO_2/YIG. S is almost linear with respect to H in the low-H regime, consistent with the VNE observed in the NbN/SiO_2 bilayer at similar temperatures shown in Fig. 3.4(c), although the magnitudes are slightly different.

In S/F structures, the magnetic stray field produced by the ferromagnetic layer can affect the transport in superconducting layers. Actually, it was reported that magnetic-field dependence of resistance is modulated at around the critical temperature in an Nb/bulk YIG hybrid system, owing to the magnetic stray field from Bloch walls in F layers [JAP 109, 083908 (2011)]. Since SSE voltage is also proportional to the resistivity of the sample, stray fields can affect the field dependence of SSE voltage. As seen in the low magnetic fields ($B < 0.1T$) at 9.5K, voltage noises which are probably caused by the stray field are surely observed.

On the other hand, in Fig. 3.5, we discuss the temperature dependence of SSE at high magnetic field ($B = 0.15$T), where the magnetization of our sample is already

saturated [Fig. 3.5(c)] and no magnetic domain exists. Hence we safely discard the influence of magnetic stray fields from YIG on the discussion on this peak.

Above 10.0 K, S is first constant and then decreases with decreasing T at 10.2 K. On the other hand, below 9.3 K, S is zero. In these two temperature regions, the T-dependence of S is consistent with that of ρ in NbN.

3.5 Discussion

Very recently, spin pumping into superconductors has been theoretically studied [99]. Following the theoretical approach of spin pumping into superconductors [103], we have calculated the spin current injected into a superconductor due to the SSE in a superconductor/ferrimagnet (S/F) bilayer system. This work is collaborated with Prof. Saburo Takahashi, Institute of Material research, Sendai, Japan.

In the presence of ΔT between F and paramagnetic metal layers, a spin current flows across the interface via SSE. Spin-flip scattering of electrons in the N layer takes place at the interface through the *s-d* exchange interaction with localized moments in the F layer, which accompanies a magnon excitation in the F layer. Making use of the linear response theory for the fluctuation dissipation theorem [75, 74] and the previous section, we obtain the spin current as

$$j^s_{N/F} = -\frac{1}{\hbar} N_I J^2_{\rm eff} \sum_{pq} \int_{-\infty}^{\infty} dt \, \langle S^+_q(t) S^-_{-q}(0) \rangle \, \langle \sigma^-_{-p}(t) \sigma^+_p(0) \rangle \,, \tag{3.23}$$

$$+ \frac{1}{\hbar} N_I J^2_{\rm eff} \sum_{p,q} \int_{-\infty}^{\infty} dt \, \langle S^-_{-q}(t) S^+_q(0) \rangle \, \langle \sigma^+_p(t) \sigma^-_{-p}(0) \rangle \,. \tag{3.24}$$

If we take only the lowest-order terms of each S operator for the magnon spin correlation function from Holstein-Primakoff representation, S operator is

$$S^-_{-q} \approx \sqrt{2S} b^\dagger_{-q}, \tag{3.25}$$

$$S^+_q \approx \sqrt{2S} b_q. \tag{3.26}$$

Its time evolution is

$$b_q(t) = b_q e^{-i\omega_q t} \tag{3.27}$$

$$b^\dagger_q(t) = b^\dagger_q e^{i\omega_q t}. \tag{3.28}$$

The creation and annihilation operators $b_q, b^\dagger_q$ have an anticommutation relation

$$[b_q, b^\dagger_{q'}] = \delta_{qq'} \tag{3.29}$$

as bose operator. From it,

$$\langle S^+_q(t) S^-_{-q}(0) \rangle = \langle b_q b^\dagger_q \rangle \, e^{-i\omega_q t} = [1 + n(\omega_q, T_F)] e^{-i\omega_q t}, \tag{3.30}$$

$$\langle S^-_{-q}(t) S^+_q(0) \rangle = \langle b^\dagger_q b_q \rangle \, e^{i\omega_q t} = n(\omega_q, T_F) e^{i\omega_q t} \tag{3.31}$$

are obtained. Note that the wavenumber q satisfies the translational symmetry since we are assuming a Brave lattice. Therefore, the equation of spin current induced by

SSE becomes

$$j^s_{N/F} = -\frac{1}{\hbar} N_I J^2_{\rm eff} \sum_q [1 + n(\omega_q, T_F)] \int_{-\infty}^{\infty} dt e^{-\omega_q t} \sum_p \langle \sigma^-_{-p}(t)\sigma^+_p(0)\rangle \tag{3.32}$$

$$+ \frac{1}{\hbar} N_I J^2_{\rm eff} \sum_q \int_{-\infty}^{\infty} dt e^{i\omega_q t} \sum_p \langle \sigma^+_p(t)\sigma^-_{-p}(0)\rangle \,. \tag{3.33}$$

Using the electron creation-annihilation operator $c, c^\dagger$, the spin correlation function in paramagnetic side can be written as scattering processes;

$$\langle \sigma^-_{-p}(t)\sigma^+_p(0)\rangle = \sum_{kk'} \langle c^\dagger_{k+p\downarrow}(t) c_{k\uparrow}(t) c^\dagger_{k'\uparrow}(0) c_{k'+p\downarrow}(0)\rangle \tag{3.34}$$

$$\langle \sigma^+_p(0)\sigma^-_{-p}(t)\rangle = \sum_{kk'} \langle c^\dagger_{k'\uparrow}(0) c_{k'+p\downarrow}(0) c^\dagger_{k+p\downarrow}(t) c_{k\uparrow}(t)\rangle \,. \tag{3.35}$$

Here for s wave superconductors, inverse Bogolubov transformation is applied to the electron operator, which is represented by

$$\alpha_{k\uparrow} = u_k \gamma_{k\uparrow} + v_k \gamma^\dagger_{-k\downarrow}, \tag{3.36}$$

$$\alpha^\dagger_{-k\downarrow} = u_{-k} \gamma^\dagger_{-k\downarrow} - v_k \gamma_{k\uparrow}. \tag{3.37}$$

We replace $c, c^\dagger$ with these operators. The calculation shows that the spin current $j^s_{S/F}$ in the case of S/F bilayer system flowing through the interface is

$$j^s_{S/F} = \frac{4\pi}{\hbar} S N_I [J_{\rm sd} v_s N(0)] \frac{1}{N_F} \sum_q [n(\omega_q, T_F, \mu_{\rm mag}) - n(\omega_q + \delta\mu, T_S)]$$

$$\times \int_{-\infty}^{\infty} dE \frac{|E(E+\omega_q)| + \Delta^2}{\sqrt{E^2 - \Delta^2}\sqrt{(E+\omega_q)^2 - \Delta^2}} [f(E - \delta_\mu/2) - f(E + \omega_q + \delta\mu/2)] \tag{3.38}$$

where n, f is the Bose fractional function and Fermi distribution function, respectively, ω_q is the energy dispersion of magnon, and $\mu_{\rm mag}$ is the chemical potential of magnon to make the chemical potential for a spin-split. We also included the chemical potential of Magnon, $\mu_{\rm mag}$ for generalization. T_F、T_S are the effective temperatures of Magnon and QP, respectively, and $\Delta(T)$ is the temperature-dependent superconducting gap. E is the energy of QP measured from the Fermi level.

For comparison of the calculation with the enhancement of S observed experimentally [Fig. 3.5(a)], we compute the equation (3.38), and plotted as a function of T/T_c. Here, we used the values of $T_c = 11$ K and $\Delta_0/k_{\rm B} = 2.08 T_c = 23$ K where Δ_0 is the superconducting gap at $T = 0$ for the strongly coupled superconductor NbN [105]. The temperature scale of Δ is much larger than that of the magnon gap energy of YIG estimated to be $g\mu_{\rm B}\mu_0 H/k_{\rm B} = 0.2$ K at $\mu_0 H = 0.15$ T, where g is the Lande's g factor (= 2.0 for YIG) and $\mu_{\rm B}$ is the Bohr magneton. Hence, we take into account the contribution only from low-frequency magnons in the calculation of Eq. (3.38). First, Fig. 3.6 shows the results of the calculation of the equation (3.38) for some ω_q/Δ_0. As shown in Fig. 3.6, the calculated spin-current signal is strongly enhanced just below T_c owing to the superconducting coherence effect, forming a coherence peak in the T range around T_c. For lower-frequency magnons

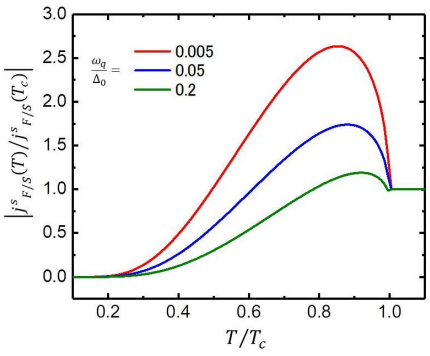

Figure 3.6 Temperature dependence of the spin current normalized by the value of T_c in the case of $\omega_q/\Delta_0 = 0.005, 0.05, 0.2$.

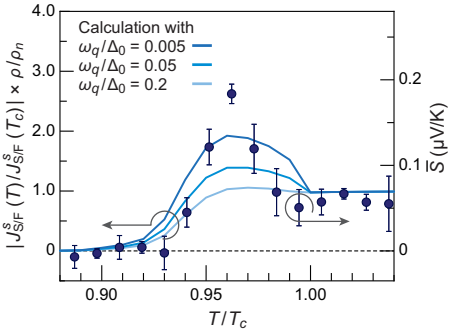

Figure 3.7 Comparison to a theoretical calculation. The results are shown as solid curves: $T = T_c$ dependence of $|V^s_{S/F}(T)/V^s_{S/F}(T_c)| = |j^s_{S/F}(\omega_q, T)\rho/j^s_{S/F}(\omega_q, T_c)\rho_n|$ (solid curves) is plotted for low magnon frequencies, $\omega_q/\Delta_0 = 0.005, 0.05, 0.2$ and Δ_0 are the magnon frequency and the magnitude of the superconducting energy gap at zero temperature, respectively. The experimental result is shown as filled circles: $T = T_c$ dependence of $\bar{V}$ (filled circles), which is defined by $[S_{\mathrm{NbN/YIG}} - \delta s S_{\mathrm{NbN/SiO_2/YIG}}]\Delta T$ with the adjusting parameter $\delta s = 0.92$ and $\Delta T = 1$K, is presented. Here, δs is assumed to be constant in this limited temperature range.

($\hbar\omega_q \ll \Delta$), a larger peak is calculated. Next, we compute the normalized ISHE voltage $|V^s_{S/F}(T)/V^s_{S/F}(T_c)| = |j^s_{S/F}(\omega_q, T)\rho/j^s_{S/F}(\omega_q, T_c)\rho_n|$, and plotted as a function of T/T_c. The experimental values for the SSE signal are calibrated as

$$\bar{V} \equiv \left[S_{\mathrm{NbN/YIG}} - \delta s S_{\mathrm{NbN/SiO_2/YIG}}\right] \Delta T, \tag{3.39}$$

where the VNE signal multiplied by the adjusting parameter δs is subtracted from S. The value of the adjusting parameter δs is chosen so that subtracting the pure VNE signal in $NbN/SiO_2/YIG$ from the signal containing both SSE and VNE in NbN/YIG removes the negative VNE contribution at fields $\mu_0 H = 0.2$ T. The result for $\delta s = 0.92$ and $\Delta T = 1$ K is plotted by filled circles in Fig. 3.7. As seen in Fig. 3.7, the temperature range where the enhancement of S is observed experimentally is reproduced by the calculation; both experimental and theoretical results are largest at $T \approx 0.96\ T_c$. The coherence-peak temperature in the calculation is a bit higher than

that reported in a microwave conductivity measurement for Nb ($0.8 \sim 0.9\ T_c$) [108]. This may be because, in Fig. 3.7, the normalized spin current $|j^s_{\mathrm{S/F}}(T)/j^s_{\mathrm{S/F}}(T_c)|$ is multiplied by the normalized resistivity ρ/ρ_n which rapidly decreases to zero below T_c. Since measured voltages are zero in the zero-resistivity state, the coherence-peak temperature shifts from $T \sim 0.9\ T_c$ expected in Eq. (3.38) to $T \sim 0.96\ T_c$ in Fig. 3.7. The magnitude of $\bar{S}$ enhancement is consistent with the theoretical calculation; compared to the normal-state values, the observed signal is enhanced by a factor of ~ 2.5 at $T/T_c \approx 0.96$, and the enhancement in the calculation is ~ 2 for $\hbar\omega_q/\Delta_0 = 0.005$. The small discrepancy in the magnitudes between the experimental and theoretical results could be due to impurity spin-orbit scattering, which may further enhance spin current owing to impurity vertex corrections [99].

Finally, we need to mention the recent experimental fact and theoretical implications. The detection of spin dynamics in NbN has been also demonstrated experimentally by spin pumping [100]. In this study, the Gilbert damping of GdN in the NbN/GdN/NbN trilayer structure was measured using FMR. The superconducting critical temperature is about 11 K for the heterostructures consisting of 10-nm NbN thin films. A large Gilbert damping peak is observed around T_c for the GdN sandwiched between two 10-nm NbN films, but not for the GdN sandwiched between 2-nm NbN films. This coherent peak of Gilbert damping is due to the enhancement of the dynamic spin susceptibility in the presence of impurity scattering. On the other hand, on the theoretical side, the interpretation in terms of the coherence peak effect in SSE was uncertain [101], since the coherence peak effect exists only in the low energy scale much less than the superconducting gap, whereas the SSE consists of spectrally broad components extended up to an energy scale much greater than the superconducting gap. Although we assumed that the spectral effect could be neglected under low temperature and low magnetic field conditions, strictly speaking, this condition needs to be considered. This means that the coherence peak effect of th SSE is expected to be drowned out completely in contrast to the case of spin pumping [101]. Another theoretical work provides us with an alternative interpretation of our SSE experiment in terms of the vortex spin Hall effect [102]. The vortices are excited in the wide fluctuation (liquid) regime such as cuprate superconductors or disordered conventioanl superconductors with the thin film structure as in the my experimental set-up. T. Taira *et al*. suggest that applying bias by the exchcange field from the adjusted F layer or dynamic stimulus due to the spin pumping, the superconducting vortex can host a spin polarization. Similarity to the vortex related thermoelectric effect in superconductors, a spin current carried by the transport of the spin-polarized vortices make the Hall voltage. The intersting point is that only a non-zero spin accmulation inside the vortex core is needed to excite the vortex spin Hall effect and the signal is propotional to the magnitude of the spin accumulation [102]. Their suggestion make it possible to explain my pronounced peak structure around T_c if we consider the change of resistivity due to the vortex pinning effect. Therefore, the origin of our experimental result is still ambiguous, and further experiments and discussions are

expected to continue from the perspective of not only spin dynamics of quasiparticles but also superconducting vortices.

3.6 Summary

In summary, we have achived thermal spin injection and elecrrical detection in supercondcting films. The temperature dependence of the SSE signal shows an increasing behavior around the superconducting transition temperature, whereas the signal disappears in the superconducting state. Following the theoretical approach of spin pumping into superconductors [103], we have calculated the spin current injected into a superconductor due to the SSE in a superconductor/ferrimagnet (S/F) bilayer system for making use of the BCS-Bogoliubov theory [77] and linear response theory for the fluctuation dissipation theorem [75, 74]. We found that the enhancement around the transition temperature is due to the change in the spin susceptibility of the superconducting film, known as coherence effect.

Chapter 4

Coupling control in YIG Cavity Resonator systems

The relevant energy scale for circuit electrodynamics experiments is in the microwave regime between a few hundred MHz and few GHz. In this study, the magnetization dynamics is excited by the high-frequency magnetic field created by microwaves propagating on microstrip line resonator. Measurements using microstrip lines can excite magnetization dynamics at arbitrary frequencies, allowing us to study frequency-dependent phenomena. Therefore praparing the suitable resonator in the microwave regime are required.

High Q-values and low energy-loss cavities have been mainly used to study the magnon-photon coupling. On the other hand, microstrip-based resonator technology is established in engineering to convey signals in microwave regime despite being the lower quality factors and higher radiation losses. Nevertheless, the microstrip resonators have some advantages compared to cavity. One important aspect is the signal of microstrip resonators well known for containing nearly no parasitic modes. In addition, the geometry of microstrip realize the situation of high filling factor η (The filling factor η is as indication of the sample in the magnetic field peaks compare to the volume of the resonator). Microstrip resonators are known for concentrating the magnetic field at the sample space and for having high η. Therefore, the major aim of this chapter is to examine a new type of microstrip-based resonator to couple with spin ensemble for application in the aspect of circuit electrodynamics and spintronics.

This work is in collaboration with Kurebayashi Lab in London Centre for Nanotechnology, UCL, UK.

4.1 Omega-shaped resonator's design

The substrate material used for the resonator should have low dielectric losses and high thermal conductivity. Low losses are important to improve the microresonator performance, whereas the high thermal conductivity substrate provides a heat sink for the power dissipated in the resonator elements. All above requirements are met by high resistivity silicon ($> 2500\ \Omega$cm)[23]. As an alternative substrate, we used a ceramic-polymercomposite with high dielectric constant (RO4003C from Rogers Corp.).

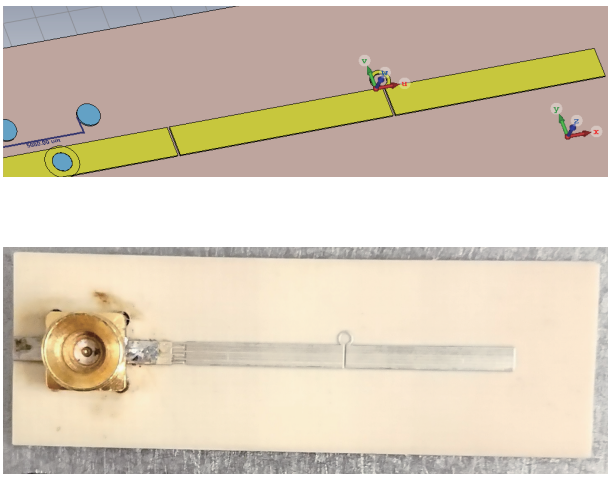

Figure 4.1 Cross section of the microstrip resonator with an incorporated coil. The microstrip-to-SMA connectors are not shown.

The voltage v induced by the precessing magnetisation $\boldsymbol{M}$ in the resonator coil can be calculated using the principle of reciprocity[24]

$$v(t) = -\int_{V_s} \frac{d}{dt}(\boldsymbol{B}_{1u}(\boldsymbol{r}) \cdot \boldsymbol{M}(\boldsymbol{r}, t))dV_s, \tag{4.1}$$

where $\boldsymbol{B}_{1u}(\boldsymbol{r}) = \boldsymbol{B}_{1u}(\boldsymbol{r}, t)/i(t)$ is the magnetic field at position $\boldsymbol{r}$ produced by a unitary current $i(t)$ carried by the microcoil and $\boldsymbol{M}(\boldsymbol{r}, t)$ is the spin magnetisation at this position. To calculate the limiting noise, we consider the thermal noise from the active resistance R of the coil,

$$N_{RMS} = \sqrt{4k_B T R \Delta f} \tag{4.2}$$

Here, T is the temperature of the coil and Δf is the bandwidth of detection electronics.

The signal from the microcoil can be maximised by increasing microwave efficiency factor of the resonator. The noise can be reduced by minimising the resistance of the coil trace R. Thus, the signal-to-noise ratio of the resonator can be optimised by adjusting the coil dimensions

$$(S/N) \propto B_{1u,\perp M}/\sqrt{R} \tag{4.3}$$

A thicker metallisation layer increases the active surface of the coil trace and thus reduces the influence of the skin effect at high frequencies and the active resistance of the coil.

We have used RO4003C (Rogers Corporation), a commercial PTFE/woven glass based laminate with copper cladding on one side of the substrate for design simulation and fabrication purpose. The dielectric is 0.8 mm thick (h) and has a relative permittivity (ϵ_{eff}) of 3.38. It has a loss tangent ($\tan\delta$) of 0.0027. A 0.1-mm thick copper and additional alminum layer for prevent oxdazation is present on one side of the substrate. We have simulated designs of planar half-wavelength resonators having

a geometry of omega-shaped provided by Christoph Zollitsch in London Centre for Nanotechnology, UCL, UK [25]. A microstrip feed line which is incorporated on the substrate and separated from the planar resonator by a gap g couples the microwave to the resonator.

Table4.1 Design Parameters - Omega Resonator

Parameter	Simulated result
Length of resonator (l)	52 mm
Coupling Gap (g)	0.1 mm
Width (w)	1.8 mm
Omega gap	0.15 mm
Omega inner radius	0.4 mm
Omega width	0.2 mm
Feedline length	11.85 mm

The design parameters are listed in tables. The resonator was designed to resonate at 3.2 GHz (f_0). The length of the resonators l is analytically given by $l + \Delta l = \lambda_g$ where λ_g is the guided wavelength and Δl is the correction term due to fringing electric fields and coupling gap. The geometries are indicated in the figure 4.1. To achieve efficient microwave power transfer to the resonator coil and acquisition of the signal from the sample, the impedance of the resonator must be matched to the 50 Ω coaxial line. The microwave power from a commercially available coaxial connector (SMA) has to be coupled to the resonator through the planar line.

4.2 Electromagnetic field analysis

The electromagnetic simulations of the resonators are carried out in CST Microwave Studio software using time domain solver with open boundary condition.

The simulation of the microstrip resonator with the incorporated microcoil reveals the electric field concentration on the line ends and the gap, as expected for the microstrip resonator, and strong magnetic field within the coil. Both field components are quite well spatially separated. The magnetic field distribution in the coil is quite nonuniform, following the $1/r$. Fig. 4.3 shows Electric (E), magnetic (H) field and surface current (I) distribution in the microstrip resonator with an incorporated coil on the substrate. The coil diameter is 0.4 mm.

In addition, the spatial distribution of each component of the RF field shows that the omega resonator as a whole has an nearly equal amount of in-plane and perpendicular components. Therefore, it is the mode near the ring that couples most strongly with the magnetic material, but both of the in-plane and out-of-plane modes simulated as Fig. 4.4 along the resonator can also drive the ferromagnetic resonance.

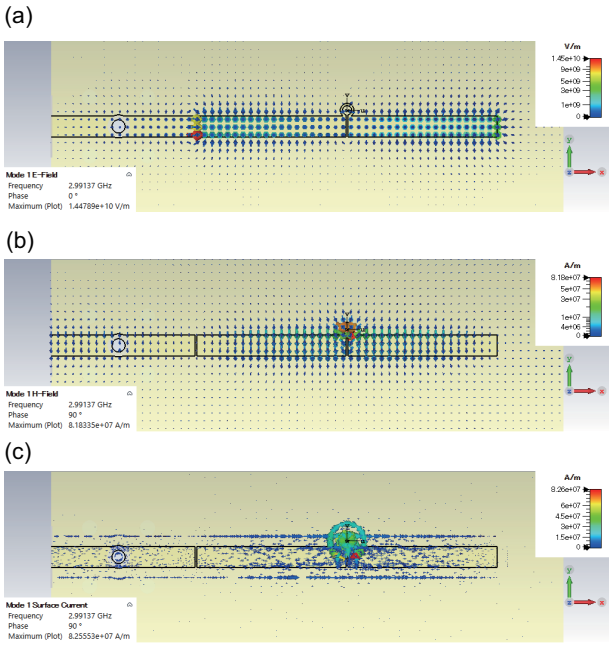

Figure 4.2 (a) Electric and (b) Magnetic fields and (c) surface surrent excited in OSR. Input power = 2 dBm.

4.3 Results from broadband VNA-FMR

The typical setup to measure broadband FMR is to use a vector network analyzer (VNA) and is usually called VNA-FMR. The VNA supply a microwave power at a given frequency in the signal line, the power P_{in} enter the stripline, a part of this power P_{abs} is absorbed within the stripline and by the sample and the output power $P_{\text{out}} = P_{\text{in}} - P_{\text{abs}}$ is measured using the detector of the VNA. The external DC magnetic field H_{DC} is swept and at the ferromagnetic resonance, the absorbed power which is propotional to $\omega\chi'' h_{rf}^2$ will become maximum and thus the output power detected by the VNA will decrease. It is therefore possible to measure the ferromagnetic resonance using a VNA-FMR setup.

The frequency response of the CPW is shown in the figure 4.5(b). The input power is fixed at 1 mW in all experiments. The CPW's characteristics are obtained over a wide frequency range. In general, the worse transmission characteristics at higher frequencies are due to the fact that the dielectric and magnetic losses are proportional to the frequency. The characteristic impedance measured from the parameters is $50 \sim 52\ \Omega$, which satisfies the impedance matching condition. On the other hand, the strong power absorption around 10.5 GHz is assumed to be the resonance due to the standing waves along PCB. This part of the data was excluded in the analysis.

The $\omega - H$ spectrum and extraction of the main ferromagnetic properties of a YIG grown on a GGG substrate is provided in Fig. 4.6(a),(b). The thickness of the film is 5μm. It is our main sample for the resonator measurement. For the analysis, we

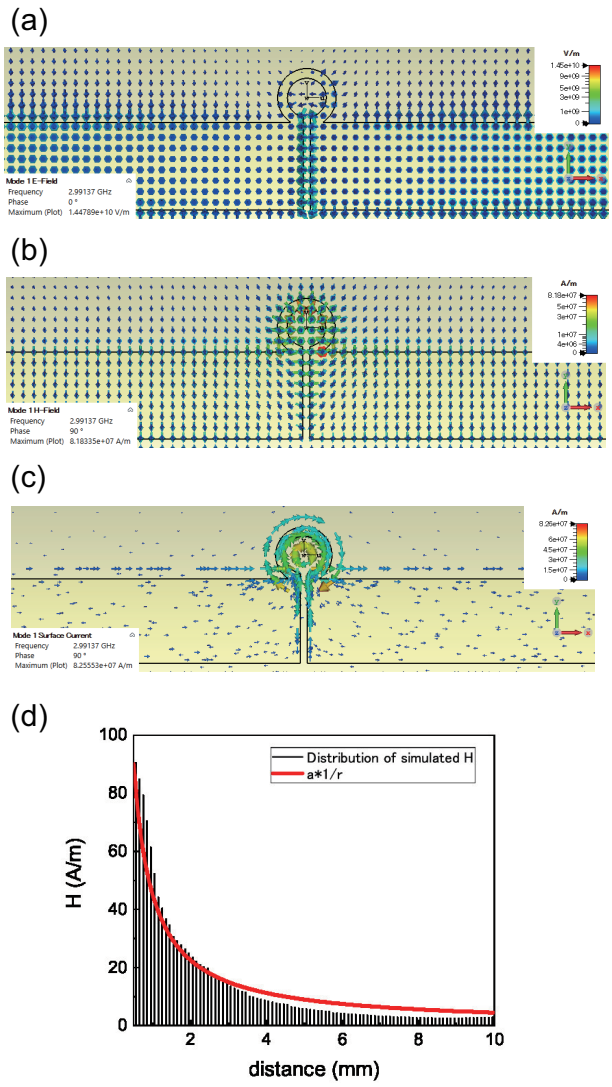

Figure 4.3 Expanded figures of Fig. 4.2 and the distance dependence of the magnetic field strength from the center of the ring .

subtracted the background at $\mu_0 H_0 = 0$ mT data from the raw data. The FMR-induced power absorptions are obtianed for different magnetic field from 1.0 to 14.0 GHz as seen in figure 4.6(b). It is possible to obtain the resonance field H_{res} and the linewidth Δf as a function of frequency. The extracted values are then fitted using the Kittel formula given in equation (1.29) and equation (2.38). As can be seen in figure 4.6(c) and figure 4.6(d), it is possible to extract some of the magnetic properties of the YIG film. In particular, we can obtain the electron gyromagnetic ratio, $\gamma_e = 26.6 \pm 0.1$ GHz/T, the saturation magnetization $M_s = 177 \pm 3$ mT, and the Gilbert damping $\alpha = 1.1 \times 10^{-3} \pm 0.2$. These extracted values are typical of a LPE-grown 5μm thick YIG film deposited on GGG reported in the reference [33].

We also measured in the low frequency range of 1-4 GHz as shown in Fig. 4.7. Note that the analysis here is under the magnetic field domain, not in the frequency domain,

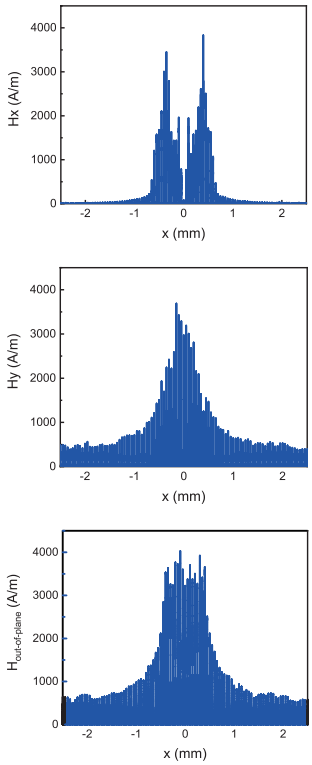

Figure 4.4 Spatial distribution of the microwave magnetic field in each direction (a) H_x, (b) H_y, and (c) H_z.

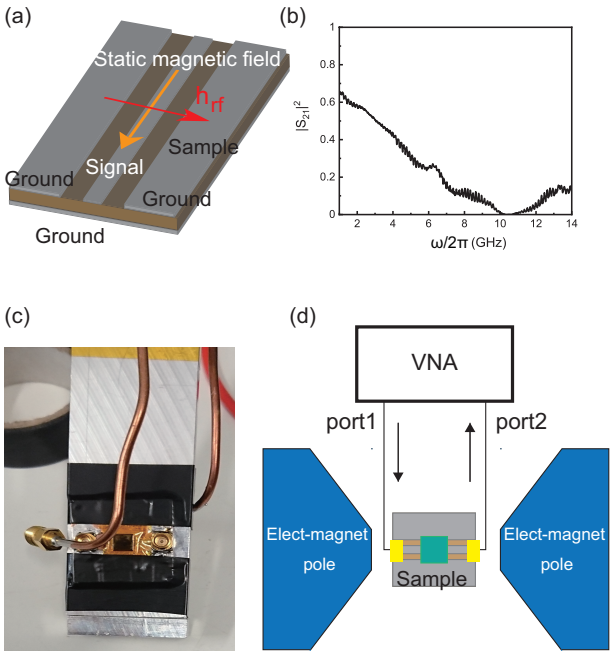

Figure 4.5 (a) The structure of the coplanar waveguide (CPW), (b) frequency response of the CPW with no sample, (c) photo, and (d) schematic illustration of a typical VNA-Broadband FMR setup and its main elements.

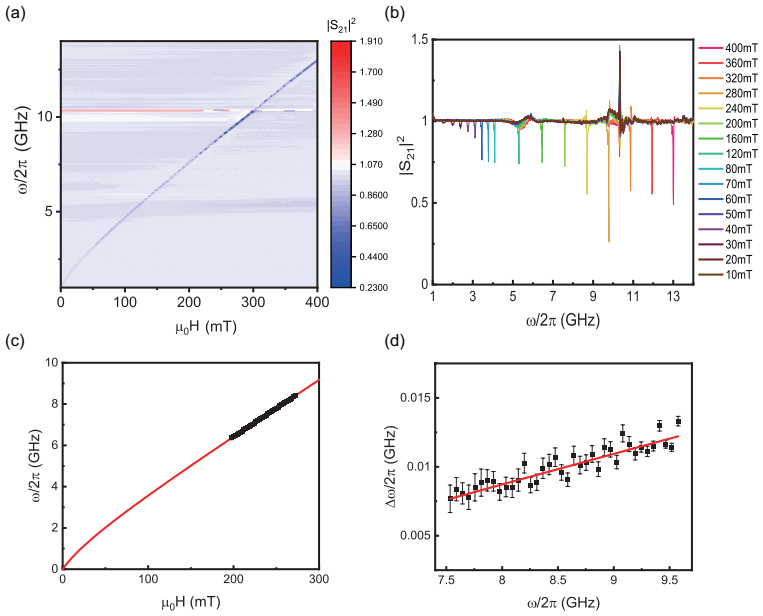

Figure 4.6 Typical results obtained from a broadband FMR measurement. (a) $|S_{21}|^2$ transmission spectra represented on the plane of microwave frequency and magnetic field ($\omega - H$ plane), (b) The FMR signals obtained at different magnetic fields. (c) The resonance frequencies and (d) frequency linewidths obtained from the raw data. Solid curves shown in (c) and (d) are fitted results using the equation (1.29) and (2.38), respectively.

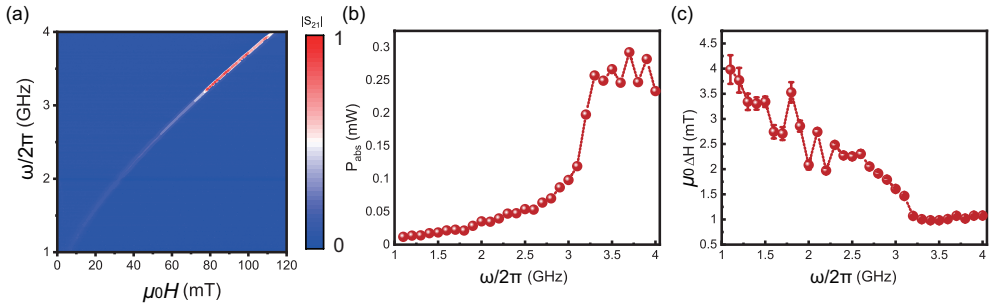

Figure 4.7 Typical results obtained from a broadband FMR measurement for 1-4 GHz. (a) Normalized $|S_{21}|$ power spectrum, (b) frequency dependence of FMR absorptions, and (c) frequency dependence of the field linewidth.

so that the linewidths are evaluated in ΔH. We obtained the frequency dependence of the microwave absorption when H is applied along the feedline. The dependence of the P_{abs} and $\mu_0 \Delta H$ on the microwave frequency changes dramatically as shown in Figs. 4.7(b) and 4.7(c) at $\omega_c/2\pi = 3.3$ GHz. This is similar to the behavior reported by Kurebayashi *et al.* [26] for the DC spin-pumping voltage in YIG/Pt structures. The phenomenon originates from the nonlinearity of the magnetization dynamics in the YIG film due to the anisotropic magnon dispersions as discussed in introduction part. Therefore, one can conclude that the observed decrease of is $P_{\rm abs}$ and increase of $\Delta\omega/2\pi$ is due to the change of the magnetic susceptibility owing to nonlinear effect

in YIG.

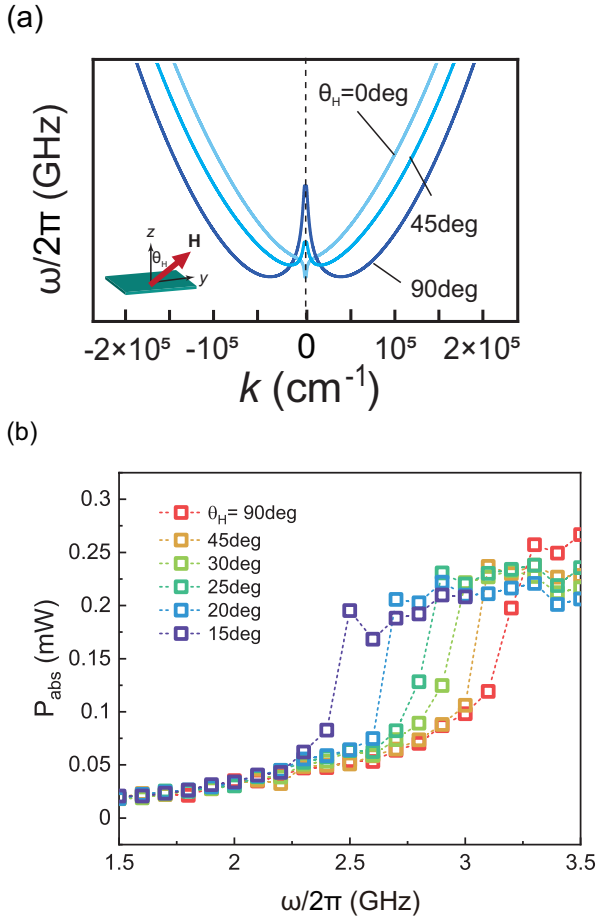

Figure 4.8 (Top) Dispersion curves for the lowest sw eigen-wave ($n = 0$) propagating in the film with totally unpinned surface spins along the projection of the bias magnetic field. Different curves correspond to the different polar angles 0, 45, 90 deg between the film normal and the bias magnetic field. (bottom) Frequency dependence of the absorbed power for each angle.

As already mentioned, in order to induce nonlinear effects as 3-magnon scattering, high microwave power beyond the nonlinear threshold is necessary. In additon, we have to consider a shape-dependent demagnetization field along the thickness direction. In ferromagnetic resonance, this interaction causes the magnetization to follow an elliptical orbit, which affects the nonlinear magnetization dynamics. Since the dipole interaction depends on the relative angle between the dipoles, we wondered if the critical frequency could be controlled by changing the direction of the magnetization with the external magnetic field. In Fig. 4.8(a), the dispersion characteristics of spin wave in ferromagnetic films depend critically on the direction of wave propagation and on the direction of bias magnetic field. It turns out that the critical frequency does indeed vary with the angle of the external magnetic field, θ_H. Comparing with the dispersion relation, it is found that the dip in dispersion is suppressed and the exchange interaction becomes dominant where the dipole interaction becomes weak.

In the FMR measurement, the critical frequency decreases as approaching the magnetic field angle θ_H to the out-of-plane direction, as seen in Fig. 4.8(b). Thus, the critical frequency of three-magnon scattering can be controlled by the angle rotation of the external magnetic field.

4.4 Results from broadband VNA-FMR with Resonator

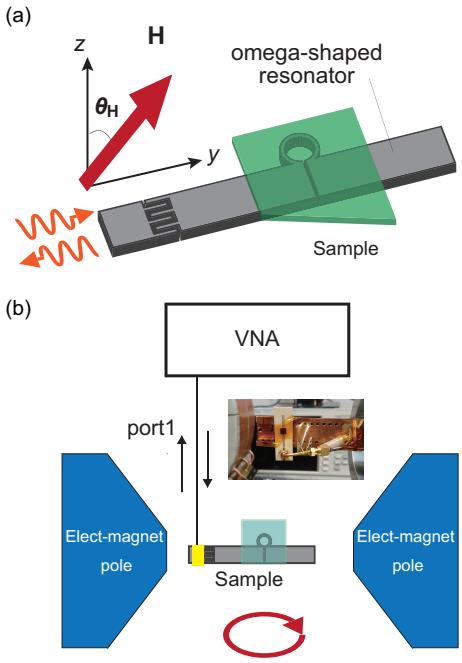

Figure 4.9 Schematic reprensentation of a Typical VNA-Broadband FMR setup and its main elements with the Omega-shaped resonaotor (OSR).

Same broadband FMR measurement setup allows to measure the ferromagnetic resonance and the resonator's absorption on a wide frequency range. We measured the $|S_{11}|$ spectra as a function of the microwave frequency f of oscillating currents flowing in the microstrip resonator line for the indicated values of different magnetic-field strengths at an angle $\theta_H = 0$ deg, where θ_H is the angle between the magnetic field direction and the z-axis. Figure 4.10(b) illustrates the $|S_{11}|$ spectra measured by applying oscillating currents along the stripline from only the Omega-shaped resonator (without the YIG film). Only the pure photon mode of the Omega-shaped resonator (OSR) appeared at $\omega_0/2\pi = 2.81$ GHz along with a full width at half maximum (FWHM) $\Delta\omega_{\mathrm{FWHM}}/2\pi \sim 323$ MHz and a quality factor $Q_{\mathrm{unloaded}} = \omega/\Delta\omega_{\mathrm{FWHM}} \sim 87$ (see Fig. 4.10(a)). However, for the hybrid of the OSR and the YIG film, resonance frequency shifts to the lower side and $|S_{11}|$ amplitude deacrease. In this configuration, the photon mode of the OSR appeared at $\omega_0/2\pi = 2.78$ GHz along with a full width at half maximum (FWHM) $\Delta\omega_{\mathrm{FWHM}}/2\pi \sim 497$ MHz and a quality factor $Q_{\mathrm{loaded}} = \omega/\Delta\omega_{\mathrm{FWHM}} \sim 56$ (see Fig. 4.10(a)). This frequency shift is reflected in the increase in dielectric constant due to the placement of the YIG, and in addition, the intensity

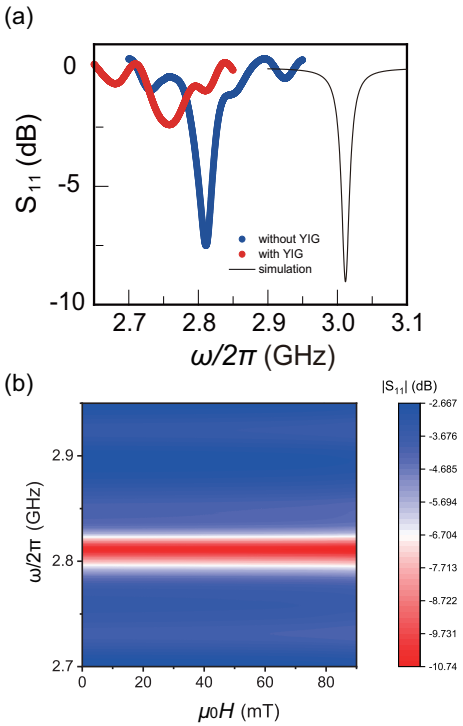

Figure 4.10 Frequency response of the OSR used in the experiment and $|S_{21}|^2$ transmission spectra represented by $|S_{21}|^2$ power on the plane of microwave frequency and magnetic field ($\omega - H$ plane).

of $|S_{11}|$ is reduced due to the absorption of microwaves by the YIG sample. Also, the photon mode peak does not much move with increasing $\mu_0 H$. This result indicates that there is no additional coupling between the photon mode and applied static magnetic field.

The $|S_{11}|$ spectra measured for the OSR-YIG hybrid. In Fig. 4.11(a), it is clear that there exists a crossing effect between the OSR and the FMR modes. From the Fig. 4.11, it is evident that the width of photon mode of the OSR is ∼10 times higher in gain than the magnon modes of the YIG film and threre's no anti-crossing as discussed in strong coupling region, which indicates that our experiment is under weak coupling condition [109, 110, 111]. Also, in the spectra, the peak shifts to higher frequencies with the applied magnetic field, indicating that this is an FMR mode. On the other hand, it is clear from the previous results that the spin-wave mode of finite wavenumber is excited in the thin film in contrast to the Kittel mode of $k = 0$, where the peak shifts to higher frequencies with the magnetic field. If we look at the coupling here, we can see that the extra peak structures of the coupling modes were observed in addition to the two fundamental coupling modes between the OSR and the YIG film. Especially, the BVMSW mode is on the low-frequency side of the Kittel mode couples depending on the field angle. In this experiment, it is confirmed that the spin wave mode is also coupled with the photon mode of the resonator. However, the details are not included, because it was not possible to distinguish the spin wave

clearly due to the standing wave on the SMA cable as a background.

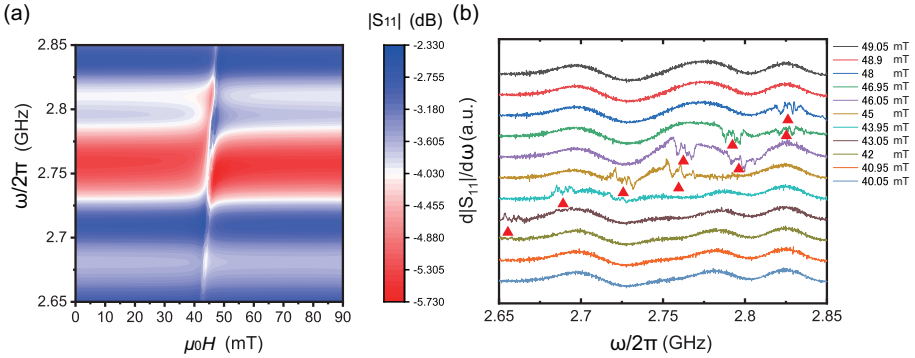

Figure 4.11 (a) Frequency response of the OSR used in the experiment and $|S_{11}|$ reflection spectra represented by $|S_{11}|$ power on the plane of microwave frequency and magnetic field ($\omega - H$ plane). (b) Field dependence of FMR absorption of spin waves.

Following the FMR measurement, the $|S_{11}|$ spectra with resonator is estimated that it also changes remarkably with the field direction. We measured the angular dependence of the photon-magnon coupling by varying the magnetic field direction θ_H on the $y-z$ plane with respect to the x-axis (see Fig. 4.10). Figure 4.12 illustrates the experimentally observed $|S_{11}|$ power on the $\omega - H$ plane for different angles from $\theta_H = 10$ deg to 90 deg per 10 deg.

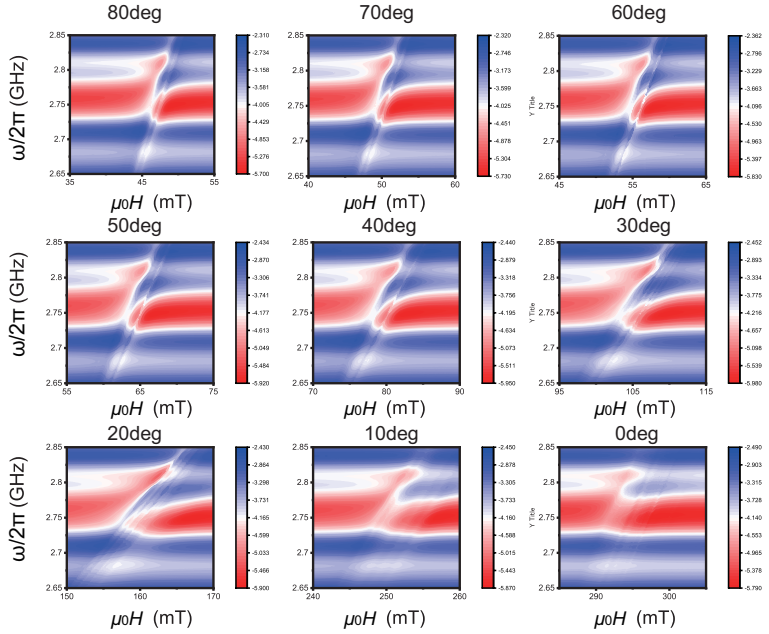

Figure 4.12 Frequency response of the OSR used in the experiment and $|S_{11}|$ reflection spectra represented by $|S_{11}|$ power on the plane of microwave frequency and magnetic field ($\omega - H$ plane) for different angles from $\theta_H = 10$ deg to 90 deg per 10 deg.

With decreasing θ_H, the coupling between OSR and YIG film becomes weaker and at $\theta_H = 0$ deg (out-of-plane configuration) it almost disappears. We have to examine the characteristic of this angle dependence. The coupling state is analyzed in the following method; All the background signal at which only the resonator mode appears is chosen at $\mu_0 H = 0$ mT. Comparing with all the background signal, we confirm that they have no angle dependence ($|S_{11}|$ is slightly changed but not much and all the resonance frequency is constant $\omega_{\rm res}^{\rm OSR}/2\pi = 2.76$ GHz) of the external static field. Based on this fact, we substract these background from the raw data as

$$|S_{11}|^N \equiv \frac{|S_{11}|^{\rm raw} - |S_{11}|^{\rm background}}{|S_{11}|^{\rm background}} \tag{4.4}$$

We define the positive part of the ratio $|S_{11}|^N_{>0}$ as the coupling strength because it is the coupled response estimated from the resonator peak to the negative peak of coupling state. The coupling strength is especially chosen to the signals at crossing point (it means $\omega_{\rm res}^{\rm FMR}/2\pi = \omega_{\rm res}^{\rm OSR}/2\pi$).

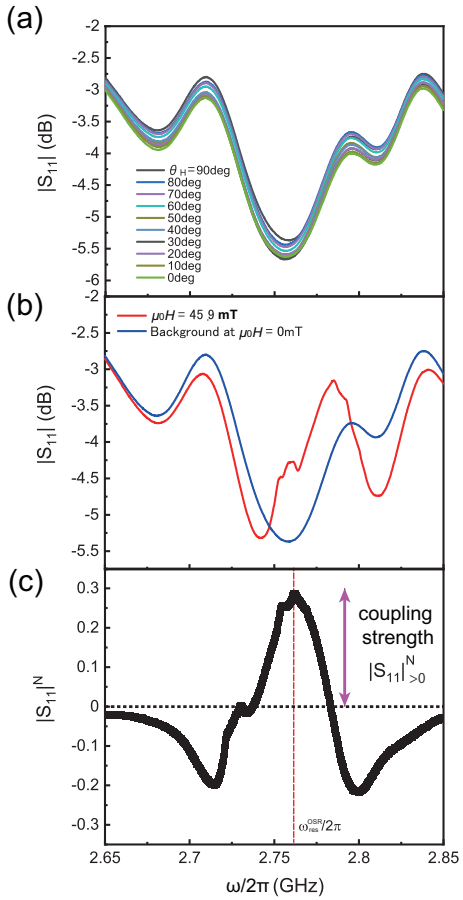

Figure 4.13 (a) Frequency dependence of $|S_{11}|$ reflection spectra of The OSR without the sample at each magnetic field angle. (b) Frequency response of the OSR represented by $|S_{11}|$ with applying the in-plane magnetic field ($\theta_H = 90$deg). (c) Frequency response of the normalized $|S_{11}|^N$.

The angle dependence of the resonance field can allow us to obtain the magnetic

properties of the ferromagnet. To do so we will use the same method as the one previously described by Ando *et al.* [32]. The direction of the xyz axis is the same in this section as in the paper. This is to avoid mistakes in the description.

The dynamics of magnetization $\boldsymbol{M}(t)$ in a ferromagnetic film unde an effective magnetic field $\boldsymbol{H}_{\text{eff}}$ is described by the LLG equation

$$\frac{d\boldsymbol{M}(t)}{dt} = -\gamma \boldsymbol{M}(t) \times \boldsymbol{H}_{\text{eff}} + \frac{\alpha}{M_s} \boldsymbol{M}(t) \times \frac{d\boldsymbol{M}(t)}{dt}. \tag{4.5}$$

Here, γ, α, and M_s are the gyromagnetic ratio, the Gilbert damping constant, and the saturation magnetization, respectively. We consider the Eq. (4.5) in an equilibrium condition, where the equilibrium magnetization direction $\boldsymbol{M}$ is directed to the y axis [see Fig.]. Here, we neglect the magnetocrystaline anisotropy for simplicity. The external magnetic field $\boldsymbol{H}$ and the static demagnetization field $\boldsymbol{H}_M$ induced by $\boldsymbol{M}$ are taken into account as the effective field $\boldsymbol{H}_{\text{eff}}$:

$$\boldsymbol{H}_{\text{eff}} = \boldsymbol{H} + \boldsymbol{H}_M, \tag{4.6}$$

$$\boldsymbol{H} = H \begin{pmatrix} 0 \\ \sin(\theta_M - \theta_H) \\ \cos(\theta_M - \theta_H) \end{pmatrix}, \tag{4.7}$$

$$\boldsymbol{H}_M = -M_s \cos\theta_M \begin{pmatrix} 0 \\ \sin\theta_M \\ \cos\theta_M \end{pmatrix}. \tag{4.8}$$

θ_H and θ_M are the external-magnetic-field-angle and the magnetization angle to the normal axis of the film plane, respectively [see the inset in Fig. 4.14(b)]. The static equilibrium condition, namely, $\boldsymbol{M} \times \boldsymbol{H}_{\text{eff}} = 0$, yields an expression, which relates θ_H and θ_M, as

$$2H \sin(\theta_H - \theta_M) + M_s \sin 2\theta_M = 0, \tag{4.9}$$

where H is the strength of the external magnetic field.

We then consider the magnetization $\boldsymbol{M}(t)$ precession around the magnetization axis, where $\boldsymbol{M}(t) = \boldsymbol{M} + \boldsymbol{m}(t)$ as shown in Fig. 4.14(b). By ignoring the second order contribution of the precession amplitude, m_x and m_y, we find the ferromagnetic resonance condition

$$\left(\frac{\omega_0}{\gamma}\right)^2 = \mu_0^2 [H_{\text{res}} \cos(\theta_H - \theta_M) - M_s \cos 2\theta_M] \times [H_{\text{res}} \cos(\theta_H - \theta_M) - M_s \cos^2 \theta_M]. \tag{4.10}$$

Since the resonant magnetic field is in good agreement with the calculation results, the data used in the angular dependence is appropriate. On the other hand, the angular dependence of $|S_{11}|^N_{>0}$ increases up to around $\theta_H = 30$ deg, and the increase is suppressed at higher angles (in-plane configuration). In the following, we discuss the origin of the behavior from the angle dependence of the coupling between magnons and photons and nonlinear magnetization dynamics in the spin system.

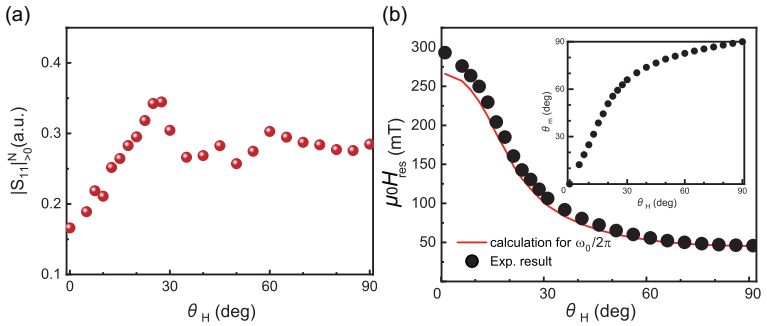

Figure 4.14 Angle dependence of (a) $|S_{11}|^N_{>0}$ and (b) resonace field $H_{\rm res}$.

4.5 Discussion

4.5.1 Static field angle dependence of the magnon-photon coupling

This work is collaborated with Dr. Kei Yamamoto, JAEA, Ibaragi, Japan.

We consider a single cavity photon mode denoted by the annihilation operator $\hat{a}$, and model the YIG film as a set of spins $\hat{S}_i$ where the index $1 \leq i \leq N$ denotes the site at which $\hat{S}_i$ is located [112]. The total number of spins N is macroscopically large. Let ω_p be the resonance frequency of the cavity and $\boldsymbol{B}_0$ be the static magnetic field. The Hamiltonian of the system then takes the following form:

$$\hat{H} = \hbar\omega_p \hat{a}^\dagger \hat{a} + g\mu_B \sum_i \left\{ \boldsymbol{B}_0 + \boldsymbol{B}_p(\boldsymbol{r}_i)\hat{a} + \bar{\boldsymbol{B}}_p(\boldsymbol{r}_i)\hat{a}^\dagger \right\} \cdot \hat{\boldsymbol{S}}_i + \sum_{ij} \hat{S}_i J_{ij} \hat{S}_j. \tag{4.11}$$

We have assumed that all the spins have the same g-factor. $\boldsymbol{B}_p(\boldsymbol{r})$ is the mode profile of the magnetic field of the cavity mode, which is in general complex. Overvars denote complex conjugation, $\boldsymbol{r}_i$ the position vector of the ith spin, and J_{ij} are matrices of exchange and dipole-dipole interactions whose explicit forms are not needed.

Suppose $\boldsymbol{B}_0 = -B_0\boldsymbol{\xi}, |\boldsymbol{\xi}| = 1$ and $\boldsymbol{B}_0$ is suffciently large so that the ground state of the spins is $\hat{\boldsymbol{S}}_i = S\boldsymbol{\zeta}$. Let us write $\zeta = (\sin\theta\cos\phi, \sin\theta\sin\phi, \cos\theta)$ and construct Cartesian coordinate axes $\{\xi, \eta, \zeta\}$ by

$$\boldsymbol{\xi} = (-\sin\phi, \cos\phi, 0), \ \boldsymbol{\eta} = (-\cos\theta\cos\phi, \cos\theta\sin\phi, \sin\theta). \tag{4.12}$$

One may introduce the Holstein-Primakoff boson operators $\hat{c}_i$ by

$$\hat{S}_\xi = \sqrt{\frac{S}{2}}\sqrt{1 - \frac{\hat{c}_i^\dagger \hat{c}_i}{2S}}(\hat{c}_i + \hat{c}_i^\dagger), \ \hat{S}_\eta = -i\sqrt{\frac{S}{2}}\sqrt{1 - \frac{\hat{c}_i^\dagger \hat{c}_i}{2S}}(\hat{c}_i - \hat{c}_i^\dagger), \ \hat{S}_\zeta = S - \hat{c}_i^\dagger \hat{c}_i, \tag{4.13}$$

where $\hat{\boldsymbol{S}}_i = \hat{S}_\xi\boldsymbol{\xi} + \hat{S}_\eta\boldsymbol{\eta} + \hat{S}_\zeta\boldsymbol{\zeta}$. Hereafter, we just write operators without hat for simplicity. Substituting these into Eq. (4.11) yields

$$\begin{aligned}\hat{H} =& -\hbar\omega_p a^\dagger a + \sum_{ij} \begin{pmatrix} c_i^\dagger & c_i \end{pmatrix} J_{ij} \begin{pmatrix} c_i^\dagger \\ c_i \end{pmatrix} + g\mu_B \sum_i \left\{ \boldsymbol{B}_p(\boldsymbol{r}_i)a + \bar{\boldsymbol{B}}_p(\boldsymbol{r}_i)a^\dagger \right\} \cdot \zeta(S - c_i^\dagger c_i) \\ &+ g\mu_B \sqrt{\frac{S}{2}} \sum_i \sqrt{1 - \frac{c_i^\dagger c_i}{2S}} \left\{ \boldsymbol{B}_p(\boldsymbol{r}_i)a + \bar{\boldsymbol{B}}_p(\boldsymbol{r}_i)a^\dagger \right\} \cdot \left\{ (\boldsymbol{\xi} - i\boldsymbol{\eta})c_i + (\boldsymbol{\xi} + i\boldsymbol{\eta})c_i^\dagger \right\} \\ &+ \text{higher order terms.}\end{aligned} \tag{4.14}$$

J_{ij} are two-by-tow matrices that determine the spin wave dispersion relations. The third term can be considered a renormalisation of the cavity mode by its coupling to the magnet so that we drop it with understanding that $\omega_p, \boldsymbol{B}_p$ properly take account of it. The second line is the cavity-magnon interaction while the higher order terms generate the three-magnon splitting (Suhl instability) and other non-linear effects. To obtain the spin wave eigenmodes, one diaognalises J_{ij} by the transformation

$$\begin{pmatrix} b_n \\ b_n^\dagger \end{pmatrix} = \sum_i \begin{pmatrix} U_{ni} & V_{ni} \\ \bar{V}_{ni} & \bar{U}_{ni} \end{pmatrix} \begin{pmatrix} c_i \\ c_i^\dagger \end{pmatrix}, \ \sum_n (\bar{U}_{ni}U_{nj} - V_{ni}\bar{V}_{nj}) = \delta_{ij}, \ \sum_n (\bar{U}_{ni}V_{nj} - V_{ni}\bar{U}_{nj}) = 0 \tag{4.15}$$

Note that for translationally invariant ferromagnets, the eigenmode index n is usually the wavevector $\boldsymbol{k}$. Using its inverse relation

$$\begin{pmatrix} c_i \\ c_i^\dagger \end{pmatrix} = \sum_n \begin{pmatrix} \bar{U}_{ni} & -V_{ni} \\ -\bar{V}_{ni} & U_{ni} \end{pmatrix} \begin{pmatrix} b_n \\ b_n^\dagger \end{pmatrix}, \tag{4.16}$$

and introducing

$$B_p^\pm(\boldsymbol{r}_i) = \boldsymbol{B}_p(\boldsymbol{r}_i) \cdot (\boldsymbol{\xi} \pm i\boldsymbol{\eta}), \tag{4.17}$$

one can rewrite the Hamiltonian as

$$\begin{aligned} \mathcal{H} &= \hbar\omega_p a^\dagger a + \hbar \sum_n \omega_n b_n^\dagger b_n \\ &+ g\mu_B \sqrt{\frac{S}{2}} \sum_{ni} \left[\left\{ B_p^+(\boldsymbol{r}_i) U_{ni} - B_p^-(\boldsymbol{r}_i) V_{ni} \right\} a b_n^\dagger + h.c. \right] \\ &- g\mu_B \sqrt{\frac{S}{2}} \sum_{ni} \left[\left\{ B_p^+(\boldsymbol{r}_i) \bar{V}_{ni} - B_p^-(\boldsymbol{r}_i) \bar{U}_{ni} \right\} a b_n + h.c. \right] \end{aligned} \tag{4.18}$$

where

$$n_i = \sum_{nm} (U_{ni}\bar{U_{mi}} b_n^\dagger b_m + \bar{V_{ni}} V_{mi} b_n b_m^\dagger - V_{ni}\bar{U}_{mi} b_n b_m - U_{ni} V_{mi} b_n^\dagger b_m^\dagger). \tag{4.19}$$

In the second term, ω_n is the eigenfrequency of the nth spin wave mode. We apply the mean-field approximation by replacing n_i by its average $\langle n_i \rangle \equiv n_i$. Introducing the effective coupling constants

$$g_{\text{effn}} = \frac{g\mu_B}{\hbar} \sqrt{\frac{S}{2}} \sum_i \sqrt{1 - \frac{n_i}{2S}} \left\{ B_p^+(\boldsymbol{r}_i) U_{ni} - B_p^-(\boldsymbol{r}_i) V_{ni} \right\}, \tag{4.20}$$

$$\tilde{g}_{\text{effn}} = \frac{g\mu_B}{\hbar} \sqrt{\frac{S}{2}} \sum_i \sqrt{1 - \frac{n_i}{2S}} \left\{ B_p^+(\boldsymbol{r}_i) \bar{V}_{ni} - B_p^-(\boldsymbol{r}_i) \bar{U}_{ni} \right\}, \tag{4.21}$$

formally things look simple as

$$\mathcal{H} = \hbar\omega_p a^\dagger a + \hbar \sum_n \omega_n b_n^\dagger b_n + \hbar \sum_n \left(g_{\text{effn}} a b_n^\dagger + \bar{g}_{\text{effn}} a^\dagger b_n + \tilde{g}_{\text{effn}} a b_n + \bar{\tilde{g}}_{\text{effn}} a^\dagger b_n^\dagger \right) \tag{4.22}$$

First of all, note that U_{ni}, V_{ni} correspond to the spatially dependent spin wave profiles. Therefore keeping Kittel mode (with $n = 1$) only means setting $U_{1i} = U, V_{1i} = V$ and discarding all the modes with $n \geq 2$. As the result the Hamiltonian reduces to

$$\mathcal{H} = \hbar\omega_p a^\dagger a + \hbar\omega_0 b^\dagger b + \hbar(g_{\text{eff}} a b^\dagger + \bar{g}_{\text{eff}} a^\dagger b + \tilde{g}_{\text{eff}} a b + \bar{\tilde{g}}_{\text{eff}} a^\dagger b^\dagger). \tag{4.23}$$

Here we dropped the index $n = 1$ and $\omega_1 \to \omega_0$ to follow the usual convention.

We also adopt rotating wave approximation that is essentially means setting $\tilde{g}_{\text{eff}} = 0$. The justification comes from assuming the time-dependences $a \propto e^{-i\omega_p t}, b \propto e^{-i\omega_o t}$. Then near the crossing $\omega_p \sim \omega_0$, the terms proportional to $ab, a^\dagger b^\dagger$ vary much faster than $a^\dagger b$ so that on a slow-time scale, the former can be averaged out.

Now we have a single, but in general complex, coupling constant

$$g_{\text{eff}} = \frac{g\mu_B}{\hbar}\sqrt{\frac{S}{2}}\sum_i \sqrt{1-\frac{n_i}{2S}}\left\{B_p^+(\boldsymbol{r}_i)U - B_p^-(\boldsymbol{r}_i)V\right\} \tag{4.24}$$

where

$$\begin{aligned} B_p^+(\boldsymbol{r}_i) &= -B_p^x(\boldsymbol{r}_i)\sin\phi + B_p^y(\boldsymbol{r}_i)\cos\phi \\ &\quad - i\left\{B_p^x(\boldsymbol{r}_i)\cos\theta\cos\phi + B_p^y(\boldsymbol{r}_i)\cos\theta\sin\phi - B_p^z(\boldsymbol{r}_i)\sin\theta\right\}, \qquad (4.25) \\ B_p^-(\boldsymbol{r}_i) &= -B_p^x(\boldsymbol{r}_i)\sin\phi + B_p^y(\boldsymbol{r}_i)\cos\phi \\ &\quad + i\left\{B_p^x(\boldsymbol{r}_i)\cos\theta\cos\phi + B_p^y(\boldsymbol{r}_i)\cos\theta\sin\phi - B_p^z(\boldsymbol{r}_i)\sin\theta\right\}. \qquad (4.26) \end{aligned}$$

As shown explicitly here, therefore, g_{eff} depends on the angle of the ground state magnetization strongly. As we have noted earlier, $B_p^{x,y,z}(\boldsymbol{r}_i)$ are in general complex. But when the cavity mode can be considered linearly polarised, one can choose $\boldsymbol{B}_p(\boldsymbol{r}_i)$ to be real. It also turns out possible to always choose U, V to be real. Under these conditions, the coupling reduces to

$$\begin{aligned} g_{\text{eff}} = \frac{g\mu_B}{\hbar}\sqrt{\frac{S}{2}}\sum_i \sqrt{1-\frac{n_i}{2S}}[&\left\{-B_p^x(\boldsymbol{r}_i)\sin\phi + B_p^y(\boldsymbol{r}_i)\cos\phi\right\}(U-V) \\ &- i\left\{B_p^x(\boldsymbol{r}_i)\cos\theta\cos\phi + B_p^y(\boldsymbol{r}_i)\cos\theta\sin\phi - B_p^z(\boldsymbol{r}_i)\sin\theta\right\}(U+V)]. \end{aligned} \tag{4.27}$$

Note that the coupling is still complex and depends strongly on the angle. Fig. 4.15 shows the simulated result of g_{eff} for $\theta = \theta_H, \phi = 90$deg by Eq. (4.27). Each components of the θ_H-dependent cavity field (B_p^y and B_p^z) are estimated from the spatial integration of the RF magnetic field over the sample area because in the case of that the sample is larger than the resonator' s line, all the spatial components of the microwave should be considered (see Fig. 4.4). To reproduce the angle dependence of g_{eff} of the experimental results (peak at $\theta_H = 20$ deg), the y-component of the resonator's RF field must be 2.8 times larger than the z-component (named model in the figure 4.15), which is significantly different from the expected values in the simulation. The measurement result cannot be explained only consider the static field angle dependence of the magnon-photon coupling.

4.5.2 Field angle dependence of a threshold frequency of three-magnon splitting

In fact, provided the supression of the coupling strength is associated with the onset of the three-magnon splitting. The variation of $\omega_c/2\pi$ should be correlated with the variation of the frequency, at which the three-magnon splitting becomes allowed by the energy and momentum conservation laws. Figure 4.16(a) shows the

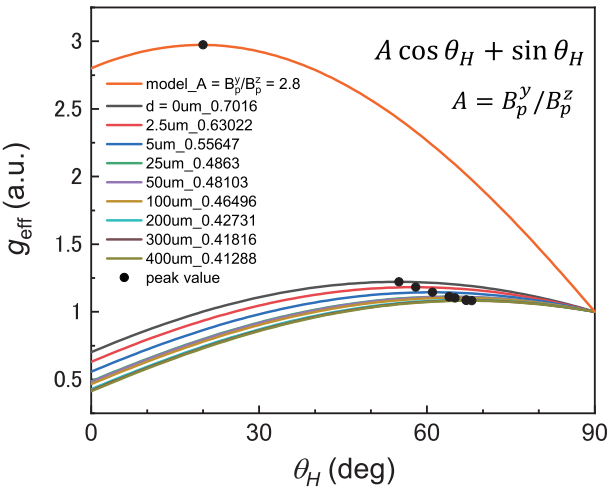

Figure 4.15 Simulated angle dependence of the coupling constant g_{eff}. They are plotted using the simulated magentic field strength B_p distributed at a distance d from the resonator surface. B_p is the result of spatial integration over the sample size (5×5 mm).

lowest-energy branch of the spectra of spin waves for YIG films with field angle from $\theta_H = 0$ to 90 deg calculated for $\mu_0 H = 10$ mT by using the theory developed in [2]. The point on the dispersion diagram at the frequency $\omega_0/2\pi$ and the zero wavenumber corresponds to the uniform FMR mode. The three-magnon splitting of the magnon of the quasi-uniform FMR mode represents a creation of two magnons with the frequencies $\omega_0/2\pi/2$. Correspondingly, this process is only allowed, if there are available spectral states at this frequency. As seen from Fig. 4.16(a), this is the case for angles with , whereas for the film with the lowest frequency in the spectrum fmin lies above $\omega_0/2\pi/2$. When the static magnetic field H_0 is varied, the spin-wave spectrum is shifted in the frequency space and the relation between the frequencies $\omega_0/2\pi/2$ and $\omega_{\text{min}}/2\pi$ changes too.

To characterize this change, we plot in Fig. 4.16(b) the field dependences of the frequency $\omega_0/2\pi/2$ and those of the frequency $\omega_{\text{min}}/2\pi$ for films with each angle. From the data of Fig. 4.16(a), it is clearly seen that for the film with , $\omega_0/2\pi/2 < \omega_{\text{min}}/2\pi$ at any H_0, i.e., the three-magnon splitting is completely prohibited in such angles. In contrast, for films with and 6 lm, the condition $\omega_0/2\pi/2 > \omega_{\text{min}}/2\pi$ necessary for the three-magnon splitting process is satisfied at H_0 smaller than a certain value $H_0 < H_{3m}$. It is also seen that, with the decrease of θ_H, the crossing point is shifted to smaller H_0, corresponding to larger cut-off frequencies. Figure 4.17 shows a quantitative comparison of the experimentally determined cut-off frequencies $\omega_c/2\pi$, at which the decrease of P_{abs}, with the calculated frequencies $\omega_{3m}/2\pi$, at which the three-magnon splitting becomes allowed (solid line), for film with different θ_H and resonance frequency of our used OSR (dotted line). From these data, it is seen that the relation of these two frequencies make the point at which above $\omega_{\text{res}}/2\pi$, three magnon affects the coupling via the enhancement of damping and below $\omega_{\text{res}}/2\pi$ the

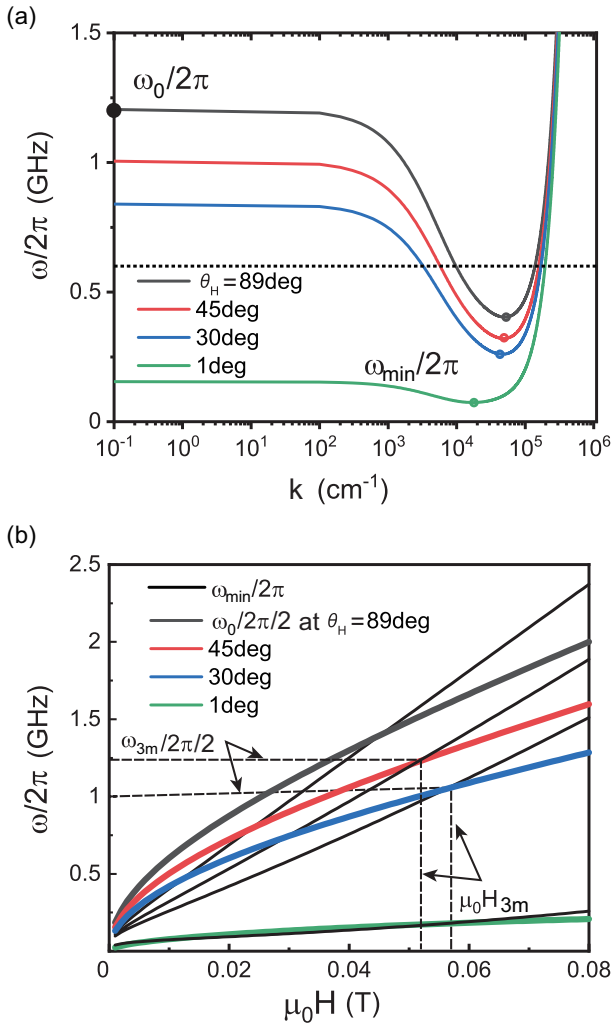

Figure 4.16 (a) The lowest-energy branch of the spectra of spin waves for YIG films with $\theta_H = 1, 30, 45$, and 89 deg calculated for $\mu_0 H_0 = 10$ mT (saturation magnetization of YIG $\mu_0 M_s = 175$ mT). The point on the dispersion diagram at the frequency $\omega_0/2\pi$ and the zero wavenumber corresponds to the uniform FMR mode. $\omega_{\min}/2\pi$ marks the lowest frequency in the spectrum of spin waves. (b) Field dependences of the frequency $\omega_0/2\pi/2$ and those of the frequency fmin for films with $\theta_H = 1, 30, 45$, and 89 deg. The points of interception determine the onset of the region, where three-magnon splitting is allowed. $H_{3m}, \omega_{3m}/2\pi$ corresponding boundary magnetic field and frequency.

effect dissapears. This result shows a good agreement with the angle depepndence of the coupling strength. Caliculated threshold from spion dispersion relation proves that the supression of the window depth is associated with the three-magnon splitting. Additionally, another data for different thicknesses of the YIG film shows the high frequency-shifted angle dependence of the change of the coupling strength. It is known that the variation of the film thickness also leads to a noticeable variation of critical frequency because film thickness also depends on the contribution of the magneto-dipole interaction to the energy of the secondary magnons.

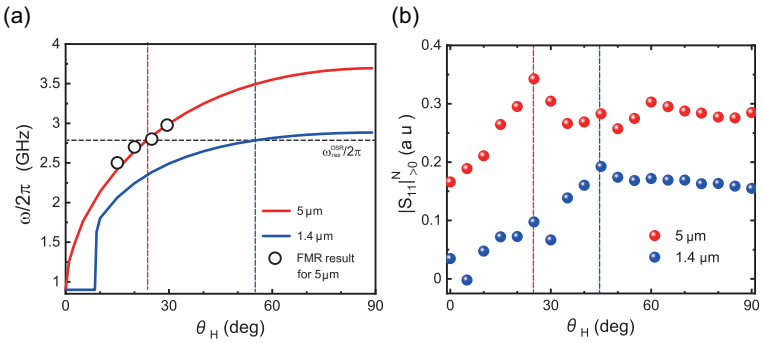

Figure 4.17 Comparison of the experimentally determined cut-off frequencies $\omega_c/2\pi$, (symbols), with the calculated frequency, at which the three-magnon splitting becomes allowed $\omega_{3m}/2\pi$ (solid line) in films with different field angles and resonance frequency of OSR (dotted line). Also plot the dependence of $\omega_c/2\pi$ on the thinner film thickness (thickness: 1.4 μm).

4.6 Summary

In summary, we performed electromagnetic field analysis of an Omega-shaped resonator and magnon-photon coupling measurement in YIG/resonator system in weak coupling regime. No avoided crossing appeared as in the strong coupling regime, but overlapping between photon mode and spin wave mode appeared. With out-of-plane rotation of the external magnetic field, the microwave absorption at the crossing point shows two properties; First, the coupling between the microwave photon mode and magnon mode exhibits an explicit angle dependence. Second, three-magnon splitting below the critical frequency cause the additonal damping of coupled state, leading the suppression of the absorption. The result demonstrate a new possibility to control the magnon-photon hybridized state in terms of nonlinear spin dynamics.

Chapter 5

Conclusion

We investigated the coherent dynamics of spin coupled state with superconductor and cavity photons. We analyzed (i) temperature dependence of spin Seebeck effect around the critival temperature in Superconductor/Ferrimagnetic insulator bilayer system and (ii) spins in single mode cavity system, which coherently couples with excited spin waves. Here, we summarize the major results and comments on their importance.

Chapter 3 **:** Spin current coherence peak in superconductor/magnet junctions

In this chapter, we found that inversed spin Hall voltage induced by spin Seebeck effects in a bilayer film compris- ing NbN and YIG layers is clearly enhanced in a narrow temperature range immediately below T_c, exhibiting a peak structure. This enhancement appears only in NbN/YIG, not in NbN/SiO_2/YIG or NbN/SiO_2, where only vortex Nernst voltages whose sign is opposite to the inversed spin Hall voltages were observed. A theoretical calculation of the spin Seebeck effects reveals that a coherence peak effect in the spin Seebeck effects for superconductors in which low-frequency magnons are taken into consideration can be responsible for the anomalous enhancement of the spin Seebeck effects.The spin-orbit coupling in the superconducting films is also found to be very useful for the research of superconductivity, since the dynamic spin response in superconductors is caused by a novel transport phenomenon called spin current. Therefore, our results suggest that the coherence effect, which has been mainly studied in nuclear magnetic relaxation in bulk superconductors, can also be realized in thin films of superconductors by using spin current and inverse spin Hall effect as a probe, and thus demonstrate the usefulness of spintronics technology in the field of superconductivity.

Chapter 4 **:** Coupling control in YIG Cavity Resonator systems

In this chapter, we have investigated the control of the magnon-photon coupling strength between YIG film and an Omega-shaped planar resonator by changing magnetic field angles and strengths. We confirmed that the out-of-plane field angle can shift the critical frequency of non-linear ferromagnetic resonance (FMR), in agreement with spin-wave dispersion relation calculated by YIG parameters. We have carried out a series of tests to clarify the coupling strength by observing overlapping between the FMR mode and resonator mode. We found that the anormalous microwave absorption exhibits the change around the critical angle where the three

magnon splitting is switched off. Varying the damping parameter through nonlinear spin dynamics is thus proposed as a new method of controlling the microwave transmission at the coupling region. In addition to that we suggest, among various resonators, a planar resonator is particularly suitable for coupling magnons in thin-films and photons concentrated near the resonator surface. They are relatively easily fabricated by lithography techniques, making it possible to design experiments in a variety of dimensions and shapes. Our result expand the new physics and develop the technique of planar resonators to realize the new coherently coupled state.

Bibliography

[1] Kalinikos B. A., IEE Proc. H - Microw. Opt. Antennas **127** 4 (1980).

[2] Kalinikos B. A., Solid State Phys., **19** pp. 7013–7033, (1986).

[3] G. Rado and J. Wertmann, S, J. Phys. Chem. Solids, 11, pp. No.3/4, 315 (1959).

[4] R. F. Soohoo, Phys. Rev., 131, pp. No.2, 594 (1962).

[5] Wigen, P. E. Nonlinear Phenomena and Chaos in Magnetic Materials (World Scientific) (1994).

[6] T. Boudiar, B. Payet-Gervy, M. F. Blanc-Mignon, J. Rousseau, M. Le Berre, and H. Joisten, J. Magn. Magn. Mater. 284, 77-85 (2004).

[7] Cherepanov, I. Kolokolov, and V. L' vov,, Physics Reports 229, 81–144 (1993).

[8] D. M. Pozar, Microwave Engineering, Wiley and Sons Ltd., 3rd edn. (2009).

[9] G.Woltersdorf, PhD thesis, Simon Fraser University, (2004).

[10] S. Kalarickal, P. Krivosik, M. Wu, C. Patton, M. Schneider, P. Kabos, T. Silva, and J. Nibarger, Journal of Applied Physics, vol. 99, p. 093 909, (2006).

[11] C. Patton, Journal of Applied Physics, vol. 39, p. 3063, (1968).

[12] C. Bilzer, T. Devolder, J.-V. Kim, G. Counil, C. Chappert, S. Cardoso, and P. Freitas, Journal of Applied Physics, vol. 100, p. 053 903, (2006).

[13] Kane Yee, IEEE Transactions on antennas and propagation, Vol. 14, No. 3, pp. 302–307, (1966).

[14] T. Itoh and R. Mittra, Analysis of a microstrip disk resonator, Arch. Elek. Übertragung 27, 456 (1973).

[15] J. Wollf and N. Knoppik, Rectangular and circular micorstrip disc capacitors and resonators, in The European Micorwave Conf. Brussels, Belgium (1973).

[16] T. Itoh, Analysis of Microstrip Resonators, IEEE Trans. Microw. Theory Tech. 22, 946 (1974).

[17] K. Kupfmuller, W. Mathis, and A. Reibiger, Theoretische Elektrotechnik, Springer Berlin, Heidelberg (2006).

[18] J. M. Martinis, K. B. Cooper, R. McDermott, M. Steven, M. Ansmann, K. D. Osborn, K. Cicak, S. Oh, D. P. Pappas, R. Simmonds, and C. C. Yu, Phys. Rev. Lett. 95, 210503 (2005).

[19] B. A. Mazin, Microwave Kinetic Inductance Detectors, Ph.D. thesis, California Institute of Technology (2004).

[20] M. Goppl, A. Fragner, M. Baur, R. Bianchetti, S. Filipp, J. Appl. Phys. 104, 113904 (2008).

[21] D. I. Schuster, Circuit Quantum Electrodynamics, Ph.D. thesis, Yale University (2007).

[22] D. M. Pozar, Microwave Engineering, Wiley and Sons Ltd., 3rd edn. (2009).

[23] J. Buechler, E. Kasper, P. Russer, K.M. Strohm, IEEE Trans. Microwave Theory Tech. 34 (1986).

[24] D.I. Hoult, Prog. NMR Spectrosc. 12 (1978).

[25] M. Jaworski, A. Sienkiewicz, Ch.P. Scholes,J. Magn. Reson. 124 (1997).

[26] H. Kurebayashi, O. Dzyapko, V. E. Demidov, D. Fang, A. J. Ferguson, and S. O. Demokritov, Nat. Mater. 10, 660 (2011).

[27] O. Dzyapko,H. Kurebayashi, E. Demidov,M. Evelt, A. J. Ferguson,and S. O. Demokritov, Appl. Phys. Lett. 102, 252409 (2013)

[28] H. Beutler, Z. Phys. 93, 177–196 (1935).

[29] U. Fano, Nuovo Cimento 12, 154– 161 (1935).

[30] A. E. Miroshnichenko, S. Flach, and Y. S. Kivshar, Rev. Mod. Phys. 82, 2257 (2010).

[31] Y. S. Joe, A. M. Satanin, and C. S. Kim, Phys. Scr. 74, 259 (2006).

[32] K. Ando *et al.*, J. Appl. Phys. **109**, 103913 (2011).

[33] V. Cherepanov, I. Kolokolov, and V., Physics Reports, vol.229, issue.3, p.81, (1993).

[34] G. Binasch *et al.*, Phys. Rev. B **39**, 4282 (1989).

[35] M. N. Baibich *et al.*, Phys. Rev. Lett. **61**, 2472 (1988).

[36] T. Miyazaki and N. Tezuka, J. Magn. Magn. Mater. **139**, L231 (1995).

[37] S. Yuasa *et al.*, Nat. Mater. **3**, 868 (2004).

[38] S. Ikeda *et al.*,Appl. Phys. Lett. **93**, 082508 (2008).

[39] D. C. Ralph, M. D. Stiles, J. Magn. Magn. Mater. **320**, 1190 (2008).

[40] A. Yamaguchi *et al.*, Phys. Rev. Lett. **92**, 77205 (2004).

[41] K. Uchida, T. Ota, H. Adachi, J. Xiao, T. Nonaka, Y. Kajiwara, G. E. W. Bauer, S. Maekawa, and E. Saitoh, J. Appl. Phys. **111**, 103903 (2011).

[42] G. E. W. Bauer, E. Saitoh, and B. J. van Wees, Nat. Mater. **11**, 391 (2012).

[43] S. Mizukami, Y. Ando and T. Miyazaki, Jpn. J. Appl. Phys. **40**, 580 (2001).

[44] S. Mizukami, Y. Ando and T. Miyazaki, J. Magn. Magn. Mater. **226-230**, 1640 (2001).

[45] B. Heinrich, D. Fraitova and V. Kambersky, Phys. Stat. Sol. (b), **23**, 501 (1967).

[46] V. Kambersky, Can. J. Phys., **48**, 2906 (1970).

[47] V. Kambersky, Czech. J. Phys. B **65**, 212411 (1976).

[48] M. I. Dyakonov and V. I. Perel, JETP Lett. **13**, 467 (1971); Phys. Lett. **A35**, 459 (1971).

[49] S. Murakami, N. Nagaosa, and S. C. Zhang, Science **301**, 1348 (2003).

[50] J. Sinova *et al.*, Phys. Rev. Lett. **92**, 126603 (2004).

[51] E. Saitoh, M Ueda, H. Miyajima, and G. Tatara, Appl. Phys. Lett. **88**, 182509 (2006).

[52] T. Kimura *et al.*, Phys. Rev. Lett. **98**, 156601 (2007).

[53] S. O. Valenzuela, M. Tinkham, Nature **442**, 176 (2006).

[54] R. H. Silsbee, A. Janossy and P. Monod, Phys. Rev. B **19**, 4382 (1979).

[55] Y. Tserkovnyak and A. Brataas, Phys. Rev. Lett. **88**, 117601 (2002).
[56] Y. Tserkovnyak and A. Brataas, Phys. Rev. B **66**, 224403 (2002).
[57] M. Zwierzycki *et al.*, Phys. Rev. **71**, 064420 (2002).
[58] K. Uchida *et al.*, Nature **455**, 778 (2008).
[59] L. F. Mattheiss, Phys. Rev. B **5**, 315 (1972).
[60] J. Linder and J. W. A. Robinson, Nat. Phys. **11**, 307-315 (2015).
[61] D. Beckmann, J. Phys. Cond. Mat. **28**, 163001 (2016).
[62] I. Žutić, J. Fabian, and S. Das Sarma, Rev. Mod. Phys. **76**, 323 (2004).
[63] A. I. Buzdin, Rev. Mod. Phys. **77**, 935 (2005).
[64] B. M. Andersen, Y. S. Barash, S. Graser, and P. J. Hirschfeld, Phys. Rev. B **77**, 054501 (2008).
[65] R. Meservey and P. M. Tedrow, Phys. Rep. **238**, 173 (1994).
[66] Y. K. Kato, R. C. Myers, A. C. Gossard, D. D. Awschalom, Science **306** (5703), 1910-1913, (2004).
[67] C. Stamm, C. Murer, M. Berritta, J. Feng, M. Gabureac, P. M. Oppeneer, and P. Gambardella, Phys. Rev. Lett. **119**, 087203 (2017).
[68] T. Yamashita, S. Takahashi, H. Imamura, and S. Maekawa, Phys. Rev. B **65**, 172509 (2002).
[69] S. Takahashi and S. Maekawa, Phys. Rev. Lett. **88**, 116601 (2002).
[70] A. Hoffman, IEEE Trans. Magn. **49**, 5172 (2013).
[71] T. Wakamura, N. Hasegawa, K. Ohnishi, Y. Niimi, and Y. Otani, Phys. Rev. Lett. **112**, 036602 (2014).
[72] T. Wakamura, H. Akaike, Y. Omori, Y. Niimi, S. Takahashi, A. Fujimaki, S. Maekawa, and Y. Otani, Nat. Mater. **14**, 675 (2015).
[73] J. Xiao, G. E. W. Bauer, K. Uchida, E. Saitoh, and S. Maekawa, Phys. Rev. B **81**, 214418 (2010).
[74] H. Adachi, J. Ohe, S. Takahashi, and S. Maekawa, Phys. Rev. B **83**, 094410 (2011).
[75] H. Adachi, K. Uchida, E. Saitoh, and S. Maekawa, Rep. Prog. Phys. **76**, 036501 (2013).
[76] L. J. Cornelissen, K. J. H. Peters, G. E. W. Bauer, R. A. Duine, and B. J. van Wees, Phys. Rev. B **94**, 014412, (2016).
[77] M. Tinkham, Introduction to Superconductivity, McGraw-Hill, New York (1975).
[78] L. C. Hebel *et al.*, Phys. Rev. **113**, 1504 (1959).
[79] D. C. Mattis and J. Bardeen,Phys. Rev. **111**, 412 (1958).
[80] R. Valdès Aguilar *et al.*, Phys. Rev. B **82**, 180514 (2010).
[81] R. Metselaar and P. K. Larsen, Solid State Commun., **15**, 291 (1974).
[82] S. Wittekoek, T. J. A. Popma, J. M. Robertson, and P. F. Bongers, Phys. Rev. B, **12**, 2777-2788 (1975).
[83] S. H. Yuan *et al.*,, J. Appl. Phys. **61**, 3552 (1987).
[84] K. Komemou, T. Yamashita, and Y. Onodera, Phys. Rev. A **28**, 335 (1968).
[85] C. Bell, S. Milikisyants, M. Huber, and J. Aarts, Phys. Rev. Lett. **100**, 047002

(2008).

[86] D. M. Glowacka, D. J. Goldie, S. Withington, H. Muhammad, G. Yassin, arXiv:1401.2276 (2014).

[87] K. L. Westra *et al.*, J. Vac. Sci. Tech., **A8**, 1288-1293 (1990).

[88] T. Kikkawa, K. Uchida, S. Daimon, Z. Qiu, Y. Shiomi, and E. Saitoh, Phys. Rev. B **92**, 064413 (2015).

[89] T. Tanaka, H. Kontani, M. Naito, T. Naito, D. S. Hirashima, K. Yamada, and J. Inoue, Phys. Rev. B **77**, 165117 (2013).

[90] H. Jin, S. R. Boona, Z. Yang, R. C. Myers, and J. P. Heremans, Phys. Rev. B **92**, 054436 (2015).

[91] T. T. M. Palstra, B. Batlogg, L. F. Schneemeyer, and J. V. Waszczak, Phys. Rev. Lett. **64**, 3090 (1990).

[92] H. C. Ri, R. Gross, F. Gollnik, A. Beck, R. P. Huebener, P. Wagner, and H. Adrian, Phys. Rev. B **50**, 3312 (1994).

[93] Z. A. Xu, N. P. Ong, Y. Wang, T. Kakeshita, and S. Uchida, Nature (London) **406**, 486 (2000).

[94] Y. Wang, Z. A. Xu, T. Kakeshita, S. Uchida, S. Ono, Y. Ando, and N. P. Ong, Phys. Rev. B **64**, 224519 (2001).

[95] Y. Wang, N. P. Ong, Z. A. Xu, T. Kakeshita, S. Uchida, D. A. Bonn, R. Liang, and W. N. Hardy, Phys. Rev. Lett. **88**, 257003 (2002).

[96] R. P. Huebener, Supercond. Sci. Technol, **8**, 189-198 (1995).

[97] K. Ohnishi, Y. Ono, T. Nomura, and T. Kimura, Sci. Rep. **4**, 6260 (2014).

[98] D. N. Langenderg and A. Larkin, Non-Equilibrium Superconductivity, North-Holland, Amsterdam (1980) and references therein.

[99] M. Inoue, M. Ichioka, and H. Adachi, Phys. Rev. B **96**, 024414 (2017).

[100] Y. Yao, Q. Song, Y. Takamura, J. P. Cascales, W. Yuan, Y. Ma, Y. Yun, J. S. Moodera, X. C. Xie, and W. Han, Phys. Rev. B **97**, 224414 (2018).

[101] T. Kato, Y. Ohnuma, M. Matsuo, J. Rech, T. Jonckheere, and T. Martin, Phys. Rev. B **99**, 144411 (2019).

[102] T. Taira, Y. Kato, M. Ichioka, and H. Adachi, arXiv:2012.03471v1 (2020).

[103] S. Maekawa, S. O. Valenzuela, E. Saitoh, and T. Kimura, Spin Current, Oxford University Press (2012).

[104] J. Bardeen, L.N. Cooper, and J. R. Schrieffer, Phys. Rev. **108**, 1175 (1957).

[105] J. R. Waldram, Superconductivity of Metals and Alloys, Westview Press, Boulder, United States of America (1992).

[106] F. Gao, G. L. Carr, C. D. Porter, and D. B. Tanner, Phys. Rev. B **54**, 700 (1994).

[107] G. E. W. Bauer, E. Saitoh, and B. J. van Wees, Nat. Mater. **11**, 391 (2012).

[108] O. Klein, E. J. Nicol, K. Holczer, and G. Grüner, Phys. Rev. B **50**, 6307 (1994).

[109] H. Huebl, C. W. Zollitsch, J. Lotze, F. Hocke, M. Greifenstein, A. Marx, R. Gross, and S. T. B. Goennenwein, Phys. Rev. Lett. **111**, 127003 (2013).

[110] X. Zhang, C. Zou, L. Jiang, and H. X. Tang, Phys. Rev. Lett. **113**, 156401

(2014).

[111] Y. Tabuchi, S. Ishino, T. Ishikawa, R. Yamazaki, K. Usami, and Y. Nakamura, Phys. Rev. Lett. **113**, 083603 (2014).

[112] Y. Tabuchi, S. Ishino, A. Noguchi, T. Ishikawa, R. Yamazaki, K. Usami, and Y. Nakamura, C. R. Physique **17**, 729–739 (2016).

Acknowledgements

I would like to thank many people for their guidance and help in carrying out this study. I would like to thank my advisor, Professor Eiji Saitoh, for his scientific guidance and his personal support. I would like to thank Professor Saburo Takahashi, for his many contributions on numerical calculations and the theory. I would like to thank Professor Yuki Shiomi, for his detailed guidance from beginning to end, including experimental techniques, data analysis, and paper writing. He corrected my paper many times, down to the smallest details. I would like to thank Professor Takashi Kikkawa, whose assistance made these experiments possible. I would like to thank Dr. Tomohiko Niizeki, without whom the samples for the first series of experiments would not exist. I would like to thank Professor Jana Lustikova, for correcting my English in my paper. I would like to thank Professor Shunsuke Daimon, for giving me advice to built the measurement program. I would like to thank Dr. Naoto Yokoi, who taught me how to develop the logic in physics, and introduced me to some books on the theoretical content, which was very helpful to me. I would like to thank Professor Hidekazu Kurebayashi, for giving me the chance to study in his Lab and helpful discussions. I would like to thank Dr. Christoph W. Zollitsch and Aakanksha Sud, for their experimantal help and exchange of ideas and tolerating countless questions. I would like to thank Dr. Kei Yamamoto, for the fruitful discussions and calculations on experimental results. I would like to thank Tomosato Hioki, Yao Chen, and Hiroki Arisawa for my time spent in the Lab. I would like to thank Sec. Marie Minagawa and Sec. Yumiko Sato for their continuous help. I would also like to thank all the people at Tohoku University, the University of Tokyo, and UCL who have been involved in my research life. I would like to thank my family and friends—in particular my father and mother, and everyone else along the way for everything.

The existence of this graduate student was enabled by GP-Spin (October 2017 - March 2021), and by Japan Society for Promotion of Science through a research fellowship for young scientists (April 2016 - March 2021, code 19J13544).

I sincerely thank you.

Shizuoka, 8 February 2021

List of Publications

Peer-reviewed papers

1. "Spin-current coherence peak in superconductor/magnet junctions", Maki Umeda, Yuki Shiomi, Takashi Kikkawa, Tomohiko Niizeki, Jana Lustikova, Saburo Takahashi, and Eiji Saitoh, Appl. Phys. Lett., 112, 232601 (2018).

2. "The bimodal distribution spin Seebeck effect enhancement in epitaxial $Ni_{0.65}Zn_{0.35}Al_{0.8}Fe_{1.2}O_4$ thin film", Hua Wang, Dazhi Hou, Takashi Kikkawa, Rafael Ramos, Ka Shen, Zhiyong Qiu, Yao Chen, Maki Umeda, Yuki Shiomi, Xiaofeng Jin, and Eiji Saitoh, Appl. Phys. Lett., 112, 142406 (2018).

3. "Electric readout of magnetic stripes in insulators", Yao Chen, Yuki Shiomi, Zhiyong Qiu, Tomohiko Niizeki, Maki Umeda, and Eiji Saitoh, Sci. Rep. 9 19052 (2019).

Appendix A

Magnetostatic Approximation

The so-called magnetostatic approximation is an approximation for the Maxwell equations in which electromagnetic propagation effects are ignored. This is one of the basic approximations implemented in the standard theories for spin waves and magnetostatic modes. Historically, the approximation bears the name "magnetostatic", though it is really for magnetic waves at microwave frequencies.

Consider the full set of Maxwell equations for the dynamic electric and magnetic fields, $\boldsymbol{e}(\boldsymbol{r},t)$ and $\boldsymbol{h}(\boldsymbol{r},t)$, and the dynamic magnetization $\boldsymbol{m}(\boldsymbol{r},t)$ for a magnetic insulator with a scalar dielectric constant ϵ.

$$\nabla \cdot \boldsymbol{e}(\boldsymbol{r},t) = 0. \tag{A.1}$$

$$\nabla \times \boldsymbol{e}(\boldsymbol{r},t) = -\frac{1}{c}\frac{\partial}{\partial t}[\boldsymbol{h}(\boldsymbol{r},t) + 4\pi \boldsymbol{m}(\boldsymbol{r},t)]. \tag{A.2}$$

$$\nabla \cdot [\boldsymbol{h}(\boldsymbol{r},t) + 4\pi \boldsymbol{m}(\boldsymbol{r},t)] = 0. \tag{A.3}$$

$$\nabla \times \boldsymbol{h}(\boldsymbol{r},t) = \frac{\epsilon}{c}\frac{\partial}{\partial t}\boldsymbol{e}(\boldsymbol{r},t) \tag{A.4}$$

Here, c denotes the speed of light in free space. These equations are written in Gaussian units. The usual approach in the magnetostatic approximation is to write the $\nabla \times \boldsymbol{h}$ equation as

$$\nabla \times \boldsymbol{h}(\boldsymbol{r},t) = 0, \tag{A.5}$$

thereby neglecting the times derivative driving term in Eq. (A.4). Equation (A.5), together with Eq. (A.3), leads the well-known spin wave dipole field expression.

In this appendix, we consider spin wave components at wavenumber k and frequency ω_k for $\boldsymbol{h}(\boldsymbol{r},t)$ and $\boldsymbol{m}(\boldsymbol{r},t)$. We use the full Maxwell equations to obtain the connection between these components. We then establish the specific restrictions on k and ω_k for which the dipole field expression developed from Ea. (A.3) is valid. This defines the magnetostatic approximation.

From the full Maxwell equations, the wave equation for $\boldsymbol{h}(\boldsymbol{r},t)$ is

$$\nabla^2 \boldsymbol{h}(\boldsymbol{r},t) - \frac{\epsilon}{c^2}\frac{\partial^2}{\partial t^2}\boldsymbol{h}(\boldsymbol{r},t) \tag{A.6}$$

$$= -4\pi \nabla[\nabla \cdot \boldsymbol{m}(\boldsymbol{r},t)] + 4\pi \frac{\epsilon}{c^2}\frac{\partial^2}{\partial t^2}\boldsymbol{m}(\boldsymbol{r},t). \tag{A.7}$$

We now consider plane wave solutions for $\boldsymbol{h}(\boldsymbol{r},t)$ and $\boldsymbol{m}(\boldsymbol{r},t)$ with frequency ω_k and

wavevector $\boldsymbol{k}$.

$$\boldsymbol{h}(\boldsymbol{r},t) = \boldsymbol{h}_k e^{i(\omega_k t - \boldsymbol{k}\cdot\boldsymbol{r})} \tag{A.8}$$

$$\boldsymbol{m}(\boldsymbol{r},t) = \boldsymbol{m}_k e^{i(\omega_k t - \boldsymbol{k}\cdot\boldsymbol{r})}. \tag{A.9}$$

To derive the relation between the time-independent amplitudes $\boldsymbol{h}_k$ and $\boldsymbol{m}_k$ we write the maxwell equation as follows.

$$\boldsymbol{k}\times\boldsymbol{h} = \frac{\epsilon\omega_k}{c}\boldsymbol{e} \tag{A.10}$$

$$\boldsymbol{k}\times\boldsymbol{e} = -\frac{\omega_k}{c}[\boldsymbol{h} + 4\pi\boldsymbol{m}]. \tag{A.11}$$

Crossing $\boldsymbol{k}$ into both sides of Eq. (A.11) gives

$$\boldsymbol{k}(\boldsymbol{k}\cdot\boldsymbol{h}) - k^2\boldsymbol{h} = -\omega_k^2 c^2\epsilon(\boldsymbol{h} + 4\pi\boldsymbol{m}), \tag{A.12}$$

where we substituted Eq. (A.11) for $\boldsymbol{k}\times\boldsymbol{e}$. Since $\boldsymbol{k}\cdot[\boldsymbol{h} + 4\pi\boldsymbol{m}] = 0$, it follows that

$$\boldsymbol{k}\cdot\boldsymbol{h} = -\boldsymbol{k}\cdot 4\pi\boldsymbol{m}. \tag{A.13}$$

Substituting this result into Eq. (A.12) and solving for $\boldsymbol{h}$ gives

$$\boldsymbol{h}_k = -\frac{1}{k^2 - k_0^2}4\pi\boldsymbol{k}(\boldsymbol{k}\cdot\boldsymbol{m}_k) + \frac{k_0^2}{k^2 - k_0^2}4\pi\boldsymbol{m}_k \tag{A.14}$$

Here, k_0 denotes the wavenumber for ordinary electromagnetic waves propagating with the same frequency ω_k in the medium,

$$k_0 = \frac{\omega_k}{c}\sqrt{\epsilon} \tag{A.15}$$

The two terms in Eq. (A.14) have different physical origins. The $\boldsymbol{k}(\boldsymbol{k}\cdot\boldsymbol{m}_k)$ term derives from the microscopic magnetic dipole-dipole interaction. The $4\pi\boldsymbol{m}_k$ term derives from the teme-derivative of the electric field and, therefore, may be called the electromagnetic propagation term. in a situation where the $|k| \gg k_0$ is satisfied, the contribution from the $4\pi\boldsymbol{m}_k$ term in Eq. (A.14) is negligible. In this limit, only the dipole field remains and Eq. (A.14) can be approximated to

$$\boldsymbol{h}_k \approx -\frac{4\pi}{k^2}\boldsymbol{k}(\boldsymbol{k}\cdot\boldsymbol{m}_k) \tag{A.16}$$

This form of the dipole field is utilized extensively in classical spin wave theory.

The nonuniform dipole field $\boldsymbol{h}_k(\boldsymbol{r},t)$ for $k \gg 2\pi/d$, where d is a nominal sample dimension,

$$\boldsymbol{h}_k = -\frac{4\pi}{k^2}\boldsymbol{k}(\boldsymbol{k}\cdot\boldsymbol{m}_k(t)) = -4\pi\boldsymbol{N}_k\cdot\boldsymbol{m}_k(t). \tag{A.17}$$

the dipole tensor is defined by the 3×3 matrix

$$\boldsymbol{N}_k = \frac{1}{k^2}\begin{pmatrix} k_x^2 & k_xk_y & k_xk_z \\ k_yk_x & k_y^2 & k_yk_z \\ k_zk_x & k_zk_y & k_z^2 \end{pmatrix}, \tag{A.18}$$

where the k_x, k_y, and k_z components are related to the wave number k and the angles θ_k and ϕ_k.

$$k_x = k \sin\theta_k \cos\phi_k \tag{A.19}$$

$$k_y = k \sin\theta_k \sin\phi_k \tag{A.20}$$

$$k_z = k \cos\theta_k \tag{A.21}$$

It is convenient to separate the $\boldsymbol{N}_k$ matrix into two parts, one which contains the first two columns,

$$\boldsymbol{N}_k^L = \frac{1}{k^2} \begin{pmatrix} k_x^2 & k_x k_y & 0 \\ k_y k_x & k_y^2 & 0 \\ k_z k_x & k_z k_y & 0 \end{pmatrix}, \tag{A.22}$$

and one with the last column only,

$$\boldsymbol{N}_k^N = \frac{1}{k^2} \begin{pmatrix} 0 & 0 & k_x k_z \\ 0 & 0 & k_y k_z \\ 0 & 0 & k_z^2 \end{pmatrix}. \tag{A.23}$$

Terms deriving from the $\boldsymbol{N}_k^N \cdot \boldsymbol{m}_k(t)$ product contain $m_{kz}(t)$ terms, which bring in second order terms in $m_{0x}(t)m_{ky}(t)$ and $m_{0y}(t)m_{kx}(t)$. These nonlinear terms will contribute to the nonlinear equation of motion for spin wave instability.

Appendix B

Holstein-Primakoff transformation

The linear equation of motion for spin waves in $\alpha_k(t)$ and $\alpha^*_{-k}(t)$ was obtained and given by

$$\frac{d}{dt}\begin{pmatrix} \alpha_k(t) \\ \alpha^*_{-k}(t) \end{pmatrix} = i\begin{pmatrix} A_k & B_k \\ -B^*_k & -A_k \end{pmatrix}\begin{pmatrix} \alpha_k(t) \\ \alpha^*_{-k}(t) \end{pmatrix} \tag{B.1}$$

with

$$A_k = \omega_H + |\gamma|Dk^2 + \frac{1}{2}\omega_M \sin^2\theta_k \tag{B.2}$$

$$B_k = \frac{1}{2}\omega_M \sin^2\theta_k e^{i2\phi_k} \tag{B.3}$$

We seek a linear transformation of the form

$$\begin{pmatrix} b_k(t) \\ b^*_{-k}(t) \end{pmatrix} = \begin{pmatrix} \lambda_k & \mu_k \\ \mu^*_k & \lambda_k \end{pmatrix}\begin{pmatrix} \alpha_k(t) \\ \alpha^*_{-k}(t) \end{pmatrix} \tag{B.4}$$

which will decouple the couled $[\alpha_k(t), \alpha^*_{-k}(t)]$ modes. the formal approach for such a transformation stars with the basic eigenvalue equation for the matrix in Eq. (B.1).

$$\begin{vmatrix} A_k - \lambda & B_k \\ -B^*_k & -A_k - \lambda \end{vmatrix} = 0 \tag{B.5}$$

the two eigenvalues obtained from Eq. (B.5) are given by

$$\lambda_{1,2} = \pm\sqrt{A_k^2 - |B_k^2|} \tag{B.6}$$

the transformation coefficients λ_k ad μ_k in Eq. (B.4) are obtained in the usual manner for eigenvalue problems, based on the now determined eigenvalues $\lambda_{1,2}$ and the requirement that the transformed $[b_k(t), b^*_{-k}(t)]$ mode pair be uncoupled. One obtains the result of Holstein and Primakoff.

$$\lambda_k = \sqrt{(A_k + \omega_k)/(2\omega_k)} \tag{B.7}$$

$$\lambda_k = \sqrt{(A_k - \omega_k)/(2\omega_k)}e^{i2\phi_k} \tag{B.8}$$

The $\lambda_{1,2}$ parameters correspond to the eigenfrequencies of our now uncoupled modes. We denote these eigenfrequencies as $\pm\omega_k$. The explicit form of ω_k from Eqs. (B.5), (B.2), and (B.3) is given by

$$\omega_k = |\gamma|\sqrt{(H_{\text{ext}} - 4\pi M_s N_z + Dk^2)(H_{\text{ext}} - 4\pi M_s N_z + Dk^2 + 4\pi M_s \sin^2\theta_k)} \tag{B.9}$$

This ω_k is the spin wave normal mode frequency.

The spin wave equation of motion for $[b_k(t), b^*_{-k}(t)]$ is now written as

$$\frac{d}{dt}\begin{pmatrix} b_k(t) \\ b^*_{-k}(t) \end{pmatrix} = i\begin{pmatrix} \omega_k & 0 \\ 0 & \omega_k \end{pmatrix}\begin{pmatrix} b_k(t) \\ b^*_{-k}(t) \end{pmatrix}. \tag{B.10}$$

Equation (B.10) has simple uncoupled harmonic oscillator solutions for $b_k(t)$ and $b^*_{-k}(t)$.

$$b_k(t) = b_k e^{i\omega_k t} \tag{B.11}$$

$$b^*_{-k}(t) = b^*_{-k} e^{-i\omega_k t} \tag{B.12}$$

These are the classical spin wave normal modes.